UNIVERSITA' DEGLI STUDI DI PARMA

Dottorato di ricerca in
Scienza e Tecnologia dei Materiali

Ciclo XXIX

# Carbon nanostructures for hydrogen storage

Coordinatore:

Chiar.mo Prof. Enrico Dalcanale

Tutor:

Chiar.mo Prof. Mauro Riccò

Dottorando: Giacomo Magnani

*“Ama et fac quod vis”*

Sant’Agostino

**Contents**

**Chapter 1**

# Introduction

This thesis is focused on synthesis, characterization and physical study of new carbon based materials (fullerides and graphenes) for the storage of hydrogen and it has been carried out at the Carbon Nanostructures Laboratory (CNL) of the Department of Physics and Earth Sciences at the University of Parma under the supervision of Prof. Mauro Riccò.

The aims of this study are the synthesis and optimization of these materials, the improvement of their storage properties and the understanding of the mechanisms and the specific interaction between hydrogen atoms and metal decorated graphene and alkali cluster intercalated fullerides.
This study starts from preliminary results published in the last few years by my research group and it is part of a comprehensive approach to the use of carbon nanostructures for hydrogen storage, as developed in the CNL group. It has to be placed in the context of a growing demand of renewable fuels such as hydrogen, identified as a possible replacement to the current gasoline for automotive application. In this domain, considerable interest is stimulated by the carbon nanostructures for their relatively low weight and the possibility to modify the interaction energy with the hydrogen molecule.

## 1.1 Energy problems & Hydrogen-based Solutions

Nowadays we are facing energetic and environmental problems.
The extensive use of fossil fuels is rapidly depleting a nonrenewable resource and its combustion produces carbon dioxide emissions that accelerate the greenhouse effect contributing to global warming [1]. Exhaust emissions from petrochemical fueled transportation release also a large amount of oxides of nitrogen ($NO_x$), greenhouse gases that play an important role in the destruction of the ozone layer [2)].
We need to change our economy based on nonrenewable oil/gas to a renewable based economy.
Hydrogen could be a good candidate as a practical source of energy, creating a cycle of $H_2$ that can replace with benefits all the traditional energetical steps and problems.

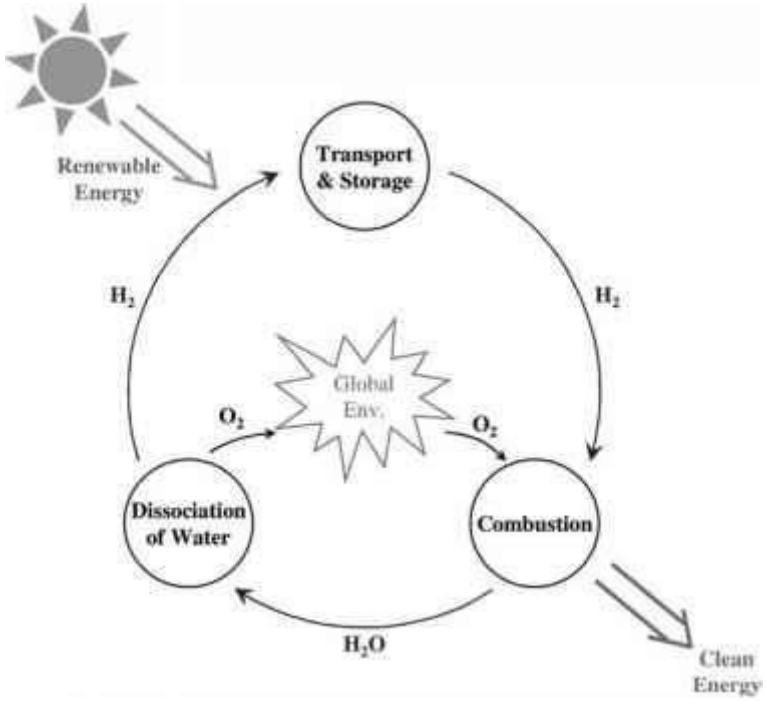


Figure 1: Cycle of Hydrogen

Hydrogen is an energy vector that can be burned as a fuel releasing an energy three times bigger than liquid hydrocarbons and the product of the combustion is water instead of $CO_2$ [3)].
The production of $H_2$ can occur in different ways, the most common and green method is by electrolysis of water using renewable energy sources like solar and biomass to dissociate the water molecule. Starting from renewable sources for hydrogen production would again contribute to eliminate the $CO_2$ emissions involved in the current method of energy production.
For these reasons many countries are developing strategies and technologies to make real this new promising economy, starting from the automotive sector.
Although hydrogen allows the possibility of a large scale storage: its density in relation with the storage systems represents the main practical problem that prevents its use.

It is essential that the autonomy of the hydrogen devices is at least comparable to the range of the petrol and diesel vehicles and to reach these performances we need to use approximately 4kg of $H_2$, the amount required to cover a distance of 400 km [4)].
This amount of required $H_2$, at room temperature and pressure would occupy a volume of 45 $m^3$, impractical for a car system.
First of all we need to introduce two fundamental parameters connected with this problem: volumetric density and gravimetric density.
The first describes the capacity of a material to store hydrogen according to the volume space of the system it occupies (tank); the gravimetric density determines the amount in weight per cent of hydrogen accumulated in that materials.

To address the problem it was thought about several solutions that can be divided by considering the three different states of hydrogen:

-storage in gas phase by means of high pressure compression to reduce the volume

-storage in liquid phase

-solid state storage using absorbent materials capable of easily loading and release hydrogen

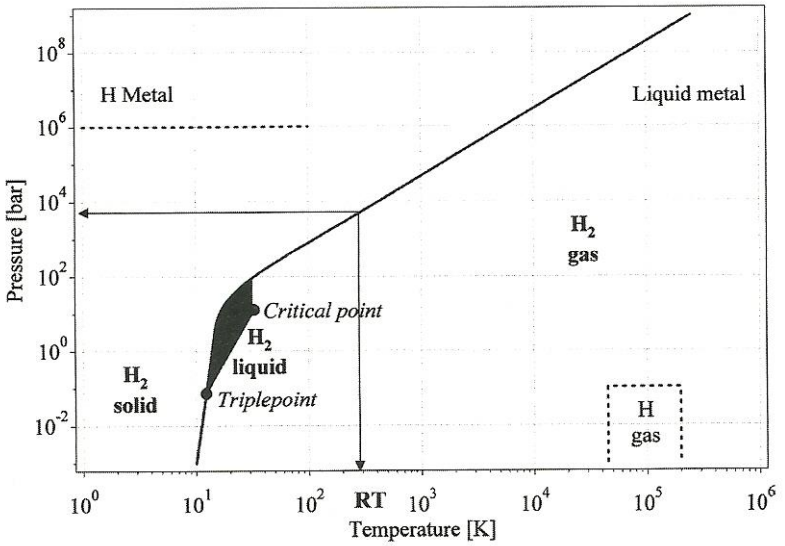


Figure 2: Hydrogen phase diagram [5]

In the compression strategy novel high-pressure tanks made of carbon-fiber-reinforced composite materials have being developed and are able to resist up to 600 bar and filled up to 450 bar for regular use [6].
However they have several disadvantages and problems, mainly in the safety field due to the risk of an explosion.

The condensation of gaseous hydrogen into liquid form is particularly attractive from the point of view of increasing the mass per container volume because the density of liquid hydrogen is 70.8 kg $m^{-3}$ and because we don't have to operate under pressure [7].

However also this storage solution present many problems caused by the working temperature.

At 1 bar the condensation temperature of hydrogen is –252 °C and the vaporization enthalpy at the boiling point is 452 kJ $kg^{-1}$. Liquid hydrogen containers are open systems to prevent strong overpressure and can lead to the loss of hydrogen as a consequence of heat transfers of the system.

So unfortunately these continuing losses by evaporation can cause a danger of overpressure.

The use of materials capable of storing hydrogen seems to be the most promising way for a practical application, having also a higher volumetric density than gaseous and liquid storage [8], but an important aspect to underline is the different interactions of $H_2$ with materials.

Hydrogen can bind an atom with different bond strengths: it can be physisorbed or chemisorbed by solid state materials.

In the former case there is a surface interaction between molecular hydrogen and the adsorber system. Responsible for the molecular adsorption of hydrogen are weak dispersive Van der Waals forces, between the gas molecules and the atoms on the surface of the solid. Due to the weak interaction between molecular hydrogen and solids, the amount of hydrogen stored at room temperature is very low, while it can consistently increase at low temperatures, typically 77 K.

Physisorption, depending on the applied pressure and the temperature, is a completely reversible process, which means that the hydrogen can be easily adsorbed and released during several cycles without any loss. Furthermore, no activation energy is involved in the molecular adsorption of hydrogen, which leads to very fast kinetics of the adsorption and desorption process.

Since in physisorption the hydrogen is adsorbed only on the surface of a solid, rather than in the bulk, the most suitable materials for molecular hydrogen storage must be porous and they have a high specific surface area. For these reasons the most studied and attractive materials in this field are zeolites [9], clathrates [10], metal organic framework (MOFs)[11] and carbon based materials [12].

During the chemisorption hydrogen binds to an atom forming a ionic or covalent bond and this strong interaction involves high binding energy and gives in terms of application a reversibility problem and also bad kinetics and/or thermodynamic properties because the formed bond is very stable.

Many metals and alloys are capable of reversibly absorbing large amounts of hydrogen, as we can see in the figure 3.

The family of hydrides is the most studied class of materials based on chemisorptions and it presents good values in terms of volumetric and gravimetric density.

One more important advantage of metal hydrides is the ability to store hydrogen in a very efficient way enabling hydrogen storage at rather low pressures without further need for liquefaction or compression [13].

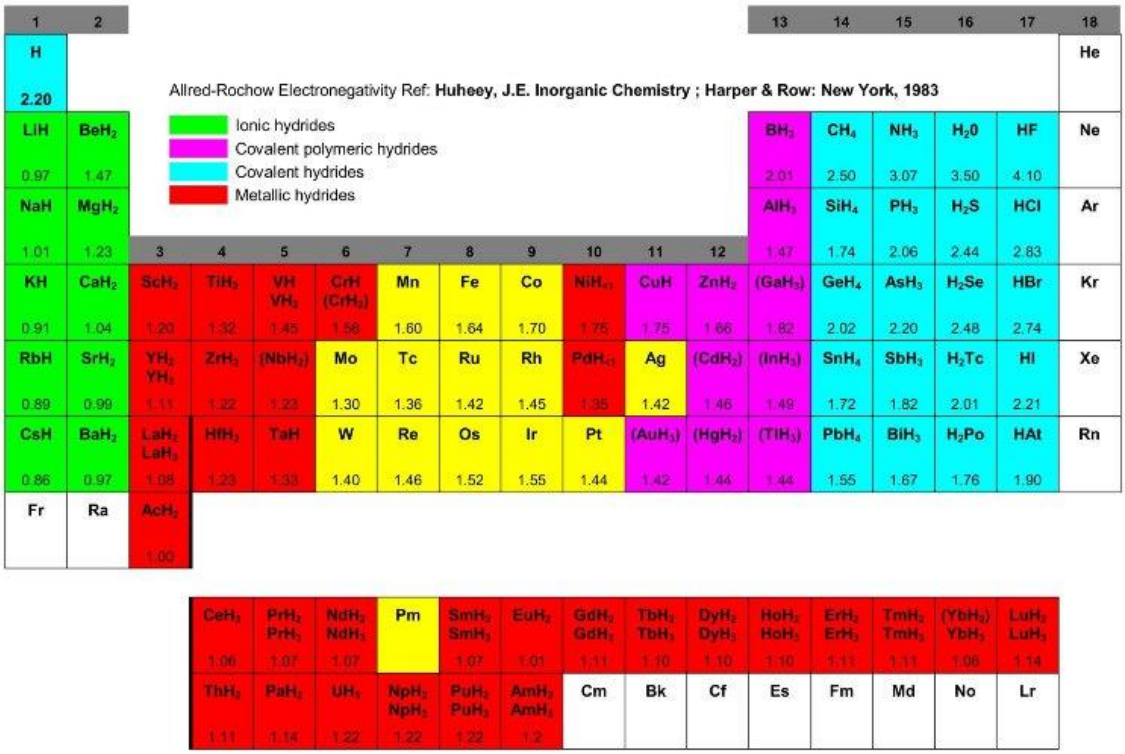


Figure 3: periodic tables of hydrides

However the products of hydrogenation are too stable and the hydrogen release is energetically too expensive [13]. The reversibility of the reaction is also not yet achieved for all systems.

In this wide panorama a higher mass density is reachable only with light elements such as calcium and magnesium. In fact, in the case of Mg, it forms ionic $MgH_2$ that is one of the most promising hydrogen storage materials and has already been extensively studied due to its low price and high hydrogen content (7.7 wt %, 110 g/L) [14)].

However the $Mg/MgH_2$ systems suffer from slow kinetics and unfavorable thermodynamics that hamper its use in practical application for automotive purposes. For example the enthalpy of formation of the hydride ( -75 kJ/mol) corresponds to an equilibrium temperature of about 300 °C at 1 bar hydrogen pressure. In practice dehydrogenation temperatures above 400 °C are needed and they are too high for storage applications [15].

Finally, other important strategies to store hydrogen in solid state are represented by hydrocarbons that can be hydrogenated and dehydrogenated if their ratio of hydrogen to carbon atoms allows reversibility. For example Cyclohexane ($C_6H_{12}$), reversibly desorbs six hydrogen atoms (7.1 mass%) and forms benzene ($C_6H_6$) [16].

We can also consider Ammonia ($NH_3$, 5.9 mass%) as a means to release hydrogen and generate an indirect form of solid state hydrogen storage [17].

The table below shows the value in gravimetric and volumetric density of all the cited materials above.

| | gravimetric hydrogen density ($kg\,H_2\,kg^{-1}$system) (%) | volumetric hydrogen density ($kg\,H_2\,m^{-3}$ system) |
|---|---|---|
| pressure cylinder (500 bar, 25°C) | 4 | 27 |
| liquid hydrogen (1 bar, −253°C) | 3 (100%) | 40(71) |
| physisorbed hydrogen (70 bar, −200°C) | 2(4%) | 30 |
| metal hydrides (1 bar, 25°C) | 1.2 (1.85%) | 50(110) |
| complex hydrides (1 bar, 150°C) | 4 (13.5%) | 50(120) |
| metals (1 bar, 25°C) Zn ($H_2O$) | 3 (3.8%) | 90 |
| ammonia (1 bar, −33°C) | (17.6%) | (15) |
| hydrocarbons (1 bar, 25°C) | 14 (14%) | 10 |
| water (1 bar, 25°C) | 11 | 11 |

Table 1: gravimetric and volumetric density values for the main hydrogen storage systems

In particular the U.S. Department of Energy (DoE) imposed clear targets for solid storage in mobile application to be achieved by 2020 [18]:

- a gravimetric capacity of 5.5 mass% hydrogen for the tank,
- a volumetric capacity of 0.040 kg hydrogen/L

Very important also to underline are the complete reversibility, the fast kinetics together with optimized thermodynamic properties and the low cost of the storage system.

## 1.2 Carbon nanostructures materials

Among the various field of research in the wide world of solid state storage systems, this thesis is mainly focused on carbon based materials. Carbon can be a good alternative to hydrides: it is green, biocompatible and often inexpensive.
In the family of carbon nanostructures materials, two of them could be interesting for our aim: graphene and fullerene.

### 1.2.1 Graphene

Graphene is a single layer of carbon packed in a hexagonal lattice (honeycomb structure), with a C-C distance of 0.142nm [19]. It has been produced and isolated for the first time in 2004 by Geim and Novoselov from University of Manchester (UK). This is the first 2D crystal structure that has been isolated and has high physical stability thanks to the presence of double covalent bonds between the carbon atoms.

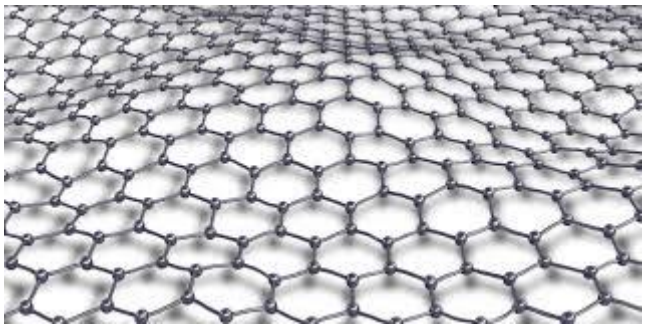

Figure 4: layer of Graphene

It constitutes the fundamental "brick" of graphite, able to theorically form many other carbon nanostructures: for example, by folding a sheet of Graphene on itself you get a nanotube, similarly you can curve it to form a closed surface obtaining the Fullerenes (see Figure 4 ).

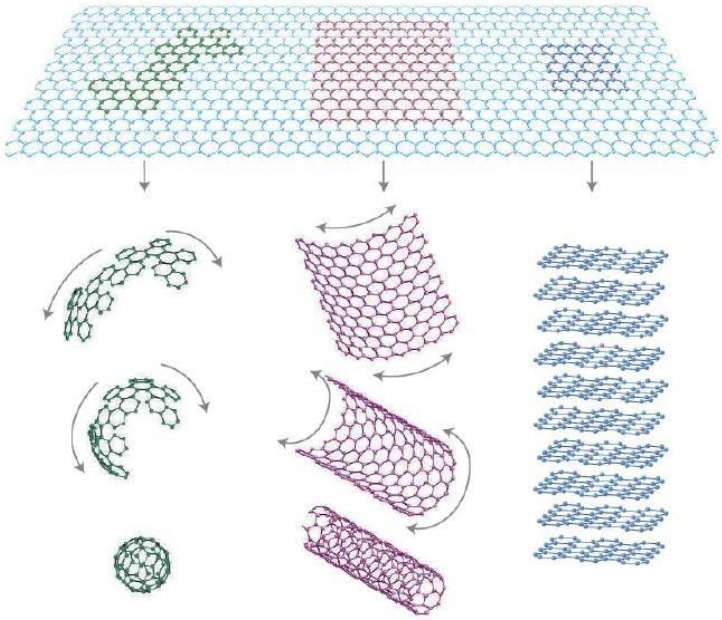

Figure 5: fullerene molecules, carbon nanotubes and graphite can all be thought of as being formed starting from a graphene sheet.

The material exhibits outstanding thermal, mechanical and electrical properties making it interesting for theoretical studies and for technological applications.

The production of graphene can occur in several ways: the starting reagents are mainly graphite and carbides.

In the case of synthesis starting from graphite, the aim is to separate the layers of carbon that are held together by Van der Waals weak interaction forces.

The most common methods used to synthesize graphene from graphite are:

- Mechanical Exfoliation [20]: it is based on exfoliation of graphite planes by applying the energy required to break the forces of cohesion between layers.

The Van der Waals interaction energy between graphite planes is $2eV/nm^2$ and the force required to exfoliation is approximately 300 $nN/\mu m^2$.

- Chemical graphene [21] ("graphene oxide"): this method allows a large scale production of Graphene. The graphite is oxidized by oxidizing agents, like concentrated acids, that introduce on the surface many organic groups, in particular hydroxylic (-OH), carboxylic (-COOH) and epoxydic ($-CHOCH_2$) groups.

The oxidized parts can be removed by reactions like chemical or thermal reduction.

- Epitaxial growth on a substrate [22]: the growth is supported and occurs under controlled atmosphere and under particular conditions of P and T.

All these synthetic ways allow to produce graphenes with very different morphologies and properties and so the strategy and the choice of the production method is a fundamental step to study graphene for many particular application.

In our case graphene is produced by a thermal exfoliation of graphite oxide.
The first step consists in the oxidation of grade RW-A graphite powder to produce graphite oxide (GO). This is obtained with the Staudenmeier or Brodie methods [23]: a treatment in nitric /sulphuric acid in presence of strong oxidizer, in our case it has been used sodium chlorate ($NaClO_3$).
GO is then exfoliated through heat shock at 1150° C under dynamic vacuum.
The treatment produces a volume expansion of the sample, which increases its initial volume up to 1000 times. This thermally expanded graphite oxide (TEGO) can be produced in gram scale and this is a suitable advantage for practical applications.

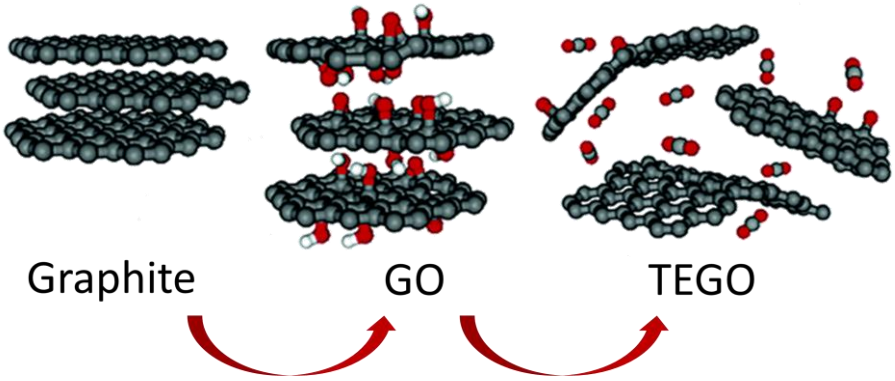


Figure 6: Principal steps in the production of TEGO

### 1.2.2 Fullerene $C_{60}$

$C_{60}$ and the fullerenes family were first discovered by Harold Kroto *et al.* [24] in 1985, studying the formation of long carbon chains in the interstellar space and it is the most common representative of the fullerene family.

The $C_{60}$ molecule presents a truncated icosahedron structure with a symmetry defined by the *Ih* point group and it's made of 20 hexagons and 12 pentagons of carbon.

It has a surface radius of about 3.56 A, but the outer diameter is increased to 10 A for the surface occupation of molecular orbitals around the carbon shell.

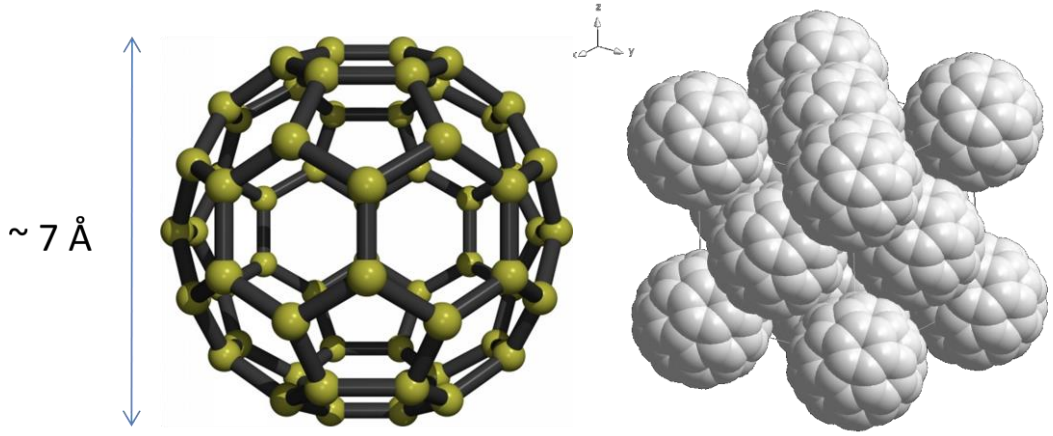


Figure 7: Schematic representation of the $C_{60}$ (left) and the crystal *fcc* structure of solid $C_{60}$

Moreover the p electrons are not homogeneously delocalized on the sphere and provide two different bonds: the edge shared by two hexagons is 1.46 A, the one between a hexagon and a pentagon is 1.40 A. The main physical properties of $C_{60}$ are reported in table 1.1.

| | |
|---|---|
| average C-C distance | 1.44 Å |
| $C_{60}$ mean diameter | 6.86 Å |
| $C_{60}$ outer v.d.W. diameter | 11.18 Å |
| $C_{60}$ inner v.d.W. diameter | 3.48 Å |
| $1^{st}$ ionization potential | 7.58 eV |
| $2^{nd}$ ionization potential | 11.5 eV |
| electron affinity | 2.65 eV |
| *fcc* lattice constant (300 K) | 14.17 Å |
| fullerite density | 1.72 g/cm$^3$ |
| $O_h$ site radius | 2.07 Å |
| $T_h$ site radius | 1.12 Å |
| thermal expansion | $6.2 \cdot 10^{-5}$ cm$^3$/K |
| Band gap | 1.6 eV |

Table 2: Main physical properties of solid C60

$C_{60}$ can be synthesized from graphite through arc-discharge in inert atmosphere.

This process generates a soot of carbon allotropes for which $C_{60}$ is the most abundant species ( 80 %) and can be easily separated using chromatography.

As shown in Fig. 7, in the solid state $C_{60}$ molecules arrange into a face centered cubic structure (space group F m3m) with a=14.17 A at room temperature and inter-fullerene distance of 10.02 A. This structure presents large octahedral (*Oh*) and tetrahedral (*Th*) voids.

Starting from 260 K the molecules are free to rotate around their center of mass in a orientationally disordered plastic crystal. When the temperature decreases under 260 K the rotation is blocked and the structure changes into a simple cubic cell (space group Pa3).

The high molecular symmetry provides two different energy scales: one is associated with the strong intramolecular covalent bonds and a weaker one due to Van der Waals soft interball binding. This feature deeply influences the electronic behavior: the solid states resemble the molecular levels with the addition of a weak splitting in narrow bands (see Fig.8) as an effect of the crystalline field.

In the ground state of the molecule, the 60 valence electrons are localized on only 7 energy states.

The $h_u$ molecular orbital level ($l$ = 5) is completely filled by the ten remaining electrons, becoming the highest occupied molecular orbital (HOMO), and the $t_{1u}$ levels become the lowest unoccupied molecular orbitals (LUMO), while the LUMO+1 levels have $t_{1g}$ symmetry. The HOMO-LUMO gap is about 2 eV. The lowest unoccupied molecular orbital (LUMO) presents a non bonding nature in agreement with the $C_{60}$ electronegative character and is triply degenerate ($t_u$ simmetry), allowing the population of $t_{1g}$ LUMO level with the possibility of reaching anion charges of $12e^-$ [25].

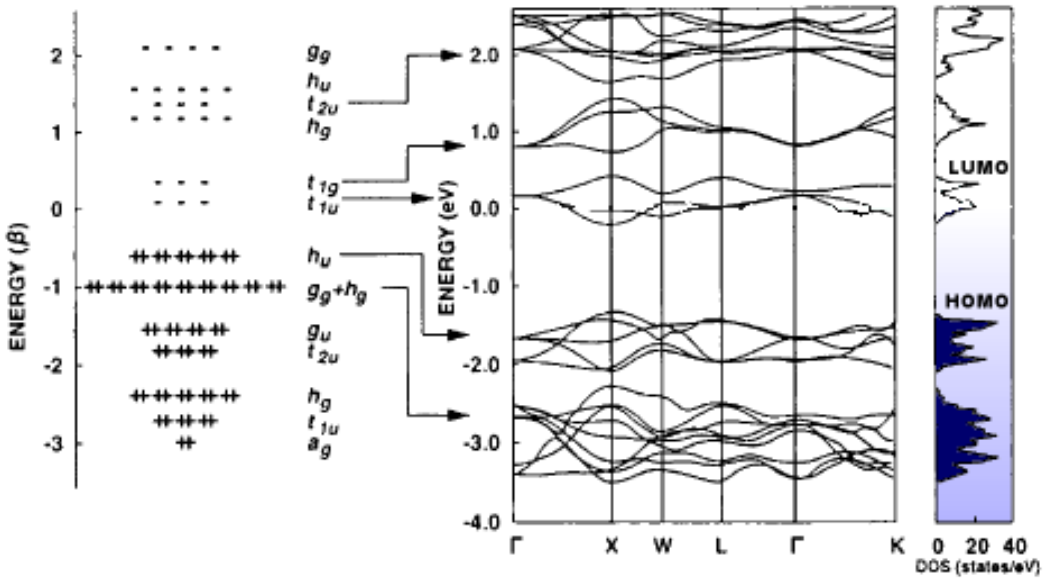


Figure 8: Scheme of molecular orbitals of $C_{60}$ and the derived electronic band structure in the molecular crystal.

### 1.2.3 The alkali intercalated fullerides

We have just explained the ability of $C_{60}$ to accept electrons on its LUMO orbitals and in particular the molecule can receive up to 6 electrons on its *t*1*u*-LUMO levels [25].

Moreover, the large intermolecular voids in the *fcc* structure can allow the diffusion of light ionic species, such as alkali and alkaline earth. The intercalation of transition metals is more difficult due to the high cohesive energy of these elements and the poor tendency to donate their charge to $C_{60}$ [26]: in these cases the synthesized solids are often amorphous or polymeric.

Since the discovery of $C_{60}$, a wide variety of intercalated fullerides were synthesized, with interesting applications in the fields of superconductivity [27] and energy storage [28].

Whereas the undoped fullerite is a semiconductor, when it is doped with electron donor atoms the conduction bands are progressively filled leading to the formation of metallic and insulating phases. Nowadays it is easily possible to synthesize a huge number of intercalated fullerides.

Our research group has widely investigated many alkali-metal intercalated fullerides for energy storage applications in the last few years introducing a new promising class of materials for hydrogen storage.

In particular Lithium and sodium intercalated systems have shown interesting and different properties as absorbent materials due to their different gravimetric and thermodynamic properties. Lithium and sodium are the smallest alkali metals and this allows a relatively easy intercalation in the fulleride lattice. Moreover, the $Li_xC_{60}$ and $Na_xC_{60}$ are the only known alkali fullerides that permit the existence of small "metallic" clusters in the *fcc* fulleride lattice, tipically obtained for an high amount of intercalated metal corresponding to a stoichiometry ratio of metal/$C_{60}$ more than 6[29].

The synthesis of these materials usually occurs via solid state synthesis and in our group mainly by chemical or physical intercalation with a process described in the figure below.

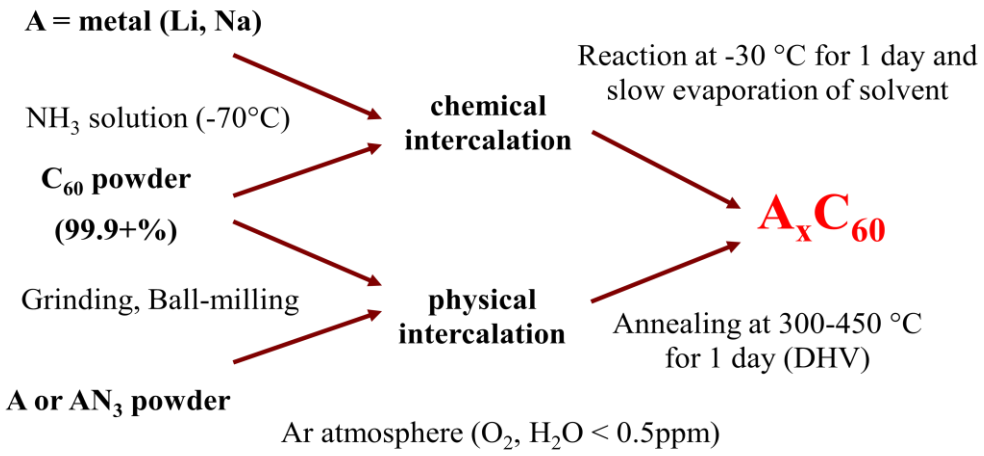


Figure 9: Main synthetic ways to produce lithium or sodium intercalated fullerides in Carbon Nanostructure Laboratory in Parma University.

As shown in Figure 9 it is possible to directly intercalate the metal or use the metal azide precursor.

In the first case $C_{60}$ powder is mixed to small pieces of metal in the stoichiometric ratio, in order to obtain typical 400-500 mg batches of powder. The grinding process takes place in a 10 ml volume agate ball-milling jar containing the sample and 3 agate spheres of 10 mm diameter ( Fritsch Mini-Mill Pulverisette 23), which is mechanically shaken at 30 Hz for 60 min (typical milling step takes 10' followed by 5' pause, in order to avoid jar overheating). The resulting black powder is then pelletized, placed in Ta foil bags, sealed under high vacuum ($<10^{-5}$ mbar) in a Pyrex vial and subsequentenly treated in a furnace at 270°C for 36h.

Following the synthetic approach using metal azide, $C_{60}$ powder is grinded with Li or Na azide powder in a mortar, pelletized and finally treated under dynamic vacuum to decompose the metal precursor releasing $N_2$.

In this thesis work we have mainly investigated two particular intercalated fullerides:
$Li_{12}C_{60}$ and $Li_6C_{60}$.
At low temperature (20 K), $Li_{12}C_{60}$ is a monoclinic crystal (space group $P2_1/c$; $a$ = 9.888(9) Å, $b$ = 9.901(8) Å, $c$ = 14.290(8) Å, $\beta$ = 89.51(6)°) where the $C_{60}$ molecules are centred in the same way of the *fcc* $C_{60}$ structure, but rotated to ~ 90° around the [001] axis of the parent cubic lattice.
This structure is characterized by the presence of a small cluster of five Li atoms (with a centred tetrahedron structure), residing in the pseudo-tetrahedral voids of the parent *fcc* lattice (see Figure 10), while the remaining two Li ions, which complete the stoichiometry, are delocalized in the remaining interstitial space [41]. Above 553 K the structure has been determined to be *fcc* (space group $Fm\bar{3}m$), with a Li cluster in the central octahedral void and the $C_{60}$ molecule characterized by rotational disorder [30].

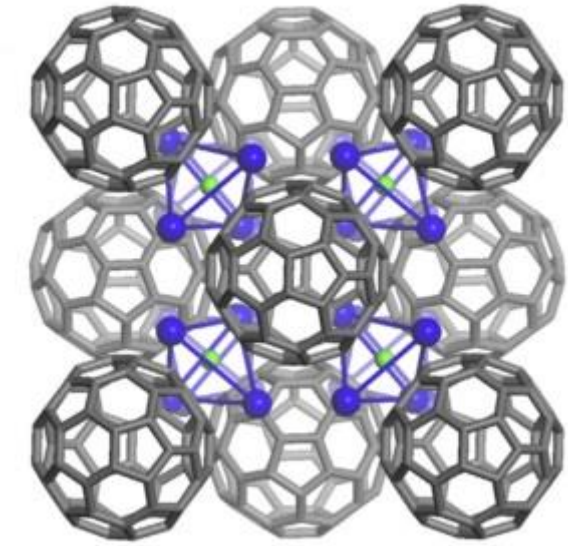

Figure 10: structure of $Li_{12}C_{60}$

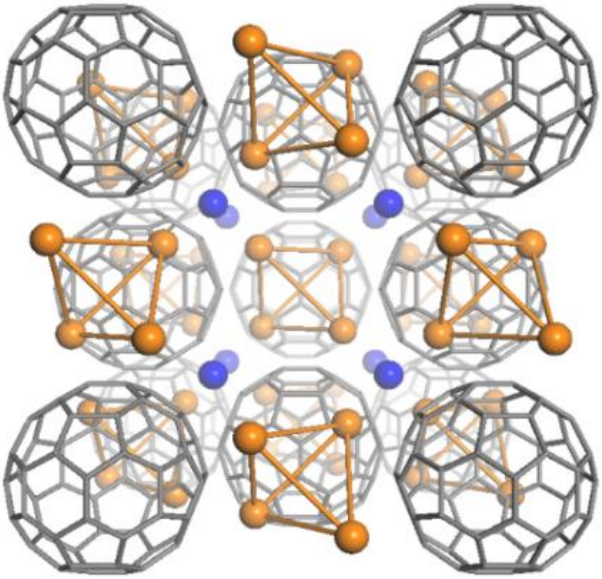

Figure 11: structure of $Li_6C_{60}$

Also In the case of $Li_6C_{60}$ [31] the structure has been determined to be a face-centered-cubic structure (space group Fm-3m $a$ = 13.86 Å) and Li clusters and ions occupies the lattice interstitial voids (Figure 11).

In this introduction we have seen the main starting materials and the aim of the research so now we need to understand and introduce their properties and behaviors in the hydrogen storage field.

### 1.3 Hydrogen Storage in Carbon Nanostructures

We have already seen that bare carbon materials are not suitable for room temperature sorption as the physical adsorption of hydrogen takes place at too small binding energies ( < 20 kJ/mol), requiring low temperatures, while the chemical absorption is too strong (> 50 kJ/mol) and requires to work at high temperatures. In order to operate around room temperature, the physical binding energies must be strengthened or the chemical binding energies must be lowered, taking advantage of particular effects that can occur when hydrogen interacts with other elements: like it happens for the Kubas binding [32] and the spillover effect [34].

The Kubas interaction involves a transition metal (M) and a hydrogen molecule and results in the formation of a dihydrogen complex formed by a three center 2-electron bond in which a molecule of $H_2$ acts as a two electron sigma donor to the metal center.
A typical dihydrogen complex is formed in the second step of the subsequent reaction:

$$L_nM + H{-}H \rightleftharpoons L_nM \longleftarrow \begin{matrix} H \\ \vdots \\ H \end{matrix} \rightleftharpoons L_nMH_2$$

where Ln represents one or more ligands (such as CO, Cl or phosphine) attached to M [33].

Whereas in the spillover process the dissociation of the hydrogen molecule and the reversible chemisorption is mediated by metal nanoparticles.
To take place, this mechanism needs a metal particle (for example a cluster of few atoms of Pt , Pd or Ni), which has to be dispersed upon an inert support (receptor or carrier). The real absorber is the receptor surface while the metal particle has the role of dissociating the incoming hydrogen molecules [35].
The process can only work if the carrier is able to allow the diffusion of hydrogen chemisorbed on its surface. The metal has the role of lowering the energy pathway for gaseous species which are firstly adsorbed by it and then diffused on the plane of the carrier.
Thanks to the diffusion of atomic hydrogen onto the carrier surface, the metal particle is always virtually free to continuously split new $H_2$ molecules.

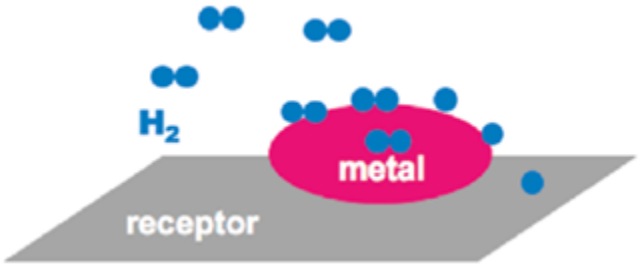


Figure 12: schematics of spillover process

Both these mechanisms involves binding energy in the range of 20-50 kJ/mol, which is the useful range to realize an efficient carbon solid state system in order to operate at room temperature.
The figure 13 shows the possible interactions that occurs between hydrogen and carbon materials with the related energies.

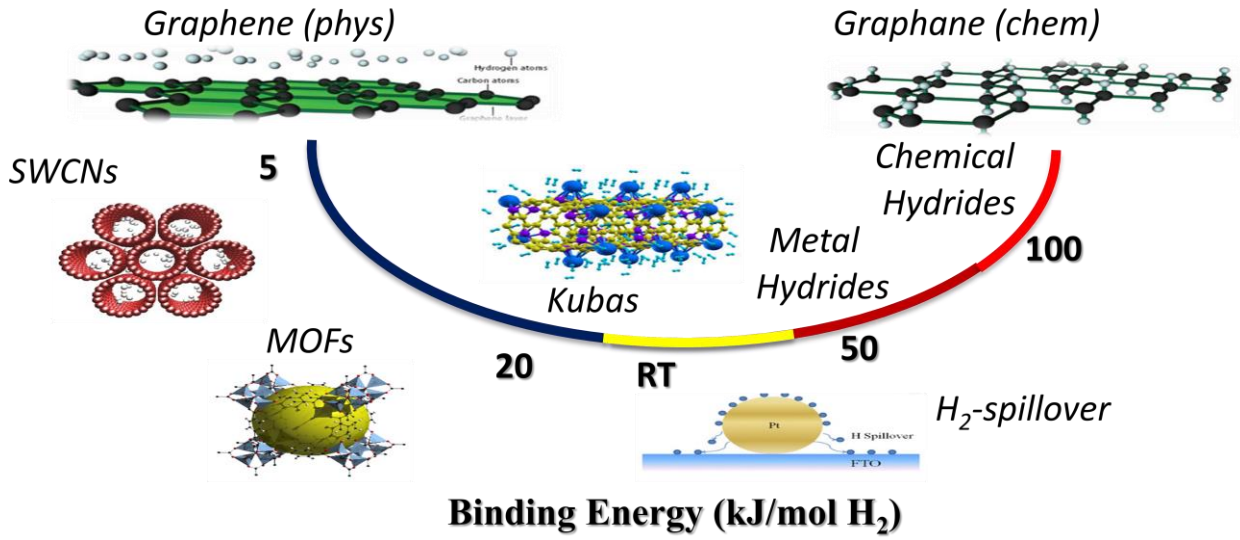


Figure 13: binding energy range required for practical solid state $H_2$ storage applications

In the case of physisorption we have introduced the importance of a high specific surface area that can increase the number of interactions of the material with the molecular hydrogen [36].
In particular the amount of physisorbed hydrogen is proportional to the surface area and in the case of carbon materials theoretical studies have calculated that this correlation at 77 K is
1.5 mass% of $H_2$ per 1,000 $m^2$ $g^{-1}$ of specific surface area (figure 14 ) [4)].

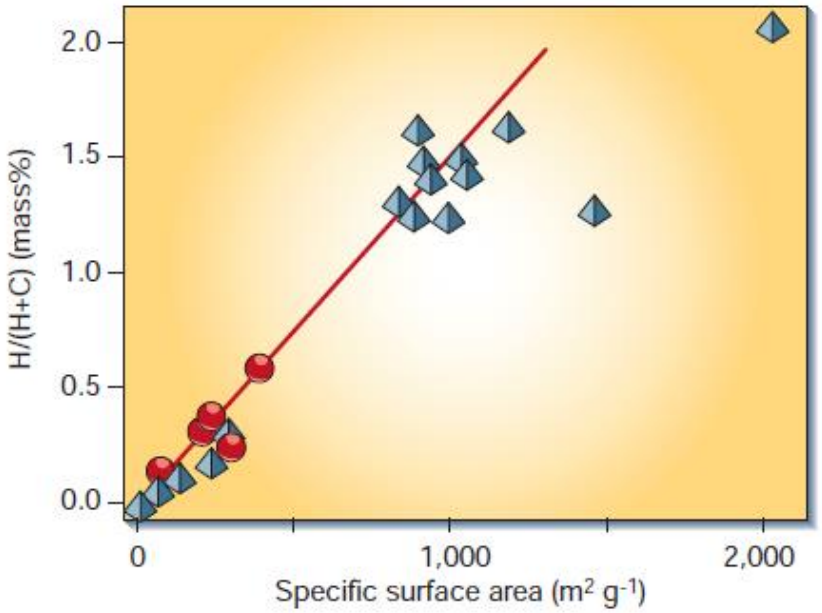


Figure 14: Reversibly stored amount of hydrogen on various carbon materials versus the specific surface area of the samples. Circles represent nanotube samples (best-fit line indicated), triangles represent other nanostructured carbon samples [36].

Other theoretical studies have shown that another important parameter is the curvature of the system [37]. Actually the binding energy of hydrogen is enhanced in curved carbon sheets.

This is due to a "transition" from the $sp^2$ hybridization of flat carbon to a partial $sp^3$ carbon hybridization, forming a curved structure with a higher number of carbon atoms interacting with the hydrogen molecule.

For this reason nanostructures like carbon nanotubes and fullerenes, which displays a high grade of $sp^3$ hybridization, are more promising candidates for this purpose.

Also the presence of metal catalyzers and charged systems has been demonstrated to improve the physisorption creating a sort of mild chemisorption.

Metal ions can in fact bind hydrogen molecules by means of orbital interactions [32] (named Kubas interaction in case of metals which possess available *d* orbitals) and similarly, light alkali metal ions can polarize the hydrogen molecule through an electrostatic interaction.

Moreover when a metallic cluster is present in the system, the spillover effect can lead to a low energy chemisorption of hydrogen atoms [34].

So if we start from a graphene plane, the binding energy of hydrogen can be optimized by operating on three factors: the curvature, the charge and the presence of a metal catalyst to allow a spillover like process.

We have found that partially ionized alkali clusters are quite suitable for this application [38] and in this thesis we investigate a spillover system in fullerene, following the prediction that a charged and curved $sp^2$ carbon could meet the suitable conditions for hydrogen absorption.

### 1.3.1 Hydrogen storage in graphene systems

Graphene seems a promising candidate for the production of hydrogen storage systems as:

– it has a large specific surface area, equivalent to 2630 $m^2/g$, theoretically predicted admitting the accessibility of both sides of graphene.

– It is lightweight and has remarkable mechanical properties (Young's modulus of 1TPa, 5 times that of steel) that guarantee durability and reliability.

– Macroscopic quantities may also be available, thanks to the development of chemical techniques to produce it in large scale.

However, theoretical calculations and experimental results have shown how graphene is able to physisorb hydrogen molecule only at low temperature (77 K), due to the high potential barrier (3.3 eV) which should overcome to dissociate $H_2$ [39].

The interaction of graphene with atomic hydrogen can instead be energetically favorable and can occur either on the plane or on the edges.
On the plane H is chemically absorbed through an exothermic process (we can only overcome a small activation energy of 0.2 eV) and forms a stable system with a binding energy of about 1 eV.
The H bond to the edges has a higher binding energy of 4 eV.
Theoretical calculations have shown that the energy with which carbon binds atomic hydrogen grows by covering the surface up to reach 6.56 eV in the case of graphene (see Figure 15) system in which all carbons are $sp^3$ and are linked to 1 hydrogen (containing 7.7 mass% of H).
Unfortunately the working temperature is too high for practical applications.

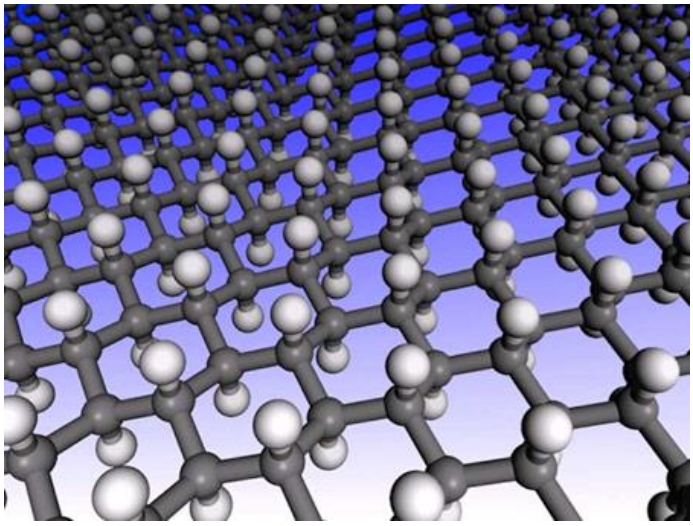

Figure 15: Graphane

However the binding energy can be optimized, for example, decorating graphene with alkali metals, alkaline earth metals or transition metals [40].

The binding energy between graphene and $H_2$ can be increased operating on two factors:

1) The polarization of the hydrogen molecule, due to the electric field generated by ionized alkali/alkaline earth atoms, can increase the physisorption binding energy.

2) A quantum-mechanical interaction (according to Kubas) which consists, in the specific case of alkaline-earth metals and transition metals, in the hybridisation of d orbitals of the metal with the hydrogen molecular orbitals.

In the second case, what we expect is that the σ bonding orbital of $H_2$ makes an hybridization with the d atomic orbitals of the metal by the retro orbital donation of antibonding
d molecular orbital σ * of $H_2$.
If this process doesn't stop, it leads to the dissociation of $H_2$ molecule and the formation of the hydride. Moreover a single metal atom can coordinate more than one molecule of hydrogen.

However the presence of metals can bring another issue: the metal atoms can form aggregates due to their high cohesion energy (of the order of 4 eV).

Nevertheless, the formation of metallic aggregates on graphene may still facilitate the absorption of hydrogen through the "spillover" phenomenon and the formation of C-H bonds mediated by metal clusters.

Nanoaggregates of Pd, Ni, Pt are known from the literature to lower the dissociation energy of the $H_2$ molecule, promoting the formation of atomic hydrogen that can interact with the active defects of graphene, like "dangling bonds".

On the other hand, the diffusion of H on graphene is another important aspect for the realization of a spillover and some recent studies suggest that this phenomenon occurs already at room temperature.
In 2014 our research group has preliminary investigated a Ni decorated graphene (TEGO) system[41], studying its hydrogen physisorption, compared to a bare graphene.
In that study the microscopy analysis demonstrated the formation of monodispersed nickel nanoparticles, of 17 nm ($\sigma$ = 4 nm) diameter, decorating the single layer graphene sheets and the presence of Ni led to a significant improvement in the amount of molecular hydrogen adsorbed at 77 K.

In fact, according to the theoretical physisoption of 1.5 mass% of $H_2$ per 1,000 $m^2/g$ of specific surface area [4], we found for our graphene system, with a specific surface area of 505 $m^2\ g^{-1}$ (theoretical adsorption 0.75 mass%), a maximum adsorption value of 1.15 mass% , 51% higher than pristine graphene at the same conditions [41].

These results shows us that the physisorption process is not so promising, mainly caused by the low amount of hydrogen sorbed. Probably better results could be obtained studying chemisorption, using metals to dissociate the hydrogen molecule.

For this reason it has been thought to optimize the catalyst nanoparticles size and in this thesis we are going to see the results obtained in the synthetic optimization of the Pt and Ni decorated graphenes.

Another possible use of graphene for hydrogen storage is to apply only as a substrate to promote the nanosizing of metal hydrides.

Now we can try to understand the advantages of this alternative approach of improving the properties of a given material by nanosizing and/or supporting that material [42].

Even if this approach is relatively new for hydrogen storage applications, it has been known for a long time in other fields such as heterogeneous catalysis, where a high surface/volume ratio is essential.

The idea of using porous materials as a support for nanosized active species is widely used in the field of catalysis. Depending on the application, a supporting material can fulfill a number of different purposes. The figure below shows a schematic overview:

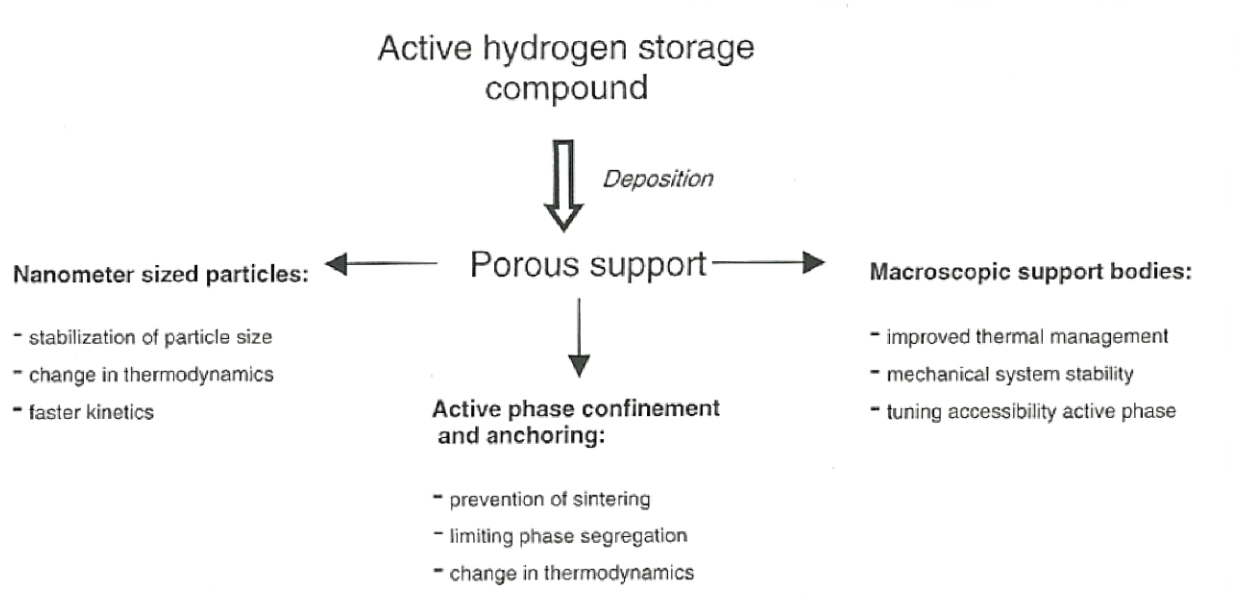


Figure 16: schematic illustration of the potential advantages of using nanoporous supports for hydrogen storage materials

Interesting material classes are unsupported clusters, nanoparticles and nanostructures, and 3D supported or scaffolded nanomaterials [43].
In general, the crystallite size of the materials discussed is below 10 nm and it's important not only to obtain these nanosized materials, but also to try to control the morphology and particle size.

However, it is well known that the fundamental physical and chemical properties of materials can change drastically when entering the nanosize regime [15] so one can expect important changes in hydrogen sorption properties such as improved kinetics and reversibility and possibly a change in thermodynamics.

For this purpose graphene is again a perfect candidate due to its outstanding morphological, physical and chemical properties.

In the experimental part of this thesis we will able to seen an example of this strategy, studying the decoration of TEGO with magnesium nanoparticles in order to produce nanostructured $MgH_2$ under hydrogen pressure directly on the surface of graphene and investigate its desorption properties.

### 1.3.2 Hydrogen storage in fullerene and fullerides

Another important part of this work has been the study of intercalated fullerides to improve their hydrogen absorber performances and understand the mechanisms involved in this process.

From the literature we know that pure $C_{60}$ can chemisorb hydrogen only at very high temperatures and the process is irreversible [44]. Only a small fraction of the absorbed hydrogen is desorbed followed by the breaking of the molecule. It has been also explained that $C_{60}$ can be easily intercalated and charged by alkali metals [29].

There is also a risk associated to this process because the alkali atom can also bind hydrogen making the hydrides which are quite stable and it would be quite hard to desorb it.

If few alkali per molecule are intercalated you synthesize fullerides, well-known for superconductivity [27], but there is no relevant improvement in terms of hydrogen absorption respect to pure $C_{60}$.

The intercalation of relatively high amounts of light alkali metals in fullerene $C_{60}$ gives fullerides in which alkali clusters occupy the octahedral interstices of the fcc lattice.
In these systems the $C_{60}$ ball acquires 6 or less charges and the clusters are only partially ionized.

In the recent past, lithium and sodium fullerides were investigated and it was demonstrated that, in the case of $Li_6C_{60}$ and $Li_{12}C_{60}$,they can reversibly absorb up to 5 wt% $H_2$ in their bare form and up to 5.9 wt% $H_2$ when doped with catalysts [45].

Coupled manometric – calorimetric measurements, showed that the overall dehydrogenation enthalpy value for $Li_6C_{60}$ is about 63 kJ/mol.
In the case of $Na_6C_{60}$ the enthalpy of reaction for the formation of $C_{60}H_{36}$ + 6NaH from $Na_6C_{60}$ was predicted to be 56 kJ/mol $H_2$ while in case of $Na_{10}C_{60}$ was measured to be 52 kJ/mol $H_2$ [38].

The onset temperature for dehydrogenation decreases from 306 °C for $Li_6C_{60}$ to about 250 °C for $Na_6C_{60}$. It is also worth pointing out that the addition of catalysts, useful for improving the kinetics of absorption and the maximum value of absorbed hydrogen, does not affect significantly the enthalpy of desorption. This is in agreement with the role of catalyst, present in form either of micro and nano-particles, in dissociating the hydrogen molecules, while the detachment of a hydrogen atom from a C-H bond in hydrofullerene depends on the lability of this bond.
From this point of view, the transition metal catalyst plays a non-local role (being dispersed in the carbon matrix), while the dehydrogenation of $C_{60}H_y$ is a local process (occurring at molecular level).

During preliminary studies we also investigated the sorption mechanism by mean of neutron diffraction and muon spin relaxation technique [46].

In these systems hydrogen mainly covalently binds to the $C_{60}$ molecule, thus forming the so-called hydrofullerene ($C_{60}H_y$, y ~ 36-48), while a minority part reacts with a fraction of the alkali metal ion (Li or Na), segregating as alkali hydride.
In situ neutron diffraction explored the hydrogen desorption process, detected the return to the (fcc) pristine structure in a reversible storage and the contemporary thermal decomposition of lithium hydride, which is formed upon lithium de-intercalation during $H_2$ uptake.

In both Li and Na fullerides, the presence of alkali clusters in the octahedral voids seems to influence the hydrogen dissociation and facilitate its chemisorption by significantly lowering the hydrogenation temperature, which is observed only at 550 °C on bare $C_{60}$. Therefore neither the Kubas, nor the electrostatic interaction seem to be the main responsible for the binding of hydrogen in $Li_6C_{60}$ and $Na_{10}C_{60}$. Unfortunately a complete understanding of the absorption/desorption processis still lacking: i.e. we need to make clear if $H_2$ dissociation is provided by intercalated ions or by charged fullerene molecules and also which is the limiting factor preventing, in both cases, a complete $C_{60}H_{60}$ hydrogenation.

Muon spin relaxation technique was recently adopted to study the initial stages of the hydrogenation mechanism in particular for $Li_6C_{60}$, $Na_{10}C_{60}$, and $Li_{12}C_{60}$ [46].
In these fullerides, muons showed that the presence of intercalated alkali-metal clusters plays an important role in the dissociation of the hydrogen molecule at moderate temperature, while the highly-charged anionic state of $C_{60}$ readily captures the atomic hydrogen. This process is even more efficient below room temperature.

Although alkali cluster intercalated fullerides nearly meet the DOE requirements in terms of hydrogen amount, the kinetic of their absorption is still not ideal. In fact after a relatively quick uptake of approximately 3 wt% for $Li_6C_{60}$ the remanent 2% is absorbed quite slowly. This slowing down, we have seen from investigation techniques, that is triggered by the formation of the hydride and the consequent reduction of the cluster size.

In order to improve the kinetics we followed two different approaches:
the first approach consisted in the decoration of the lattice with transition metals nanoparticles which are known to facilitate the $H_2$ molecule dissociation and initial investigations have shown promising results.

In particular we tried to intercalate Pd or Pt nanoparticles into the fulleride lattice. These are known to be good catalysers for hydrogen dissociation and the final amount of absorbed hydrogen raised from 5% to almost 6% for both cases and the systems work at lower temperatures [45].

Also a study using Ni nanoparticles has been performed, showing also in this case that the final amount of absorbed hydrogen reaches the DOE required value of 5.5 wt% [47].

The second approach has followed the observation that Na intercalated fullerides display a better kinetics but a lower absorbed amount of hydrogen, so we prepared fullerides intercalated with both Na and Li [48].
Part of the present thesis is aimed to provide the results of this cointercalation approach and will show the benefits of this strategy and how it is possible to control and further improve the storage properties of these materials.

## References chapter 1


1) A. Züttel, A. Borgschulte, and L. Schlapbach, Hydrogen as a future energy carrier, WILEY-VCH, Ed. WILEY-VCH, 2011.
2) Robertson, G. P.; Paul, E. A.; Harwood, R. R., Greenhouse gases in intensive agriculture: contributions of individual gases to the radiative forcing of the atmosphere. *Science* 2000, 289 (5486), 1922-1925.
3) Züttel A. et al., Hydrogen: the future energy carrier, *Phil. Trans. R. Soc. A* (2010) 368, 3329–3342
4) Schlapbach L, Züttel A. Hydrogen-storage materials for mobile applications. *Nature* 2001;414:353–8.
5) Leung W.B. et al., *Phys. Lett*., 1976, 56A, 425-426
6) Zheng, J.; Liu, X.; Xu, P.; Liu, P.; Zhao, Y.; Yang, J., Development of high pressure gaseous hydrogen storage technologies. *International Journal of Hydrogen Energy* 2012, 37 (1), 1048-1057.
7) Zhou, L.; Zhou, Y.; Sun, Y., Enhanced storage of hydrogen at the temperature of liquid nitrogen. *International Journal of Hydrogen Energy* 2004, 29 (3), 319-322 d
8) Aceves, S. M.; Espinosa-Loza, F.; Ledesma-Orozco, E.; Ross, T. O.; Weisberg, A. H.; Brunner, T. C.; Kircher, O., High-density automotive hydrogen storage with cryogenic capable pressure vessels. *International Journal of Hydrogen Energy* 2010, 35 (3), 1219-1226. d
9) Zhuxian Yang et al., Enhanced Hydrogen Storage Capacity of High Surface Area Zeolite-like Carbon Materials, *J. Am. Chem. Soc.*, 2007, *129* (6), pp 1673–1679
10) Viktor V. Struzhkin et al., Hydrogen Storage in Molecular Clathrates, *Chem. Rev*. 2007, 107, 4133−4151
11) Collins, D. J.; Zhou, H.-C., Hydrogen storage in metal–organic frameworks. *Journal of materials chemistry* 2007, 17 (30), 3154-3160.
12) Dillon, A. C. et al. Storage of hydrogen in single-walled carbon nanotubes. *Nature* 386, 377–379 (1997)
13) Schüth, F.; Bogdanović, B.; Felderhoff, M., Light metal hydrides and complex hydrides for hydrogen storage. *Chemical communications* 2004, (20), 2249-2258.
14) Zaluska A. et al., Nanocrystalline magnesium for hydrogen storage, *Journal of Alloys and Compounds* 288 (1999) 217–225
15) M. Dornheim et al., Hydrogen storage in magnesium-based hydrides and hydride composites, *Scripta Mater*., vol. 56, 841846 (2007)
16) Cacciola G. et al., Cyclohexane as a liquid phase carrier in hydrogen storage and transport, *Int. J. Hydrogen Energy*, Vol. 9, No. 5, pp. 411-419, 1984
17) Asbjørn Klerke et al., Ammonia for hydrogen storage: challenges and opportunities, *J. Mater. Chem.*, 2008,18, 2304-2310
18) U.S. Department of Energy (DOE), "Hydrogen and Fuel Cells Program Plan," internet version: [http://www.hydrogen.energy.gov/pdfs/program_plan2011.pdf], 2011.
19) K. S. Novoselov, et al. *Science a*, 666 (2004)
20) Liang, Z. Fu, and S. Y. Chou, Nano Lett. 7, 3840 (2007)
21) Cai M., et al., Methods of graphite exfoliation. *J. Mater. Chem.* 24992–25002 (2012).
22) Keun Soo Kim, Yue Zhao, *Nature* Vol. 457, 706 (2009)
23) Brodie, B. C. Sur Le Poids Atomique Du Graphite. *Ann. Chim. Phys*. 1860, 59, 466–472
24) H.W. Kroto et al., "C60: Buckminsterfullerene," *Nature*, vol.318, no. 6042, pp. 162–163, Nov. 1985.
25) W. Kratschmer et al., Solid c60: a new form of carbon, *Nature*, vol. 347, 354 (1990)
26) Xiao Ming Liu et al, *Nano Lett*. 2013, 13, 137−141

27) Y. Iwasa and T. Takenobu, "Superconductivity, MottÂ Hubbard states, and molecular orbital order in intercalated fullerides," *Journal of Physics: Condensed Matter*, vol. 15, no. 13, pp. R495–R519, Apr. 2003
28) D. Pontiroli et al., "Ionic conductivity in the Mg intercalated fullerene polymer Mg2C60," *Carbon*,vol. 51, pp. 143–147, Jan. 2013
29) Teprovich JA et al., Synthesis and characterization of a lithium-doped fullerane (Li(x)–C60–H(y)) for reversible hydrogen storage. *Nano Lett* 2012;12:582–9
30) Giglio F. et al., Li12C60: a lithium clusters intercalated fulleride. *Chem Phys Lett* 2014;609:155–60.
31) M. Riccò, M. Belli, D. Pontiroli, *et al.*; Phys. Rev. B 75 (2007) 081401
32) G. J. Kubas, "Metal-dihydrogen and σ-bond coordination: the consummate extension of the Dewar-Chatt-Duncanson model for metal-olefin π bonding," *Journal of Organometallic Chemistr* ,vol. 635, no. 1-2, pp. 37–68, Oct. 2001.
33) T. Hoang and D. Antonelli, Exploiting the kubas interaction in the design of hydrogen storage materials, *Adv. Mater*., vol. 21, no. 18, 1787 (2009)
34) A. Singh, M. Ribas, and B. Yakobson, "H-spillover through the catalyst saturation: An ab initio thermodynamics study,"*Acs Nano*, vol. 3, no. 7, pp. 1657–62, Jul. 2009.
35) P. A. Sermon and G. C. Bond, "Hydrogen Spillover," *Catalysis Reviews*, vol. 8, no. 1, pp. 211–239, Jan. 1974.
36) G Nijkamp, M. G., Raaymakers, J. E. M. J., Van Dillen, A. J. & De Jong, K. P. Hydrogen storage using physisorption—materials demands. *Appl. Phys. A* 72, 619–623 (2001).
37) Stan, G. & Cole, M. W. Hydrogen adsorption in nanotubes. *J. Low Temp. Phys*. 110, 539–544 (1998)
38) Mauron, P et al., Hydrogen Desorption Kinetics in Metal Intercalated Fullerides. *J. Phys. Chem. C* 2015, 119, 1714−1719.
39) Miura, Y.; Kasai, H.; Dino, W.; Nakanishi, H.; Sugimoto, T. First principles studies for the dissociative adsorption of $H_2$ on graphene. *J. of Appl. Phys*. 2003, 93, 3395–3400
40) Grafene coi metalli
41) Gaboardi, M et al., Decoration of Graphene with Nickel Nanoparticles: Study of the Interaction with Hydrogen, *J. Mater. Chem. A* 2014, 2 (4), 1039
42) Pundt, A., Hydrogen in Nano-sized Metals. *Advanced Engineering Materials* 2004, 6 (1-2), 11-21.
43) Nielsen, T. K.; Manickam, K.; Hirscher, M.; Besenbacher, F.; Jensen, T. R., Confinement of $MgH_2$ nanoclusters within nanoporous aerogel scaffold materials. *ACS nano* 2009, 3 (11), 3521-3528.
44) P. Mauron et al.,"Reversible hydrogen absorption in sodium intercalated fullerenes," *International Journal of Hydrogen Energy*, vol. 37, no. 19, pp. 14 307–14 314, Oct. 2012.
45) Aramini, M et al., Addition of Transition Metals to Lithium Intercalated Fullerides Enhances Hydrogen Storage Properties. *Int. J. Hydrogen Energy* 2014, 39, 2124−2131
46) Aramini M, Gaboardi M, Vlahopoulou G, Pontiroli D, Cavallari C, Milanese C, et al. Muon spin relaxation reveals the hydrogen storage mechanism in light alkali metal fullerides. *Carbon N Y* 2014;67:92–7.
47) M. Aramini, G. Magnani et al., Nickel Addition to Lithium Intercalated Fullerides: Synthesis and Hydrogen Storage Properties, manuscript in preparation
48) M. Gaboardi, G. Magnani et al.; Catalytic effect of sodium in the hydrogen storage of NaxLi6-xC60; http://arxiv.org/abs/1611.06512

**Chapter 2**

# Experimental techniques

The aim of this chapter is to describe the range of analytical techniques and methods used to characterize the materials synthesized during this thesis work.

## 2.1 X- ray diffraction (XRD)

X-ray powder diffraction (XRD) is a rapid analytical technique primarily used for phase identification of a crystalline material. It provides information on the crystal symmetry and on the atomic arrangement in the unit cell.
This technique has been discovered by Max von Laue in 1912, which understood that crystalline substances act as three-dimensional diffraction gratings for X-ray whose wavelength is comparable with the atomic planes distance in a crystal lattice.
X-ray diffraction is based on constructive interference of monochromatic X-rays diffused by the crystalline sample. These X-rays are generally generated by an X-ray tube, filtered to produce monochromatic radiation, collimated and directed toward the sample.
The interaction of the incident rays with the sample produces constructive interference and a diffracted ray when conditions satisfy the Bragg's Law:

$$n\lambda = 2d \sin \theta.$$

This law relates the wavelength $\lambda$ of electromagnetic radiation to the diffraction angle $\theta$ and the lattice spacing $d$ of a set of atomic planes in a crystalline sample. The position and intensity of diffracted X-rays are measured by a detector, which in a powder diffraction experiment, moves around the sample scanning a range of $2\theta$ angles; the diffraction peaks are detected whenever the detector intersects the Debye-Scherrer cones generated by the samples, due to the random orientation of the powdered material.
By using the Bragg's law, it is possible to put in relationship the diffraction peaks with d-spacings allowing the identification of the materials by comparison of d-spacings with standard reference patterns, because each element has a set of unique d-spacings.
More in detail, X-rays are generated in a cathode ray tube by heating a filament to produce electrons, accelerating the electrons toward a target by applying a voltage, and bombarding the target material with electrons. When electrons have sufficient energy to dislodge inner shell electrons of the target material, characteristic X-ray spectra are produced. These spectra consist of several components, the most common being $K_\alpha$ and $K_\beta$. $K_\alpha$ consists, in part, of $K_{\alpha1}$ and $K_{\alpha2}$. $K_{\alpha1}$ has a slightly shorter wavelength and twice the intensity as $K_{\alpha2}$. The specific wavelengths are

characteristic of the target material (Cu, Fe, Mo, Cr). Filtering, by foils or crystal monochromators, is required to produce monochromatic X-rays needed for diffraction. $K_{\alpha 1}$and $K_{\alpha 2}$ are sufficiently close in wavelength such that a weighted average of the two is used.
A detector records and processes this X-ray signal and converts the signal to a count rate which is then output to a device such as a computer monitor.

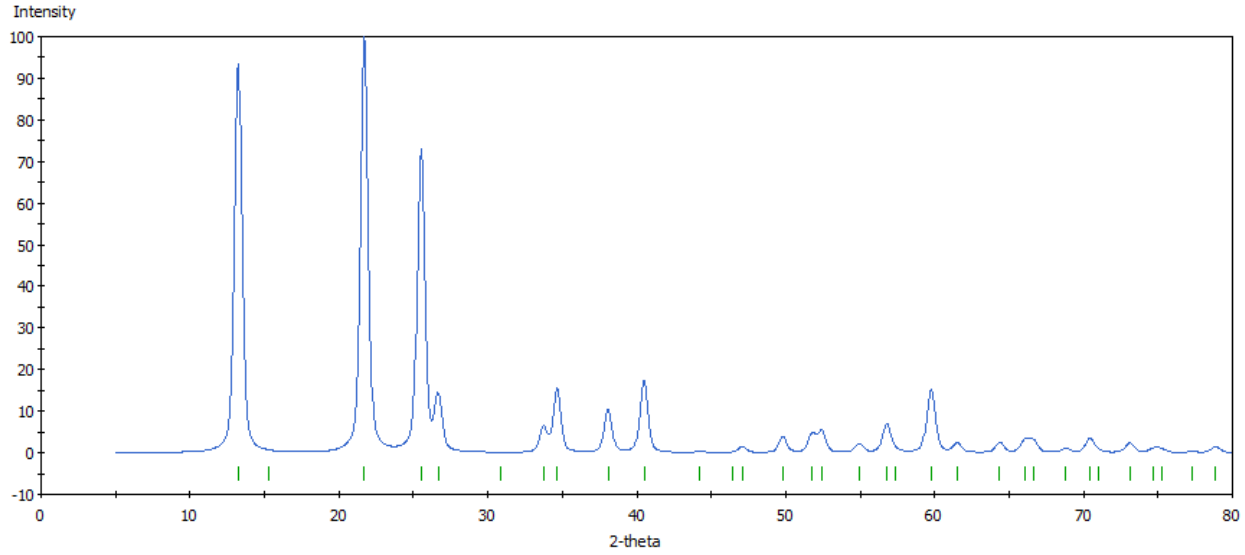


Figure 17: example of a diffractogram of $C_{60}$

The geometry of an X-ray diffractometer is such that the sample rotates in the path of the collimated X-ray beam at an angle θ while the X-ray detector is mounted on an arm to collect the diffracted X-rays and rotates at an angle of 2θ. The instrument used to maintain the angle and rotate the sample is termed a goniometer. For typical powder patterns, data is collected at 2θ from ~5° to 70°, angles that are preset in the X-ray scan.

The synthesized samples have been analyzed using a Bruker D8 discover diffractometer, operating in Debye-Scherrer geometry and using a sealed tube generator ($CuK_\alpha$) and a 2D detector (GADDS). The beam is monochromatized and collimated by double cross-coupled Göbel mirrors, inserted between the generator and the specimen. This allows to select just the $K_\alpha 1$ line of copper ($\lambda$ = 1.540612 Å).
The diffracted beam is detected by a 2-dimensional HI-STAR area detector: this is a multi wire proportional counter (MWPC) of 11.5 cm diameter.
The 2D image acquired on the detector is processed by the GADDS program and integrated.
The Debye-Scherrer geometry allows to analyze also small quantities of sample.
These small quantities of investigated air sensitive sample powder are in general introduced in a sealed glass (or quartz) capillary, avoiding the exposition to external atmosphere.
The main disadvantage of this diffractometer is presented by the low angular resolution

in $2\theta$ (~0.05° with detector at distance of 20 cm from the specimen), which is intrinsically linked to the density of wires in the detector's chamber.

Figure 18: Bruker D8 discover diffractometer

## 2.2 Neutron scattering experiments

The neutron is a powerful probe for the study of condensed matter, and has significant advantages over other techniques for the study of the microscopic structure and dynamics of matter.
Neutron scattering gives detailed information about the microscopic behavior of condensed matter, playing a major role in shaping the experimental and theoretical understanding of materials ranging from magnetism and superconductivity to chemical surfaces and interfaces.
A neutron is an uncharged (electrically neutral) subatomic particle with mass 1,839 times that of the electron. Neutrons are stable when bound in an atomic nucleus, whilst having a mean lifetime of approximately 1000 seconds as a free particle. The neutron and the proton form nearly the entire mass of atomic nuclei, so they are both called nucleons.
Neutrons scatter from materials by interacting with the nucleus of an atom rather than the electron cloud. This means that the scattering power (cross-section) of an atom is not strongly related to its atomic number, unlike X-rays where the scattering power increases in proportion to the number of electrons in the atom.

This has three advantages:

1) it is easier to detect light atoms, such as hydrogen

2) neighbouring elements in the periodic table generally have substantially different scattering cross sections and can be distinguished,

3) the nuclear dependence of scattering allows isotopes of the same element to have substantially different scattering lengths for neutrons. Isotopic substitution can be used to label different parts of the molecules making up a material.

Neutrons have wavelengths similar to atomic distances, permitting diffraction measurements to be performed.

### 2.2.1 Neutron diffraction

Neutron diffraction provides information on the location of atoms within a sample, which may be a single crystal, a polycrystalline powder, a glass, a liquid or even a gas. Single crystal diffraction and powder diffraction may be used to reveal the positions of the atoms within the unit cell of a crystalline material. For a disordered material, total diffraction is used to determine the atomic correlation function. Neutron diffraction also provides information on the location and orientation of the magnetic moments in a magnetic material.

Neutron diffraction is of use for the study of physical phenomena within a sample, as well as for studying the atomic structure itself.

The wave-like properties of the neutron were first demonstrated, by means of diffraction, by Mitchell and Powers in 1936.
When a beam of radiation is incident on a crystalline sample, interference effects between wavefronts scattered from the regular array of atoms in the material produce a diffraction pattern characteristic to that material.
Measurement and analysis of this diffraction pattern allows the locations of the atoms in the material to be determined.
When the path length difference between waves scattered from successive layers of atoms is a whole number of wavelengths, constructive interference gives rise to Bragg Reflections only in certain well-defined directions. If a single crystal sample is placed in the beam, then scattered beams are observed in any direction for which Bragg's Law is satisfied by some set of Bragg planes.
Therefore, knowing the wavelength, $\lambda$, and the angle between the transmitted and scattered beam directions, $2\theta$, we can calculate the interplanar d-spacings, and hence determine the dimensions and symmetry of the unit cell.
From the de Broglie relationship, $\lambda = h / mv$ it can be seen that neutrons with thermal energies have associated wavelengths of the order of interatomic separations.
A typical thermal neutron with a velocity of 2200 $ms^{-1}$ has an energy E = 25 meV (given by its kinetic energy, $\frac{1}{2} mv^2$) and a wavelength $\lambda$ = 1.8 Å.
Thus, neutron diffraction experiments can be used to investigate crystal structures in a manner analogous to X ray diffraction.
In an X-ray or electron diffraction experiment the radiation is scattered by the electrons surrounding the nuclei and an electron density map is obtained, from which the positions of the nuclei can be deduced. Neutrons, however, are scattered by the nuclei themselves, and thus a neutron diffraction experiment gives a direct measurement of nuclear positions.

In this thesis we have used this technique, mainly to study the structure and the phase transitions of fullerides.
In particular using neutron diffraction instead of X ray diffraction can solve many problems connected to our investigated carbon nanostructures based systems.
First of all, carbon is a light element and this affects its X-rays scattering cross section (which is proportional to the atomic number) weakening the signal, especially with laboratory X-ray sources. This problem can be easily overcome by acquiring for longer time.
Fullerides of light alkali metals have the same problem. In particular, Li is very difficult to localize both with laboratory and synchrotron sources of X-rays. By using neutrons, instead of X-rays, one can overcome some drawbacks. For example, carbon owns a good coherent cross section and zero

incoherent cross section. Hydrogen is practically invisible with X-rays (only in some cases a depth analysis with synchrotron light can give more information) and with neutrons the incoherent signal completely cover the coherent one.

| Isotope | Coh. xs (barn) | Inc. xs barn |
|---|---|---|
| $^{1}H$ | 1.7583 | 80.27 |
| D | 5.592 | 2.05 |
| $^{12}C$ | 5.559 | 0 |
| $^{7}Li$ | 0.619 | 0.78 |
| Na | 1.66 | 1.62 |

Table 3: table of coherent and incoherent neutron cross section (xs) of the most representative isotopes for this thesis.

However, is possible to obtain structural information by replacing hydrogen with deuterium, whose coherent cross section is more than double that the incoherent one. In table 3 the neutron cross section are reported for $^{1}H$, $^{2}H$ (or D), Na and the most abundant isotopes of carbon and lithium.
It turns out that lithium is hardly visible with both neutrons and X-rays diffraction.
Another problem of fullerene systems is the presence of intrinsic disorder: after the unit cell is found, the center of mass of $C_{60}$ can be easily localized but its orientation is never obvious and often merohedral disorder occurs. Moreover, an amorphous phase is always present in fullerites, which affects the background signal.

### 2.2.2 Inelastic neutron scattering (INS)

When a neutron interacts with a nucleus, it can be either absorbed or scattered, in the latter case its energy and/or trajectory can be affected. The relatively weak energy of the thermal neutrons used in a neutron scattering experiment (in the order of few meV) prevents the excitations of the internal nuclear levels and core electronic states, but is responsible for the sensitivity of the neutrons to the global dynamics of the material under study.
The neutron-nucleus interaction is characterized by a scattering length, which can be a complex quantity for an absorbing material and which quantifies the capacity of an isotope to interact with the neutron beam.
This interaction depends on the total spin state J = I + S of the neutron-nucleus system (with I the nucleus spin and S that of the neutron). The scattering length therefore varies from one chemical species to another, but also from one isotope to another within the same species.
In the elastic neutron scattering the energy of the incoming neutron does not change after being scattered from the sample whereas in inelastic neutron scattering the energy of the scattered neutrons are different from those of the incoming neutrons.

Hence, by contrast to elastic scattering, a part of the kinetic energy of the neutrons is transferred to the sample for inelastic scattering.

An example of inelastic neutron scattering spectrometer is given in the figure 19.
The analysis of an inelastic spectrum provides information on the energy levels of the sample under study. These levels can be magnetic (crystal field, spin waves), and/or nuclear.
In the latter case they reflect the fluctuations of the atomic positions in the system, which vary with the thermodynamics conditions (P, T) of the sample. The time (and space) periodic variations of the atomic positions will reflect the interactions at stake in the sample.
In our systems the coherent part of the scattering originates essentially from carbon contributions and will develop the incoherent term as if originating uniquely from hydrogen atoms.
Also, when metal decorated graphene or metal intercalated fullerides are considered, the contribution of the metallic particles should be included. In particular, Ni, Li and Na atoms have coherent and incoherent cross sections which should be taken into account in the interpretation of their spectra.

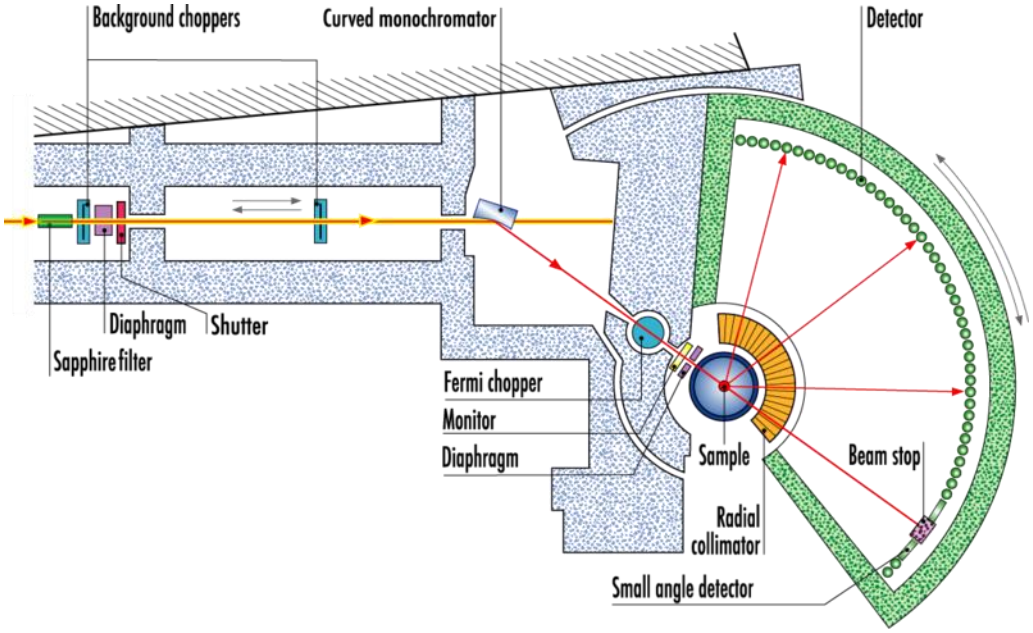


Figure 19: layout of the IN4C [4)] time of flight spectrometer (ILL, Grenoble) used for our investigations.

## 2.3 Muon Spin Relaxation (μSR)

μSR technique uses the muon spin to look at structural and dynamical processes in the bulk of a material on an atomic scale by probing the local magnetic field.
In general it is mainly used to study magnetic and superconducting materials, but is also used to study charge transport, proton diffusion, and the chemistry of muon radicals.
It is a really promising and useful alternative technique for the study of hydrogen storage materials thanks to the production, in many systems, of Muonium.
In a muon spin rotation experiment a beam of spin polarized positive muons is implanted in the sample. The muon makes a precession under the influence of a local magnetic field and, in case, of an external applied field.
After an average mean lifetime of 2.2 μS the muons decay into a positron and two neutrinos. Thanks to the parity non conserving decay of the muon, the positron is emitted preferentially in the direction of the muon spin. The incoming muon and the outgoing positron can be revealed by two detectors (Figure 22).
If we plot the number of events as a function of the residence time we see that the muon decay curve is modulated by the muon precession frequency, so we can get something very similar to the NMR free induction decay.
μSR is useful for studying hydrogen storage materials because if your sample is not a metal, in which muon potential is screened by the conduction electrons, during its thermalization process the muon binds to an electron and makes muonium.
Muonium is an isotope of hydrogen, totally equivalent from the chemical point of view.
So in this case, a μSR experiment is equivalent of implanting a single hydrogen atom in your sample and following its behavior by measuring the muon spin evolution.

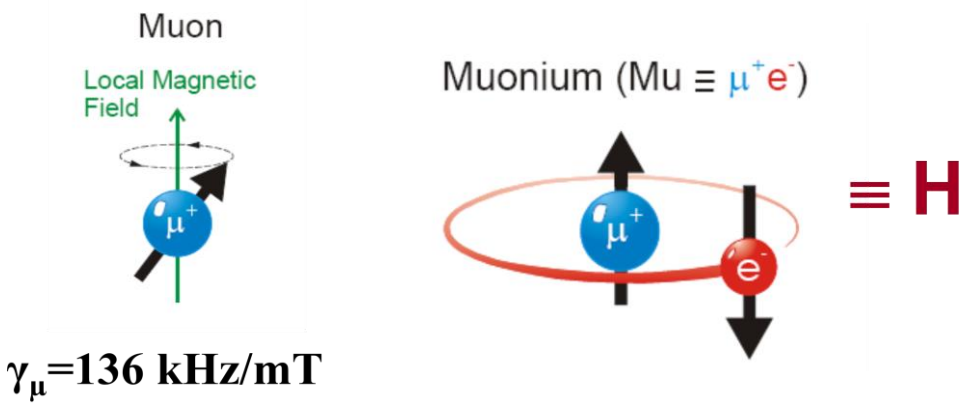


Figure 20: (left) muon spins are forced to precess around a local magnetic field with their Larmor frequency (magnetogyric ratio= 136 kHz/mT);
(right) Muonium

Although muons are produced in a variety of high-energy processes and elementary particle decays, μSR requires low energy muons that will stop in the samples being studied. Low energy muons are available at the required energy only from ordinary two-body pion decay. Thus, before making a source of muons, one must make pions. Pions are produced in sufficient amount from collisions of high-energy protons (>500 MeV) with the nuclei of an intermediate target.
A light element such as carbon or beryllium is used for the primary target in order to maximize pion production, while minimizing multiple scattering of the proton beam. The charged pions that are produced live for only about 26 billionths of a second and then decay into a muon and muon neutrino (antineutrino).

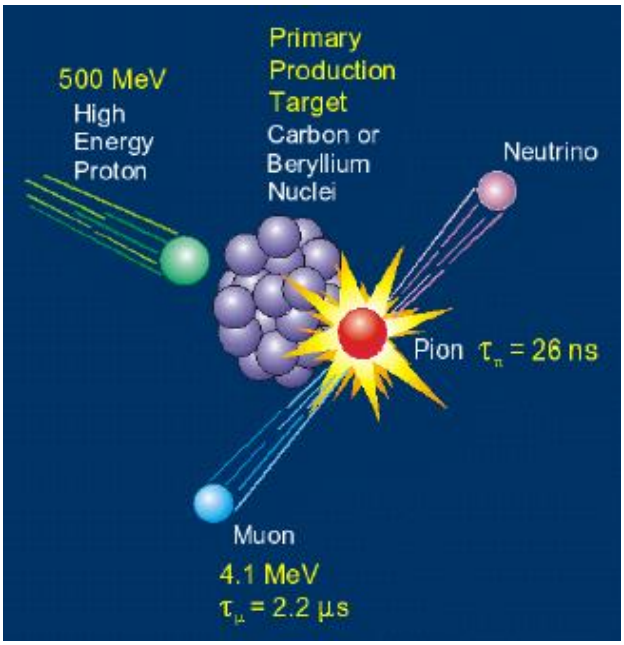


Figure 21: muon production

μSR is made possible by the unique properties of the pion and muon decays:

- surface muons are perfectly spin polarised opposite to their momenta

For this reason when a muon is transported down the beam line to stop in the sample being studied, it arrives nearly 100% spin polarized. This is a significant improvement with respect to nuclear magnetic resonance (NMR) or electron spin resonance (ESR) that must rely upon thermal equilibrium spin polarization in a magnetic field so that sufficient polarization is often achieved only at low temperatures and/or in strong magnetic fields.

- when the muon decays it emits a fast decay positron (electron) preferentially along the direction of its spin.

From a single decay positron we cannot be certain which direction the muon spin is pointing in the sample. However, by measuring the anisotropic distribution of the decay positrons from a bunch of

muons deposited at the same conditions, one can determine the statistical average direction of the spin polarisation of the muon ensemble.
The time evolution of the muon spin polarisation depends sensitively on the spatial distribution and dynamical fluctuations of the muons magnetic environment.

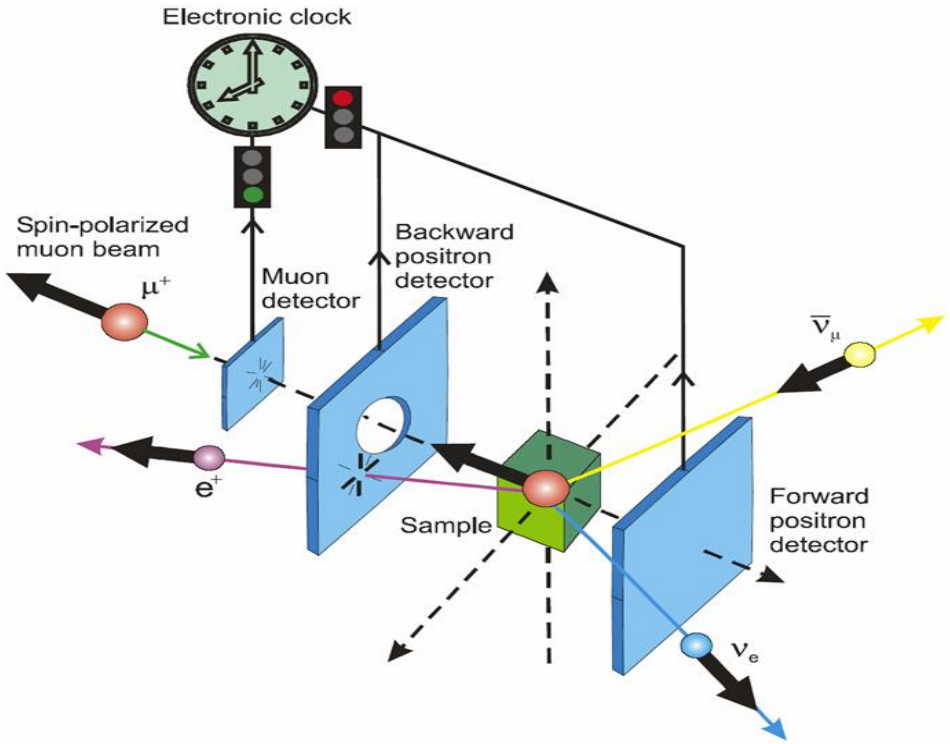


Figure 22: ZF-μSR experiment schematic representation.
The detectors are organized in two groups, forward and backward

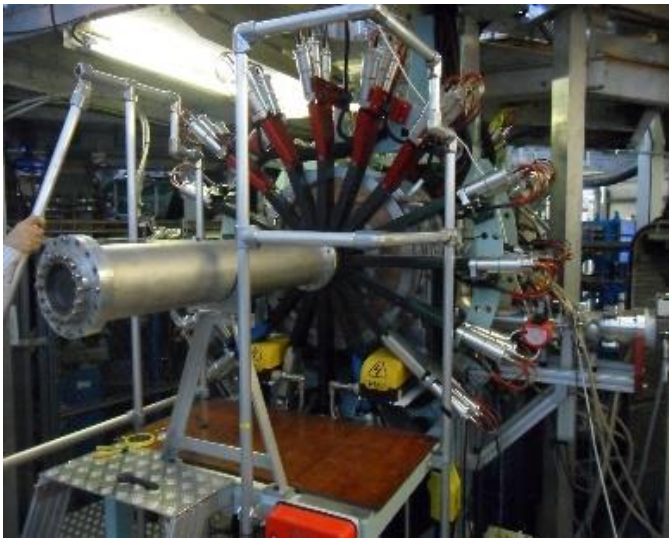

Figure 23: picture of EMU instrument at ISIS (UK)

In this work the μSR measurements were done at the Rutherford Appleton Laboratory near Oxford in the UK. The ISIS facility is the World's most intense source of pulsed muons (single pulse of 80 nm FWHM, beamsize tunable from 10-27 mm FWHM) for condensed matter research.

## 2.4. Transmission Electron Microscopy analysis (TEM)

Transmission electron microscopes produce two-dimensional, images and can determine the positions of atoms within materials, making this technique a fundamental tool for morphological and composition studies. For this reason it has a large use in nanotechnologies research and development in many fields, including heterogeneous catalysis and we have extensively used it in the study of metal decoration of graphene and more in general to investigate nanoparticles in our systems. This instrument can give several different information as it is explained in the following part. In this thesis we have used mainly HRTEM and STEM analysis, but also the other possible TEM applications are very useful and interesting in the study of the carbon nanostructures field.

### 2.4.1 High-resolution TEM (HRTEM)

High-resolution TEM in general refers to imaging in which lattice fringes (i.e. crystallographic planes) are observed or atomic resolution is achieved. HRTEM images are formed from a number of diffracted beams; this multi-beam approach is known as phase-contrast imaging, and is necessary to construct an image of the crystal lattice. HRTEM provides access to much information about the sample, such as analyzing crystalline defects and interfaces at the atomic scale, and observing and verifying devices, multilayers, nanocrystals and nanostructures.

### 2.4.2 Scanning TEM (STEM)

The condenser lens system of the microscope is used to focus a small electron probe on the sample. Scan coils then raster the probe across the sample (similarly to Scanning electron microscopy SEM). While a central bright-field detector may exist, images from an annular dark field (ADF) detector are usually of more interest. Such ADF images, formed from electrons incoherently scattered at high angles, have image intensities dependent on sample thickness and atomic number ("Z contrast" images).

These images can therefore give good compositional contrast, for instance of heavy catalyst particles on light supports, or of multilayers made from different materials.

When combined with EDXS or EELS, STEM becomes a powerful technique for analyzing compositional variations on nanometric to micrometric scales.

Unlike the TEM, where the electrons in the primary beam are transmitted through the sample, the Scanning Electron Microscope (SEM) produces images by detecting secondary electrons which are emitted from the surface due to excitation by the primary electron beam. In the SEM, the electron beam is scanned across the surface of the sample in a raster pattern, with detectors building up an image by mapping the detected signals with beam position.

TEM resolution is about an order of magnitude better than the SEM resolution. In the SEM, we use much lower accelerating voltages to prevent beam penetration into the sample since what we require is generation of the secondary electrons from the true surface structure of a sample.

### 2.4.3 Energy-dispersive X-ray (EDX) spectroscopy

This is a compositional analysis technique. The high energy electron beam can eject electrons from inner-shell atomic orbitals. The resulting vacancies are filled by electrons from higher energy shells ; electron energies lost during these transitions are emitted as X-rays. The transitions, and hence X-rays, have energies that are characteristic of the atomic species. Therefore, measuring the X-ray spectrum allows identification of the sample composition, and is typically sensitive down to levels of about 0.5 to 1 atomic percent. Quantification of composition is relatively straightforward for elements heavier than sodium. While lighter elements can be detected, e.g. from boron or carbon upwards, sensitivity to them is low, thus making quantification difficult. In general, spectral analysis must account for possible artefacts such as emission of X-rays from Cu grids or microscope pole pieces induced by back-scattered electrons, and peak overlap from the limited spectral resolution. When combined with STEM, EDX compositional line-scans and maps can be taken.

### 2.4.5 Electron energy-loss spectroscopy (EELS)

Inelastic scattering by the TEM specimen results in energy losses of the electron beam that are measured in the electron energy-loss spectrum. At low energy losses (e.g. < 50 eV), energy loss is mainly due to interactions with oscillations of weakly-bound electrons ("plasmons") in the specimen. Intensity in this region of the specimen can, for instance, give information on sample optical properties. At higher energy losses, inner-shell ionization events produce intensity edges in the energy-loss spectrum that are atomically characteristic, and can therefore be used for elemental analysis. Compared to EDX, the better collection efficiency of the EEL spectrometer can allow shorter spectral acquisition times for compositional line-scans or mapping in STEM mode. However, compositional quantification is more complicated and less accurate than for EDX, especially if there is overlap of edges from different elements (i.e. it is not a "push button" technique). Nevertheless, EELS is often more chemically sensitive than EDX, and further provides better identification/quantification of low atomic number elements such as carbon or oxygen. Additionally, measurement of the fine structure of the ionization edge spectrum can be used to analyze atomic bonding states or valency for many elements. Specimen thickness, relative to the inelastic scattering mean-free path, is also be easily determined from the EEL spectrum.

For this thesis work has been used a JEOL instrument, model JEM-2200FS, able to operate at 200 kV (point resolution of 0.19 nm) in collaboration with IMEM-CNR in Parma (IT).

To perform these measurements the graphene samples have been solubilized in degassed isopropanol solvent, sonicated to promote layers separation and finally the solution has been deposited on an amorphous carbon grid.
In the case of TEM analysis performed in Australia to analyzed Mg decorated graphene (Chapter ), it has been used a Phillips CM200 microscope operating with an electrons energy of 200 keV.

Figure 24: image of JEOL instrument JEM-2200FS (IMEM CNR Parma)

## 2.5 Scanning Electron Microscopy (SEM)

The scanning electron microscope (Figure 25) is another instrument able to study the sample morphology. It is an electron microscope that images the sample surface by scanning it with a high energy beam of electrons.

Conventional light microscopes use a series of glass lenses to bend light waves and create a magnified image while the scanning electron microscope creates the magnified by using electrons instead of light waves.

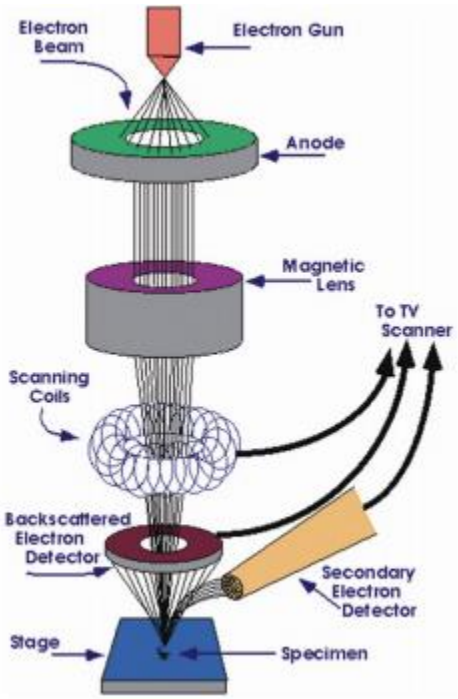


Figure 25: schematic diagram of SEM

When the beam of electrons strikes the surface of the specimen and interacts with the atoms of the sample, signals in the form of secondary electrons, back scattered electrons and characteristic X-rays are generated that contain information about the sample's surface topography, composition, etc. The SEM can produce very high-resolution image of a sample surface, revealing details about 1-5 nm in size in its primary detection mode i.e. secondary electron imaging.

Characteristic X-rays are the second most common imaging mode for an SEM.

These characteristic X-rays are used to identify the elemental composition of the sample by a technique known as energy dispersive X-ray (EDX). Back-scattered electrons (BSE) that come from the sample may also be used to form an image.

BSE images are often used in analytical SEM along with the spectra made from the characteristics X-rays as clues to the elemental composition of the sample.

In a typical SEM, the beam passes through pairs of scanning coils or pairs of deflector plates in the electron column to the final lens, which deflect the beam horizontally and vertically so that it scans in a raster fashion over a rectangular area of the sample surface. Electronic devices are used to detect and amplify the signals and display them as an image on a cathode ray tube in which the raster scanning is synchronized with that of the microscope. The image displayed is therefore a distribution map of the intensity of the signal being emitted from the scanned area the specimen.
SEM requires that the specimens should be conductive for the electron beam to scan the surface and that the electrons have a path to ground for conventional imaging. Non-conductive solid specimens are generally coated with a layer of conductive material by low vacuum sputter coating or high vacuum evaporation.
This is done to prevent the accumulation of static electric charge on the specimen during electron irradiation.
The SEM shows very detailed dimensional images at much high magnifications (up to x300000) as compared to light microscope (up to x 10000). But as the images are created without light waves, they are black and white. It is useful for our purposes because the fracture surfaces, nanoparticles and nanocoating can be imaged through SEM with great clarity.

To perform the morphological analysis of the samples we have used a Zeiss, mod. EVO MA10 (Carl Zeiss, Oberkochen, Germany) scanning electron microscopy in collaboration with the $H_2$-laboratory in Pavia (IT). For the instrument calibration it has been used a Co standard.

## 2.6 Hydrogen storage properties characterization techniques

### 2.6.1 Temperature-Programmed Desorption (TPD) analysis

TPD analyses are used to obtain the hydrogen desorption information of as synthesized and cycled materials. In particular in this thesis we have used this technique to investigate the desorption temperature of nanosized magnesium hydride supported on graphene (see chapter 3.5).
TPD analysis was performed by a tandem system consisting of Mettler Toledo Thermogravimetric Analysis (TGA) and Differential Scanning Calorimetry (DSC) system which were coupled to an Omnistar Mass Spectrometry (MS). These instruments were installed inside a glove box filled with high purity Ar (low $O_2$ ppm).
In general, TGA allows for a simple measurement that monitors the weight loss of the material while ramping the temperature up. Besides the weight loss, DSC also monitors the heat flow that corresponds to the inert reference material during the temperature ramps.
In this way, all thermal events of the materials can be observed on the DSC analysis.
These events include the hydrogen desorption process (endothermic) and other structural change events such as melting. The most important part of TPD was the spectroscopic desorption measurement which was performed by the MS instrument connected to the TGA-DSC instrument chamber. During heating, the hydrogen and other volatiles from the materials were released into the

evacuation line which was connected to the MS. They were then analyzed to determine the relative composition of the desorbed gas based on their specific molecular weight.
Using the MS, masses between m/z = 2 to 99 were selectively monitored and measured.
In our case m/z = 2 corresponded to the hydrogen released by the materials.
A typical sample measurement involved a loading of a small amount of samples (4 mg) into an alumina or aluminum crucible to undergo heating on the furnace.
Then, a 10 minute settling time was used to stabilize the initial temperature before the temperature was ramped up to 500 °C. The heating rate was set at 10 °C.min-1 under a flow of 25 ml.min-1 of Ar.
In addition this type of analysis allows also to obtain the hydrogen capacity of the overall materials. It is calculated from two sources; the weight loss captured by the TGA analysis and the calculation based on the hydrogen evolution monitored by the MS.
However, this is only applicable when there are relatively no impurities on the material as observed in the MS. Therefore, it was usually done only with the materials after hydrogen cycling, while the calculation based method was done by integration of $H_2$ peak from MS after a 1 point calibration of the MS with standard $MgH_2$. Standard $MgH_2$ used is commercially available $MgH_2$ (99%, Aldrich) with the calibration results shown in Figure 26.

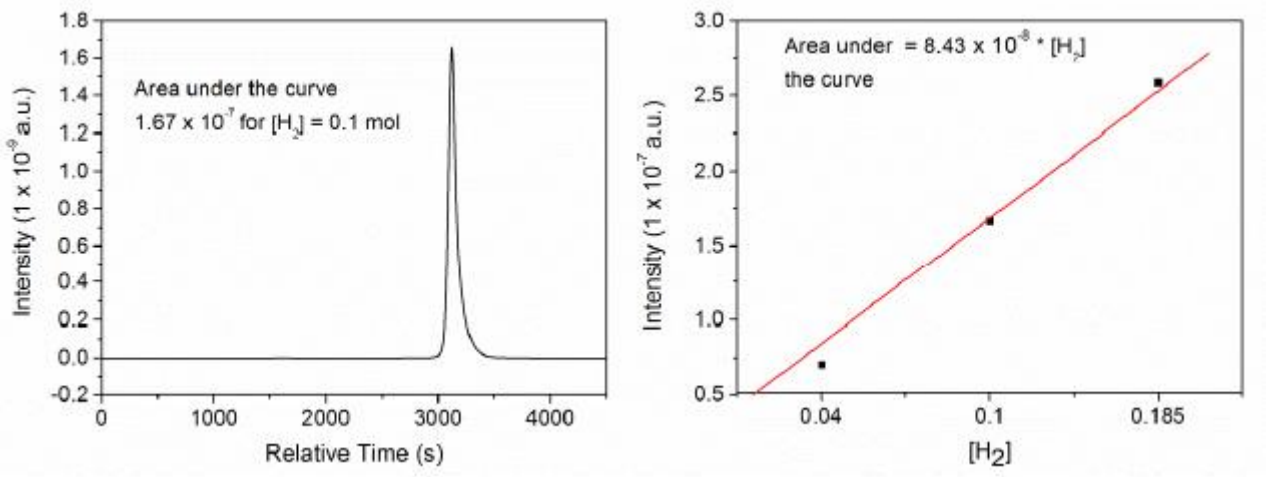


Figure 26: (left) TPD result of a commercialized $MgH_2$ with theoretical $[H_2]$ of 0.1 mol and the area under the curve was used to plot the calibration line (right)

Total Hydrogen storage capacities are typically presented in units of weight percentage (wt%), defined as:

$$wt\% = \frac{mass_{H_2}}{mass_{sample} + mass_{H_2}} x\ 100\%$$

### 2.6.2 Cycling hydrogen pressure measurements in a pressure reactor rig

In the case of investigations of graphene samples, the measurements of hydrogenation/dehydrogenation cycles of the synthesized materials were done in a pressure rig chamber. This instrument was used to anneal and clean the materials from unwanted by-products of the reactions. It was done by manually controlling the hydrogenation/dehydrogenation process where the rig chamber was heated to a certain temperature either under vacuum or $H_2$ pressure.
A schematic drawing of the apparatus is shown in Figure.
It has a thermocouple that is connected to the temperature controller and attached to the outside of the sample chamber to measure the temperature of the sample. The temperature controller regulates the furnace to heat the sample chamber to the set temperature. The pressure in the gas reservoir was monitored using a pressure gauge and was adjusted with manual valves. Typically, a sample was first dehydrogenated under a dynamic vacuum to ensure the removal of by-products for 3-5 h.
Then, the rest of the dehydrogenation steps were performed in a closed static vacuum. The length of the dehydrogenation time was determined from the kinetics measurements of the materials with either a Sievert or Gravimetric instrument.
The sample usually underwent 3 hydrogenation/dehydrogenation cycles before it was characterised further as a cycled material.

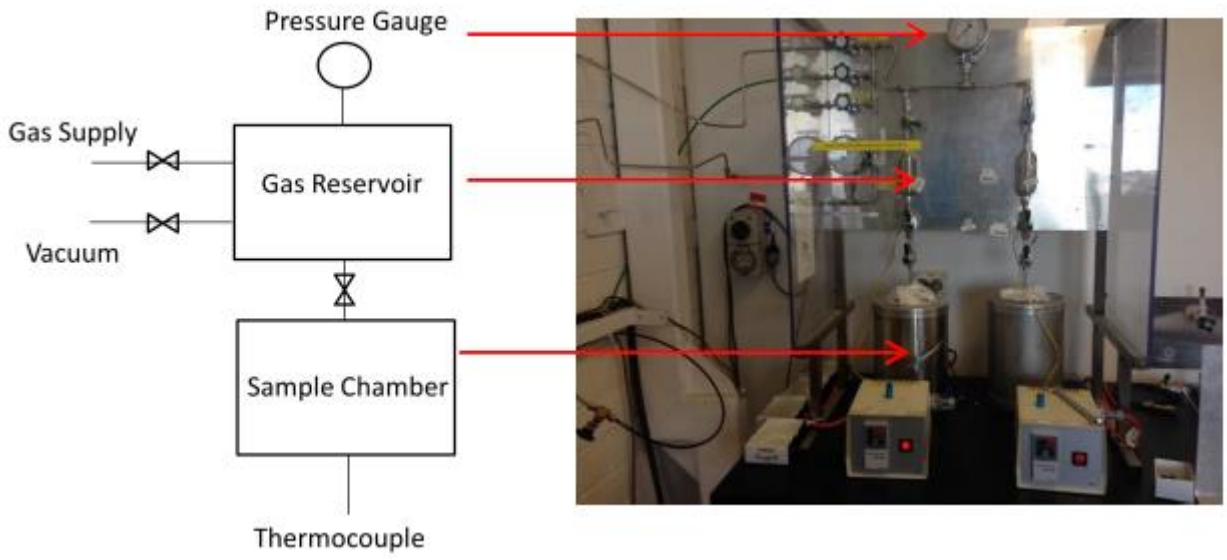


Figure 27:(Left) Schematic diagram of the high pressure manual sorption apparatus for hydrogen storage studies and the corresponding apparatus setup (Right)

### 2.6.3 Absorption and desorption measurements (pcT)

The instrument used to test the sorption properties is a fully automated Sievert type manometer apparatus: PCTPro-2000, Hy-energy & Setaram (Figure 28).
It allows to perform cyclic kinetic and thermodynamic properties measurements of absorption and desorption processes of the investigated samples. In particular it is possible to quantify the absorption and release of hydrogen, by monitoring the pressure inside the system after having measured the volume.

Figure 28: PCTPro-2000 instrument

In this thesis this technique has been used to evaluate the sorption properties of alkali metal intercalated fullerides operating on about 300 mg of as prepared sample.
The absorption measurements consist in monitoring the hydrogen pressure variations as a function of time translated into mass percentage ($H_2$ wt%): in general the system is heated from room temperature up to 280° C at the rate of 5° C/min, under a $H_2$ pressure of 100 bar.
At the end the system is maintained at the end ramp temperature for 10 hours and then it is cooled to room temperature. The absorption results are affected by the instrument sensitivity and present an accuracy of ± 0.1 wt%.
Also the desorption measurements allow to control the hydrogen pressure variations as a function of time translated into $H_2$ wt%: the system is heated from room temperature up to 400° C, at the rate of 5° C/min under a costant $H_2$ pressure of 0.5 bar and then the system is cooled down to room temperature.
In the desorption case we have a results accuracy of ± 0.01 wt%.

### 2.6.4 Combined manometric-calorimetric desorption measurements

We use high pressure cells, with a volume of 10 µl (Fig. 29), combined [9)] with Setaram Sensys HP-DSC instrument connected to the Sievert apparatus(PCTPro). This measures allow to study the hydrogen desorption process from the thermodynamic point of view ($T_{onset}$, $\Delta H_{desorption}$).
About 30 mg of hydrogenated sample are heated from room temperature up to 400° C at the rate of 5° C/min under a $H_2$ pressure of 0.5 bar.

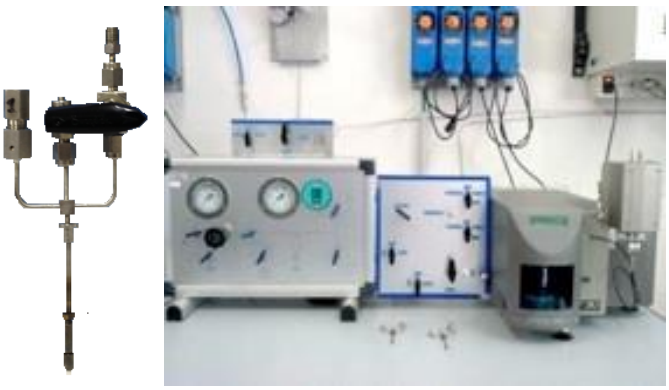

Figure 29: high pressure cell (left); Sensys HP-DSC instrument (right)

## References chapter 2


1) http://serc.carleton.edu/research_education/geochemsheets/techniques/XRD.html

2) Suryanarayana, C.; Norton, M. G., X-ray diffraction: a practical approach. Springer: 1998.

3) ISIS Neutron Training Course, manual

4) https://www.ill.eu/instruments-support/instruments-groups/instruments/in4c/description/instrument-layout/

5) A. Schenck, Muon spin rotation spectroscopy, 1985. [Online]

6) http://www.fis.unipr.it/~derenzi/dispense/pmwiki.php?n=MuSR.MuSR

7) http://nmi3.eu/muon-research/the-musr-technique.html

8) Lowell, S., Characterization of porous solids and powders: surface area, pore size and density. Springer: 2004; Vol. 16.

9) P. Mauron et al., High-pressure and high-temperature differential scanning calorimeter for combined pct measurements of hydrides, *Rev. Sci. Instr*., vol. 80, 095113 (2009)

**Chapter 3**

# Experimental Results and Discussion

The experimental chapter of this thesis starts with the study of fullerene based materials.
In particular we have investigated the storage mechanisms and properties of $Li_{12}C_{60}$ $Li_6C_{60}$ and optimized alkali mixed intercalated fullerides by means of neutron diffraction, MuSR etc...
As it was described in the previous parts of this thesis, our efforts have been focused onto the understanding the interaction occurring between hydrogen and fullerides, the mechanism of $H_2$ absorption with the aim to improve the storage properties of these novel materials with the development of new strategies for the addition of metals to lithium intercalated fullerides.

In the Chapter 1 we have also introduced fulleride systems and we have described the preliminary characterization of this materials.
In particular we have underlined how unfortunately some properties of intercalated fullerides are still detrimental to their application in the field of hydrogen storage.
The high temperatures needed to release $H_2$ from fulleride systems, for instance, suggests difficult operative condition. However, despite the improvements still needed, the relatively high absorption values discovered in both intercalated and hybrid fullerides identifies these systems as very promising.
Therefore it is evident the importance first of all to clarify the hydrogen interactions with carbon to understand the hydrogen behavior in these systems.
Although the study of the starting and the final products are relatively straightforward, the intermediate hydrogenation steps are not yet fully understood.
Muon Spin Relaxation (μSR) has already revealed part of this mechanism on $Li_6C_{60}$ and $Na_{10}C_{60}$, in this chapter we will show, however, that in $Li_{12}C_{60}$ this process looks quite different.
We already know that μSR is a well suited technique to study hydrogen storage materials thanks to the chemical similarity shared by a hydrogen atom and Muonium.
This property makes this technique a unique tool for studying the behaviour of a single hydrogen atom in matter.
The previous μSR experiment on $Li_6C_{60}$ and $Na_{10}C_{60}$ in details has shown a particular behavior:
the zero field measurement has shown quite a large missing fraction which indicates that more than half of the implanted muons undergo an hyperfine interaction with an electron.
In order to understand the origin of this interaction a longitudinal field experiment has been performed, showing that the muon spin polarization is not restored at the field expected for Muonium but at much lower fields, indicating the presence of a radical.
The only possibility for Mu of forming a radical in this system is binding to $C_{60}$ (Figure 30).

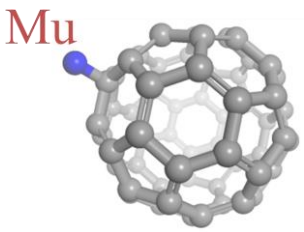


Figure 30: radical Mu-$C_{60}$

So uSR in the case of $Li_6C_{60}$ material shows that the first process to occur while absorbing hydrogen is the hydrogenation of $C_{60}$.
Starting from these preliminary results we have increased the amount of intercalated Li and we have made the same experiment on $Li_{12}C_{60}$.

## 3.1 Study of hydrogen storage mechanism in $Li_{12}C_{60}$

This μSR experiment shows results quite different from the previous case of $Li_6C_{60}$ and $Na_{10}C_{60}$ parent compounds and we have discovered here a new mechanism of hydrogenation.
Moreover, the Li dynamics has been probed by both μSR and Inelastic Neutron Scattering, revealing an internal Li cluster rearrangement, which suggests the activation of Li diffusion above 150 K.
First of all, no missing fraction is observed, i.e. no hyperfine interaction on muon.
The observed relaxation is quite temperature dependent and cannot be fitted with a single combination of relaxation functions.

It is indeed the sum of two contributions: a Gaussian decay and a slow oscillation.

While the former suggests the dipolar interaction with many surrounding nuclei which, in our case, must be $^7$Li; the second, in a non magnetic system, can only originate from a precession into the dipolar field of a single dipolar nucleus, here $^7$Li (the small natural abundance of $^6$Li does not really affect this conclusion), indicating the formation of a bound Mu-Li state.
The first reaction of Mu, in this system, appears the formation of a Mu-Li bound state which could either be the first stage of the formation of the hydride, but could even be part of the spillover process, just after the hydrogen molecule dissociation. The amplitude of this component is strongly temperature dependent and it increases at high temperatures. The remaining fraction represents bare muons stopped interstitially into the alkali cluster.
From the precession frequency we can precisely compute the muon-Li distance which matches that of a Li-H covalent (and not ionic) bond at all the temperatures.
On the other hand, we can compute an average muon-Li distance from the observed decay of the interstitial muons. The big change observed around 250K indicates a structural phase transition implying a cluster rearrangement, also confirmed by inelastic neutron scattering measurements.

In addition, the μSR signal shows a clear transition above 150 K, compatible with a thermally activated Li cluster rearrangement.
Finally a combined Inelastic Neutron Scattering analysis has been performed which shows that tetrahedral Li clusters may undergo a progressive melting upon heating, which could favour room temperature ionic diffusion.
The μSR experiment was carried out on the Argus spectrometer at ISIS-Rutherford Appleton laboratory (Didcot, UK) at the RIKEN-RAL Muon facility. The 100% spin-polarized pulsed beam of this facility is optimized to study the muon spin evolution over long time-scales.
Inelastic Neutron Scattering (INS) measurements have been carried out on the thermal neutrons time-of-flight spectrometer IN4C at the ILL, in Grenoble, France.

**Sample preparation**

The $Li_{12}C_{60}$ crystalline powder has been synthesized as described in the introduction part (pag. 13) by cutting small pieces of lithium (purity of 99 %), mixing them with $C_{60}$ powder (Purity of 99.9 %) in stoichiometric amount and following a solid state synthesis using the ball mill technique.
The obtained powder has been pelletized, it has been introduced in a Ta foil, sealed into a pyrex vial and thermally treated under static vacuum at 270°C for 36h.

To perform the μSR experiment the sample has been pressed and sealed in an air-tight silver-coated aluminium cell, capped by a kapton window. The total experimental muon polarization asymmetry was established to be 21.10(15)%, estimated on a separate transverse field (TF) experiment on pure silver. The baseline, due to muons stopping outside the sample, is measured to be 5.76(11)% of the total polarization. The muon polarization is followed by plotting the asymmetry function, expressed as $A(t) = [N_b(t) - \alpha N_f(t)]/[N_b(t) + \alpha N_f(t)]$, where $N_{b/f}$ is the backward/forward collected counts and $\alpha$ is a geometrical parameter, calibrated for each temperature by fitting the oscillation observed under the application of a 20 G transversal field (TF). Data were analysed by means of the WiMDA software [18], after correcting for the double–pulsed structure of the muon beam.
In the case of INS experiment about 300 mg of $Li_{12}C_{60}$ powder has been sealed in an aluminium flat container sealed with an indium o-ring and measured using neutron incident wavelengths of 1.11 and 2.41 Å. This allowed us to probe the dynamics either in Stokes or in the anti-Stokes side, covering different energy ranges with different resolutions.

**Analysis of the results**

The zero field (ZF) time evolution of the muon polarization of $Li_{12}C_{60}$ has been displayed, for different temperatures, in Figure 31. The initial polarization of $Li_{12}C_{60}$ is 100% of the total asymmetry, while in the previous cases ($Li_6C_{60}$ and $Na_{10}C_{60}$) [14] a sizeable missing fraction was present. In $Li_6C_{60}$ and $Na_{10}C_{60}$, the large fraction of the missing initial polarisation was attributed to the formation of radical species on the negatively charged fullerene molecule.
In that case, the strong hyperfine coupling between the $\mu^+$ and the nearby radical electron generate a muon precession frequency that exceeds the pass band of the instrument, but the application of a longitudinal field (LF) allowed to repolarize this missing fraction and to estimate the value of the muon-electron hyperfine coupling [15].
In $Li_{12}C_{60}$, the absence of missing fraction suggests that no radical is formed on $C_{60}^{6-}$, probably because some more efficient processes prevail in the Mu reaction pathway. Moreover, the ZF relaxation observed in $Li_{12}C_{60}$ is also different from the $Li_6C_{60}$ case, where a simple lorentzian decay was observed and easily ascribed to interstitial $\mu^+$ diffusion.
Due to the low natural abundance of $^{13}C$ (~1%) and to the diamagnetic nature of these material, the only possible spin interaction which the muon experiences is the eteronuclear dipolar coupling with $^7Li$ nuclear spins ($I$ = 3/2; the 7% natural abundance of $^6Li$ gives a negligible contribution).
The complex ZF relaxation observed in $Li_{12}C_{60}$ (shown in Figure 31) can be properly fitted with two different components:

1- a Gaussian decaying component
2- a slowly oscillating component

The former can originate from a multiple dipolar spin interaction.
This would in principle induce a static Kubo-Toyabe (K-T) decay of the muon polarization [25], however, the short time portion of this decay is known to be well approximated by a Gaussian function. The 1/3 recovery expected for the K-T decay would, in our case, fall outside the experimental time window.

The Gaussian decaying part of the polarization can be fitted with the function:

$$P_G(\Delta, t) = A_G exp\left(-\frac{1}{2}\gamma_\mu^2 \Delta^2 t^2\right), \quad (1)$$

where $\gamma_\mu$ is the muon gyromagnetic ratio and $\Delta$ is related to the dipolar interaction through the Hayano function [26]:

$$\Delta^2 = \frac{1}{3} I(I+1)\hbar^2 \gamma_{Li}^2 \frac{8}{3} F \sum_{j=1}^{N} r_j^{-6}\ , \ (2)$$

where $F$ = 1 for integer spins and it is $1 + \frac{3}{8}\frac{I+1/2}{I(I+1)}$ for odd half-integer spins while $r_j$ is the distance between the muon and the $j$-th nucleus [26,27].
Equation 1 describes the time evolution of the spin of those muons stopped interstitially or substitutionally to the alkali ion, thus probing the nuclear dipolar field of the many Li ions constituting the cluster. Incidentally, since $^7Li$ nucleus has a non-zero quadrupolar moment, the spin

Hamiltonian will contain a quadrupolar term in addition to the dipolar one. In case of few $N$ neighbouring nuclei, one have to solve the $2(2I+1)^N$ dimensional problem, while, if $N$ is high enough, as in our case, the K-T or Gaussian relaxations become again a good approximation and the previously adopted approach is fully justified [28].

For the second slowly oscillating component, it was not possible to properly fit by a K-T function (either static or dynamic [25]), especially for the longer time part of the μSR histogram.

On the other hand, a K-T fit of the oscillating part gives a large value for Δ (about 4.5 G, $\gamma_\mu \Delta \sim 0.4\ \mu s^{-1}$) corresponding to an average μ-$^7$Li distance incompatible with the structure of this compound (it would suggest an aggregation of $^7$Li's around the muon, not likely if we take into account the positive charge of both). On the contrary, this part of the spin evolution can be fitted by a decaying oscillatory function.

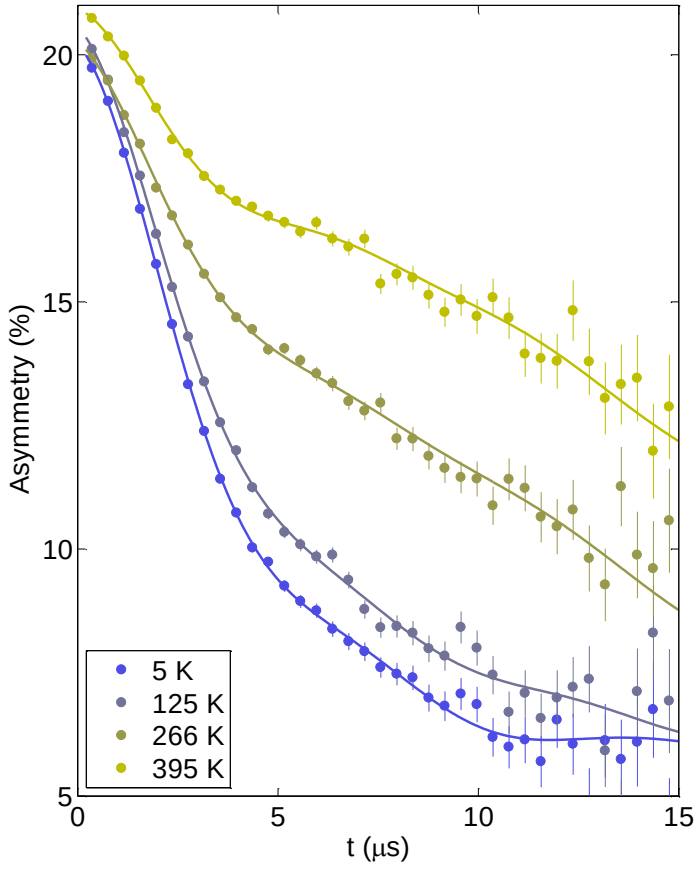


Figure 31: Zero Field μSR asymmetry spectra of $Li_{12}C_{60}$ for selected temperatures. Solid lines represent the fit to equation 3.

Such an oscillation could be originated either by a dipolar interaction between the muon and a single $^7$Li nucleus quite close to it, or by the hyperfine interaction of the muon with a long range ordered magnetic phase (hypothesis already excluded by the diamagnetic nature of the material).

The interaction between the muon and a single lithium spin can be analytically modelled by considering the full Hamiltonian in terms of dipolar and quadrupolar coupling, as described by Meier [29]. The ZF asymmetries were fitted, for different temperatures, according to the function:

$$P_z(t) = P_M(\nu_D, \nu_Q, t)\exp(-\lambda t) + P_G(\Delta, \mathrm{t}). \qquad (3)$$

Here $P_M$ is the Meier function, with $\nu_D$ and $\nu_Q$ respectively the dipolar and quadrupolar frequencies [29]. The observed lorentzian decay of the oscillation is attributed to the $^7$Li diffusional and vibrational dynamics.

The fits with the above-described model are shown in Figure 311 and the results of the fits are displayed in Figure 32. All efforts aimed to adopt different models, for instance by replacing the oscillating term by a static K-T (or Gaussian) relaxation, worsen the fit and leads to non-physical results. In order to explain this result we have to make some considerations. As already observed in the previous study systems $Li_6C_{60}$ and $Na_{10}C_{60}$ [14], the partial electron charge residing on Li clusters can interact with the implanted $\mu^+$ during the muon thermalization process, inducing the production of Mu. Moreover, the high negative charge owned by $C_{60}$ (6 electrons) can easily leads the creation of a $C_{60}$-Mu adduct radical and it is also known to inhibit the formation of endohedral muonium (Mu@$C_{60}$, *e.g.:* a Mu residing at the centre of $C_{60}$) otherwise observed in other fullerides.

However, neither a stable Mu atom nor a radical is formed in $Li_{12}C_{60}$, as no signature for the existence of a muon hyperfine interaction with a paramagnetic electron is observed. This, however, does not exclude that Mu is formed as precursor of an efficient process that can quickly trap it and leave the muon in a diamagnetic environment. Other possibilities are that the muon does not trap any electron (although the slightly positive Li's are not expected to attract a bare $\mu^+$) and sit interstitially or substitutionally to Li. Alternatively, two electrons could bind to the muon forming the muonium ion $Mu^-$ (experimentally observed on LiH [30,31]). Following the latter hypothesis, if we assume the $H^-$ radius and simulate the free volume accessible by it, only two distinct interstitial positions are large enough to accept it: the centre of the big pseudo-octahedral void (which at 20 K resulted unoccupied by Li ions, according to our group recent structural study) [13] or the centre of the $C_{60}$ molecule ($Mu^-$@$C_{60}$), as already observed by MacFarlane *et al.* [32].

For both these configurations, and for other possible locations within the $Li_{12}C_{60}$ structure, we have calculated, from equation 2, the dipolar field ($\Delta$) and we have compared it with the Gaussian width of the fit displayed in Figure 32c. In Table 4, the average radius and calculated $\gamma_\mu\Delta$ are reported for different sterically allowed substitutional or interstitial sites. Since the values reported in Table 4 were calculated for the structure refined at 20 K [13], we have to compare them with the experimental value of $\gamma_\mu\Delta$~0.2 $\mu s^{-1}$ extrapolated at this temperature.

By the comparison of the found values with the experimentally observed ones displayed in Figure32c it is evident that the (a) case ($\mu^+$ in the centre of the tetrahedral cluster) is the one that better reproduces the experimental values.

| Muon site | $\langle R \rangle$ (Å) | *First neighbour Li's* | Calculated $\gamma_\mu \Delta$ ($\mu s^{-1}$) |
|---|---|---|---|
| [a] $\mu^+$@$T_h$-$Li_5$ | 2.7 | 4 | 0.20 |
| [b] $\mu^+$ in $T_h$-$Li_5$ corner | 4.07 | 7 | 0.10 |
| [c] $Mu^-$@$O_h$ void | 3.8 | 8 | 0.14 |
| [d] $Mu^-$@$C_{60}$ | 6.5 | 32 | 0.06 |
| [e] $\mu^+$ in $T_h$ void, $O_h$-$Li_8$ (HT phase) | 3.7 | 4 | 0.07 |
| [f] $Mu^-$ in LiH [31] | 2.04 | 6 | 0.54 |

Table 4: Average distance $\langle R \rangle$ between muon and the first neighbour Li ions for allowed muon sites in $Li_{12}C_{60}$ structure [13], the relative number of first neighbour Li's and the calculated $\gamma_\mu \Delta$ from equation 2. a(b): one $\mu^+$ substitutional to the Li ion at the centre (corner) of the $Li_5$ tetrahedral cluster. A muonium anion sitting at the centre of the cell (c) or endohedral (d). (e): a $\mu^+$ replacing the tetrahedral Li ion in the high temperature phase of Fig.1b. (f): the $Mu^-$ in LiH is also reported for comparison [31].

Following this discussion, below ~150 K the Gaussian relaxation can be attributed to the diamagnetic muons trapped in the centre of the tetrahedron, substitutional to the central Li.
In this thermal range, $\gamma_\mu \Delta$ was calculated to vary between 0.25(2) (at 5 K) and 0.194(1) $\mu s^{-1}$ (at 159 K). In fact, hydrogen is well known to easily cluster with alkali metals, and it is believed to hold a negative charge when added to neutral Li molecules [32].
In our case, it is difficult to assign a net charge on $\mu^+$, since it becomes part of a charged molecule made of five lithium atoms, which should be thought as a whole. We can tentatively attribute a charge of two electrons per cluster ($Li_5^{2+}$), considering they are in number of two per $C_{60}$ and two Li ions are disordered in the crystal. The average Li-H distance is about 1.6 Å for the covalent pair and may vary up to 1.85 Å in small clusters or molecules, while it is fixed to 2.04 Å in bulk lithium hydride salt [31].

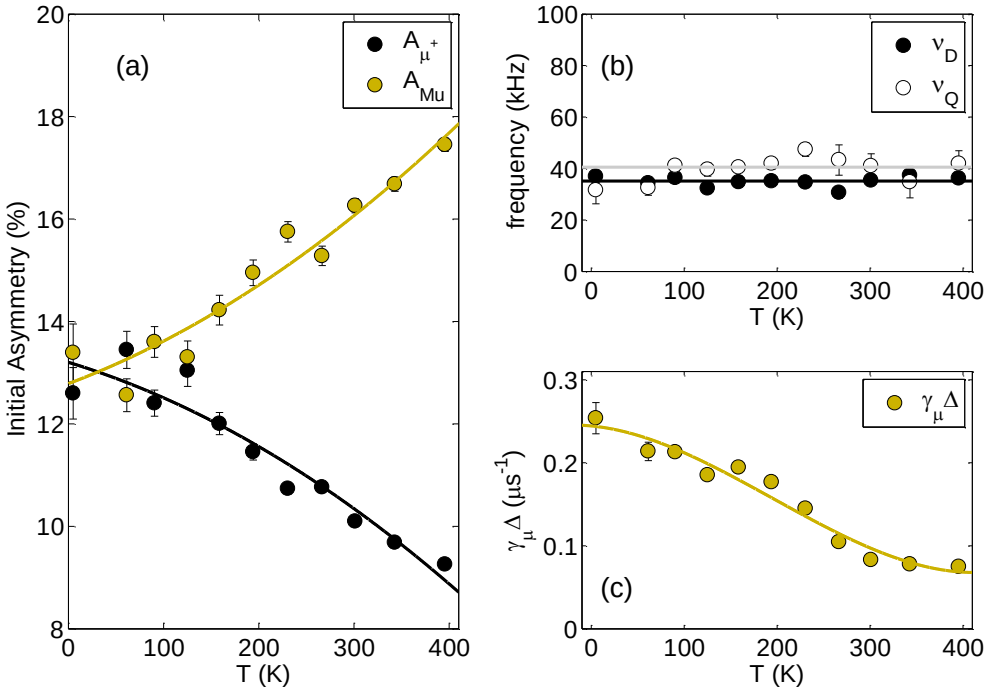


Figure 32: The results of the fit, according to equation 3, for the ZF-μSR data of $Li_{12}C_{60}$ displayed as a function of temperature. (a): amplitudes of the $\mu^+$ (Gaussian) and LiMu (oscillating) components. (b): dipolar and quadrupolar frequencies of the LiMu oscillation (black and grey solid lines represents the respective average value). (c): relaxation rate ($\gamma_\mu\Delta$) of the Gaussian component. Solid lines in (a) and (c) are guides for the eyes.

Upon rising the temperature above 150 K, Δ considerably decreases, indicating a possible phase transition or the migration of the muon to another site, where the average distance between muon and lithium rises. In our opinion, the most plausible possibility is that the Li at the corners of the tetrahedron move far from the central ion toward the $O_h$ void, raising the relative distance, thus forming a cubic cluster ($Li_8^{4+}$) in the larger central void of the cell, as observed by Cristofolini *et al* for $Li_xC_{60}$ compounds (with $x \geq 12$) above 373 K [16].

The high temperature cluster configuration is depicted in Figure 33b.

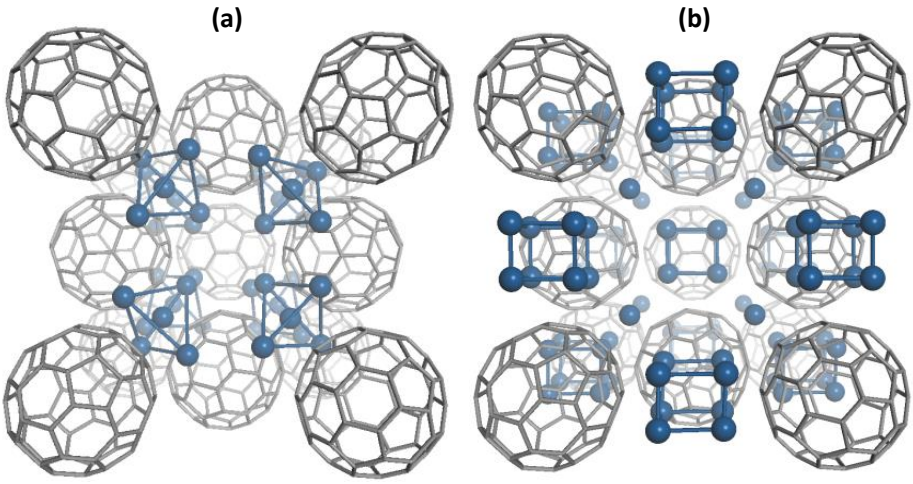


Figure 33: (a) Low temperature phase of $Li_{12}C_{60}$ [13]. (b) High temperature phase as suggested by μSR and INS experiments (as explained in results and discussion paragraph).
The $C_{60}$ in the foreground has been omitted for clarity.

The muon, sitting at the centre of the low temperature tetrahedron, would maintain the same coordination and the dipolar field would decrease as far as the lithia at the corners move toward the centre of the cell. This hypothesis was taken into account by inverting equation 2 for $N = 4$ (the number of lithia at the cluster's corners) and substituting $r_j$ by the average radius $\langle R \rangle$.

The relative $\mu^+$-Li distance is plotted in Figure 31, as a function of temperature, showing a gradual increase from ~2.5 to about 3.7 Å. In this condition, the cubic cluster at high temperature would have an average edge of about 2.6 Å (calculated from the cell at 20 K).

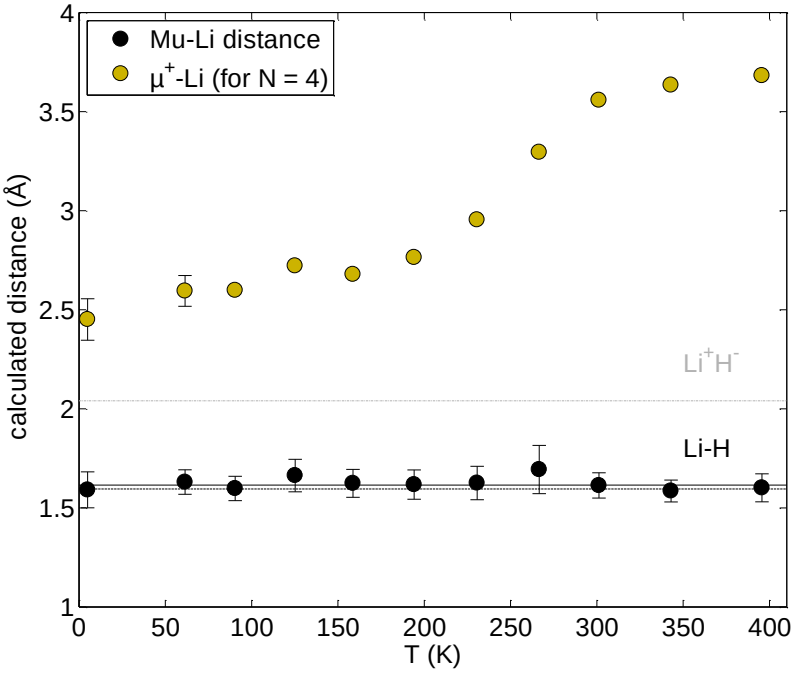


Figure 31: Black dots: distances extracted from the fit to equation 3 for the first LiMu oscillating component as a function of temperature. Dot-dashed lines represent the tabulated distances for the LiH covalent (black) and ionic (grey) bonds. The solid line is the average value of the fit. Yellow dots: Li-$\mu^+$ average distance as computed from Δ for a coordination number of four Li (N=4), reported as a function of temperature.

This hypothesis has been confirmed by Inelastic Neutron Scattering (INS) investigations, which shows an evident temperature evolution of the spectral features associated to lithium cluster vibrations just around 250 K (see Figure 35).

The measurements, performed at different temperatures from 10 to 320 K, have been normalized to the monitor counts, the vanadium standard and then corrected for the background and the scattering coming from the sample holder. The signal was then converted into the so-called generalized density of states $GDOS(\omega,T)$ [20]. The theoretical $G(\omega,T)$ has been calculated by ILL collaborators, experts in DFT analysis, on the basis of first-principles calculations, performed using the projector augmented wave (PAW) formalism [21] of the Kohn-Sham density functional theory, within the generalized gradient approximation (GGA) [19], as implemented in the Vienna ab-initio simulation package (VASP) [23]. All electronic functions have been calculated by them at the gamma point only and an energy cut-off of 450.0 eV was used. Geometry relaxation and a series of single point energy calculations were carried out on $Li_{12}C_{60}$ structural unit as reported in literature [13]. Phonons have been extracted using the direct method as implemented in the Phonon software [23]. $G(\omega,T,Q)$ has been calculated from the partial density of states $g_i(\omega)$ as:

$$G(\omega,T,Q)=\sum_{i=1}^{N}\frac{\sigma_i(coh)+\sigma_i(inc)}{m_i}g_i(\omega)e^{-2W_i(Q)}.$$

Where $\sigma_i(coh)$ and $\sigma_i(inc)$ indicate the coherent and incoherent cross section respectively, $m_i$ is the mass and $W_i(Q)$ is the Debye-Waller factor for the atom $i$. Finally, the summation $G^{th}(\omega,T)=\int G(\omega,T,Q)dQ$ has been carried out on a regular Q-grid, matching the Q-space covered by the experiment.

The calculated spectra, convoluted with the experimental resolution function, were then compared to the experimental data.

In Figure 32, the GDOS of $Li_{12}C_{60}$ derived from IN4c measurements using 1.1 Å wavelength incident neutrons at 10, 200, 250 and 320 K is displayed. As clearly shown, the INS bands located around 15 and 22 meV (indicated by stars) drop as the temperature increases, while the other bands are essentially unaffected. The shaded area below 5 meV indicates the region where a strong contribution from the elastic line is present, hence it was not taken into account in our study.

These data are compared to the Li and C partial GDOS calculated at 10 K. The partial GDOS of Li dominates the total spectrum in the "$C_{60}$ gap" region, i.e. 10-27 meV, where no contribution from C vibrations is expected. In particular, the two peaks at 15 and 22 meV are in good agreement with those found in the experimental data. They were associated to vibrations involving Li atoms located at the corners of the tetrahedral Li cluster, while the central atom (navy area in Figure 35) contributes only weakly in this frequency range. These observations are compatible with a progressive melting of the Li- tetrahedral cluster upon heating. The lack of evolution of the principal $C_{60}$ molecular modes with temperature suggests the absence of severe modification of their local environment.

The amplitude and temperature dependence of the observed μSR Gaussian decay can thus be reasonably explained by assuming that the muon stops inside the tetrahedral Li clusters and probes the $Li_{12}C_{60}$ structural phase transition.

Moving back to the oscillatory muon fraction, as we have explained above, the dipolar interaction of the muon with a single Li ion is responsible for the observed oscillating component.

In analogy of what is observed for H, the muonium could form a $Li^+Mu^-$ ionic pair (similarly to LiH) or a covalently bound Li-Mu molecule [32]. In both cases, the hyperfine coupling would be quenched by a singlet electronic state. In fact, in $Li^+Mu^-$ the 2 electrons on $\mu^+$ would fill the $1s$ hydrogenoid level, while in Mu-Li the electron on $\mu^+$ and the one on Li would lower their energies by forming a bonding molecular orbital. The fit of the ZF polarization to equation 3 leads to $\nu_D$ = 35(2) kHz and $\nu_Q$ = 41(3) kHz (see Figure 32). The dipolar frequency is consistent with the formation of a single Li-Mu covalent bond, being the relative average extrapolated distance 1.62(7) Å and the Li-H covalent bond 1.599 Å [32]. The fit of the data at different temperatures show that the second oscillating component does not show any temperature dependence (see Figure 32b), suggesting the formation of a rather stable species. The lithium intended to form this bond is possibly one of the four at the corners of the $T_h$ cluster or one of the two lithia delocalized in the lattice. Moreover, Figure Figure32a shows a clear temperature evolution of the $\mu^+$ and Mu μSR amplitudes. While at 5 K the two species are present with the same fraction, at 400 K the percentage of muons covalently bound to Li decreases to ~33.5%. This may be compatible with the cluster expansion, also probed by INS, whose increasing sterical hindrance could inhibit the formation of Li-Mu covalent bond.

Furthermore, the quadrupolar frequency is also in good agreement with the DFT calculation made on an isolated covalent Li-H. In this case it results $\nu_Q$ = 46 kHz, for a Li-H molecule with 1.6 Å distance. The slightly lower value extrapolated from the fit could be due to the non-isolated nature of this molecule inside the $Li_{12}C_{60}$ lattice which manifests itself in a different charge on the Li atom. It is also interesting to notice how $\nu_Q$ does not vary significantly on increasing the temperature, indicating that the electric field gradient on lithium, which is affected by its environment, does not undergo major changes during the phase transition, as expected.

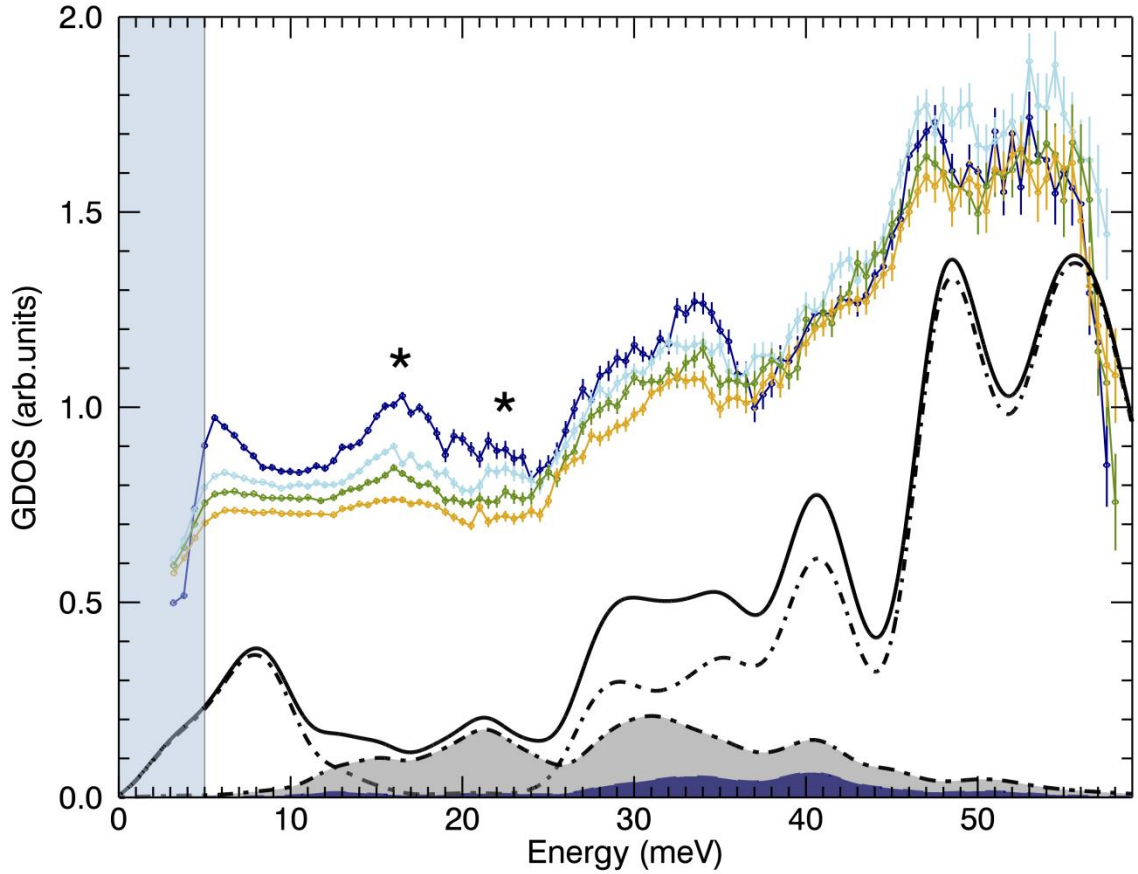


Figure 32: (top curves, from top to bottom, curves are shifted by 0.01 GDOS unit for clarity) Generalized density of states (GDOS) of $Li_{12}C_{60}$ derived from IN4C data using 1.1 Å incident neutrons, as collected at 10, 200, 250 and 320 K. (Bottom curves) Calculated total GDOS of $Li_{12}C_{60}$ (black solid line) and the Carbon (black dot-dashed line) and Lithium (dot-dashed grey area) partial GDOS. The navy area within the grey area represents only the partial GDOS of Li atom at the centre of the tetrahedral cluster. Calculated spectra were convoluted with a Gaussian function having a full width at half maximum matching the energy resolution of the spectrometer.

**Conclusions**

$Li_{12}C_{60}$ system has been studied by means of muon spin relaxation spectroscopy and Inelastic Neutron Scattering and these analysis have unveiled the behaviour of hydrogen in the first step of the hydrogenation process. The results are quite differently between $Li_6C_{60}$ and $Li_{12}C_{60}$.

In the previous study of $Li_6C_{60}$, the formation of a muonic radical is observed, proving that H (Mu) is immediately chemisorbed by $C_{60}$ after the molecule dissociation. In $Li_{12}C_{60}$, H will bind to Li to initiate the formation of LiH (always found in $Li_{12}C_{60}H_y$) [9]. Only after the amount of free Li in the lattice is suitably decreased, the $C_{60}$ hydrogenation is expected to start. As $Li_{12}C_{60}$ is known to chemisorb hydrogen starting at mild conditions (up to 70 °C) [9], we can deduce that the presence of $C_{60}$ dramatically reduces the temperature (and pressure) necessary to combine $H_2$ and Li to form LiH. The two factors enhancing Li hydrogenation are: 1) the formation of small Li clusters, 2) their

partial ionization and further investigations on increasing Li stoichiometry could be useful to understand which is the main factor in the hydrogen absorption mechanism.

After this first analysis focused on the study of the interaction occurring in the first step of hydrogenation for $Li_{12}C_{60}$, we have tried to understand the full mechanism involved in the absorption process in the case of $Li_6C_{60}$ stoichiometry from a structural point of view, using neutron diffraction technique.

### 3.2 Neutron diffraction study of $Li_6C_{60}$ interacting with hydrogen

Although the *in situ* thermal evolution of related fullerides, such as $Na_{10}C_{60}$ and $Li_{12}C_{60}$, has been investigated by means of *in situ* high-resolution neutron powder-diffraction,[8,51] the study of the $Li_6C_{60}$ system has been largely ignored using neutron diffraction or any other detailed structural analysis. Therefore, there is a need to understand the hydrogenation process of $Li_6C_{60}$ from a structural perspective and the combination of deuterium absorption and *in situ* neutron powder diffraction are ideal tools for such analysis.
We have seen that $Li_6C_{60}$ is one of the best performing fullerene-based hydrogen storage material. In the last years this particular fulleride has been widely studied in our group both from the manometric measurements and from structural point of view. We have mentioned in the introductive part of this thesis that a first study of hydrogen behaviour and dynamic has been performed with μSR to analyze the type of interactions occurring during the beginning of the hydrogenation process and has shown how hydrogen binds the carbon of the $C_{60}$ ball forming a C-H bond. It was found an increase in the amount of fraction of muonium adduct radicals cooling down the system to 5K that indicates that hydrogen interaction is enhanced at cryogenic temperatures, while the unfavorable high T needed for hydrogen absorption is probably required to overcome the $H_2$ dissociation barrier mediated by alkali metals. For this reason it is particularly important the optimization of the hydrogen molecule dissociation step to improve the sorption properties of intercalated fullerenes.
Anyway the mechanism of its reversible hydrogen absorption is not, however, totally known and it is important to better understand how these materials work.

In order to understand the mechanism of the absorption process we recently investigated the structural evolution of $Li_6C_{60}$ during the absorption of deuterium with in situ neutron diffraction. The experiment has been performed on the high-intensity neutron powder diffractometer WOMBAT[38] at ANSTO (Sydney, Australia).

The sample was kept under 60 bars pressure of Deuterium and its temperature was gradually increased up to 330 °C while measuring the evolution of its diffraction pattern.
Following the $Li_6C_{60}$ structural patterns evolution is possible to notice several phase transitions that involved the formation and partial segregation of LiH.
Neutron powder-diffraction measurements have been carried out using an incident neutron wavelength of 2.95825(5) Å, determined using the $La^{11}B_6$ NIST standard reference material 660b.
The amount of absorbed deuterium has been determined by the analysis of the variation in the scattered neutron intensity and confirmed by an *ex situ* desorption measurement.

**Sample preparation**

$Li_6C_{60}$ was synthesized from $C_{60}$ powder (purity of 99.99%) by adding stoichiometric amounts of $LiN_3$ in a mortar, pressing the mixture into pellets and annealing them at 350°C for 20 hours. Lithium azide has been previously anhydrified and purified from a 20 wt% solution in $H_2O$ purchased from Aldrich.
The annealing process promotes the Li intercalation into the $C_{60}$ lattice.
In fact LiN3 liquefies at 115 °C and can easily diffuse in the fullerene lattice before its decomposition into metal Li andnitrogen.
The thermal rate to reach the temperature has been divided in 4 sequential steps: up to 120 °C at 60 °C/h, then to 180 °C at 5 °C/h, then to 240 °C at 20 °C/h, and finally to 350 °C at 60 °C/h.
After the synthesis we analyzed the obtained sample by means of X-ray diffraction which confirmed the expected fcc crystal structure of $Li_6C_{60}$.

To perform the experiment $Li_6C_{60}$ was loaded inside a He glove-box into a pressure-rated stainless steel sample cell of ~8 mm inner diameter and 0.51 mm wall thickness equipped with a gas delivery tube and isolation valve. The sample was positioned on the neutron diffractometer inside a vacuum furnace.
The temperature was controlled via a K-type thermocouple at the base of the sample cell, with a second thermocouple attached to the cell just above the sample for monitoring the thermal gradients. The gas line and sample space has been evacuated before the introduction of $D_2$ into the sample and maintained at 60 bar using a Hiden Isochema IMI gas-delivery system.
2 min diffraction patterns were collected continuously throughout the experiment, during which the temperature was increased from 40 to 330 °C in steps of 10–20 °C and held at each step for ~ 20 min. The temperature was then held at 330 °C for about 9 h. The diffraction data were normalized with respect to the incident neutron flux measured by a beam monitor positioned upstream of the sample. An additional set of temperature-dependent data were collected for a nominally-identical sample cell pressurized with 60 bar helium gas. In addition to the intense reflections from the stainless steel cell, some spurious weak peaks were observed, attributed to secondary off-axis scattering from parts of the surrounding sample environment.

It has been possible to estimate the deuterium content of the sample by taking into account both the scattering from the sample cell and sample environment, obtaining the total neutron intensity attributed to the sample alone. The total intensity from the sample for this estimation was obtained by subtracting the total neutron counts of the empty cell, scaled to account for differences in mass in the beam using the first datasets. More in detail, the temperature evolution of the empty cell total intensity was fitted by a polynomial function in order to subtract from the sample-filled cell the value at correct temperature.
After the experiment we have investigated *ex situ* the amount of desorbed hydrogen to confirm the system reversibility and check also the absorbed hydrogen amount. The deuterium desorption was carried out by heating the sample at 5 °C/min from room temperature up to 390 °C under a hydrogen pressure of 0.5 bar in a PCTPro-2000 manometric instrument (HyEnergy-Setaram).

**Analysis of the results**

Neutron diffraction shows how the hydrogen absorption by $Li_6C_{60}$ is a complex process.
From the diffraction pattern analysis we can understand the hydrogen storage mechanism.
The hydrogen molecule is dissociated by the intercalated clusters following a spillover-like process. Then the hydrogen atoms immediately bind to $C_{60}$.This process proceeds up to 8 H atoms attached to fullerene. After that, hydrogen starts to react with Li itself and makes the hydride, which segregates in the lattice.
This leads two detrimental effects: 1) the cluster nuclearity decreases and the cluster ability to dissociate the $H_2$ molecules also decreases; 2) in principle, the production of LiH could segregate an amount of hydrogen which cannot be desorbed anymore.
Fortunately this does not happen. In these particular conditions (LiH nanoparticles decorating the fullerite lattice) the stability of LiH is much lower than the bulk and during the desorption process all the absorbed hydrogen is released and the Li re-intercalates in the fcc lattice at moderate temperatures. The initial compound is then obtained at the end.
All this mechanism involves at least three main processes that will be analyzed in details in the next paragraphs.
The neutron powder-diffraction pattern of the pristine $Li_6C_{60}$ sample and the empty cell diffraction pattern are shown in figure 36.
The complexity of the experiment and reflections from the stainless-steel cell required that Le Bail analyses or single peak fitting routines had to be used to extract information from these data preventing a global Rietveld refinement.
The *fcc* lattice of $C_{60}$ (fulleride) may hold in principle several atoms and if the intercalated ion is sufficiently small (*e.g.* Na or Li),[3–5,12] it is possible to maintain the *fcc* structure by forming small alkali-metal clusters centered in the octahedral or tetrahedral voids of the structure, as happens for $Na_6C_{60}$, $Na_{10}C_{60}$, and $Li_{12}C_{60}$.[3–5,7] $Li_6C_{60}$ is isostructural to $C_{60}$, exhibiting an *fcc* structure at room temperature.

Different from the other systems, it contains a minor fraction of polymeric $Li_4C_{60}$ (below 5%),[12] irrespective of the synthesis procedure. Its structure is similar to the high-temperature monomer phase of $Li_4C_{60}$, which has a Li cluster in the central octahedral void.[12] Le Bail analysis of the neutron diffraction data shown in Figure 1 results in a lattice parameter for the *fcc* phase of $a$ = 13.815(6) Å. This is slightly lower than the value reported in the literature for $Li_6C_{60}$, measured using laboratory X-ray powder diffraction.6 The lattice parameter is also lower than the 14.16 Å of fullerite and this is probably due to the coulombic interaction between Li cations and $C_{60}$ anions, which contracts the overall lattice. The structure appears to be a slightly distorted *fcc* lattice, similar to that observed for $Li_{12}C_{60}$.[13] An amorphous fraction is also commonly present in fullerides, corresponding to by a background below the Bragg peaks.

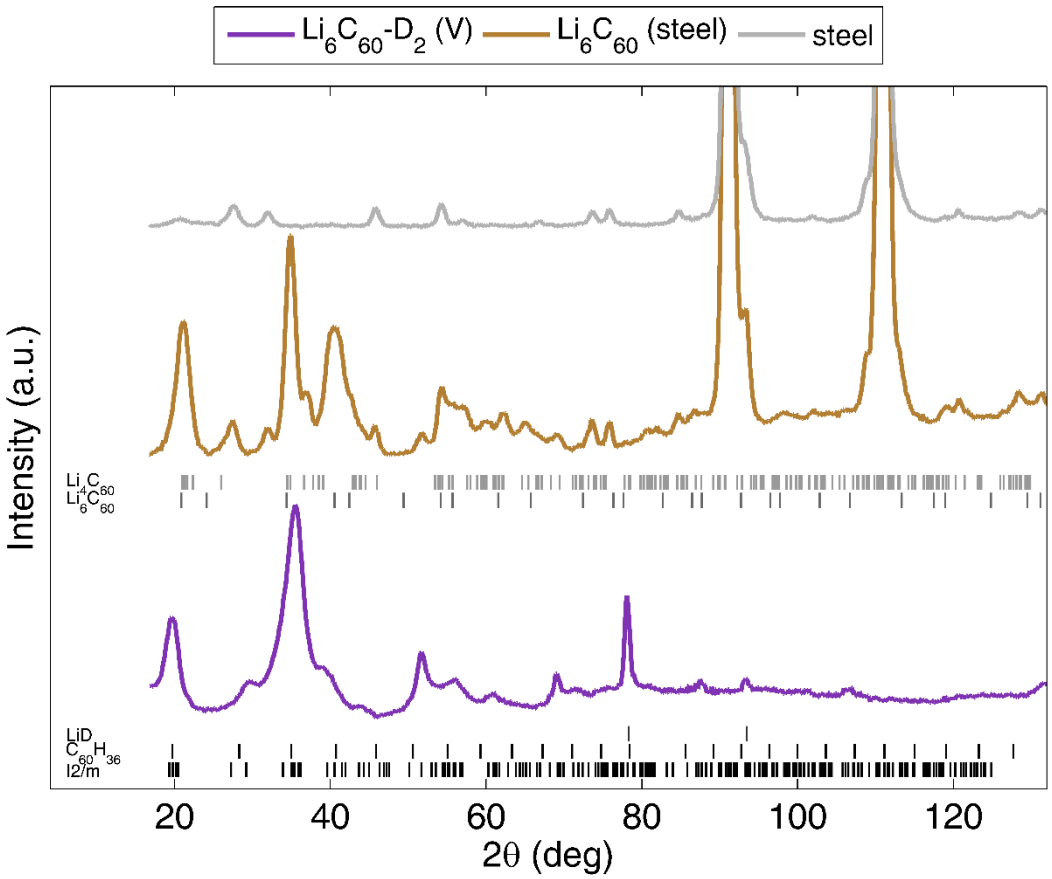


Figure 36: Neutron powder-diffraction patterns of the $Li_6C_{60}$ sample before and after in situ deuteration, as measured at room temperature. Patterns from an empty stainless steel cell and deuterated $Li_6C_{60}$ extracted from the cell and placed in a vanadium can are also shown.
Vertical bars at the bottom are reflection markers for different phases or space groups

The collection of neutron-diffraction data in the relevant scattering angle (2θ) 17–80° for the experiment are shown as a function of deuterium pressure and temperature in a two-dimensional plot in Figure 37. The $Li_6C_{60}$ *fcc* phase in the *in situ* data exhibits its three most intense peaks at scattering angles (2θ) of 21, 35 and 40.5° (the 111, 220, and 311 reflections, respectively).
The $Li_6C_{60}$ *fcc* 111 reflection in particular was targeted to follow the evolution of the *a* lattice parameter as a function of temperature. To read the temperature in the figure, correlated with a specific step, we need to horizontally project the investigated diffractogram point onto

the black line temperature on the left. Single peak fitting using a Gaussian function plus a flat background was performed near the peak and the result is shown in Figure 39.

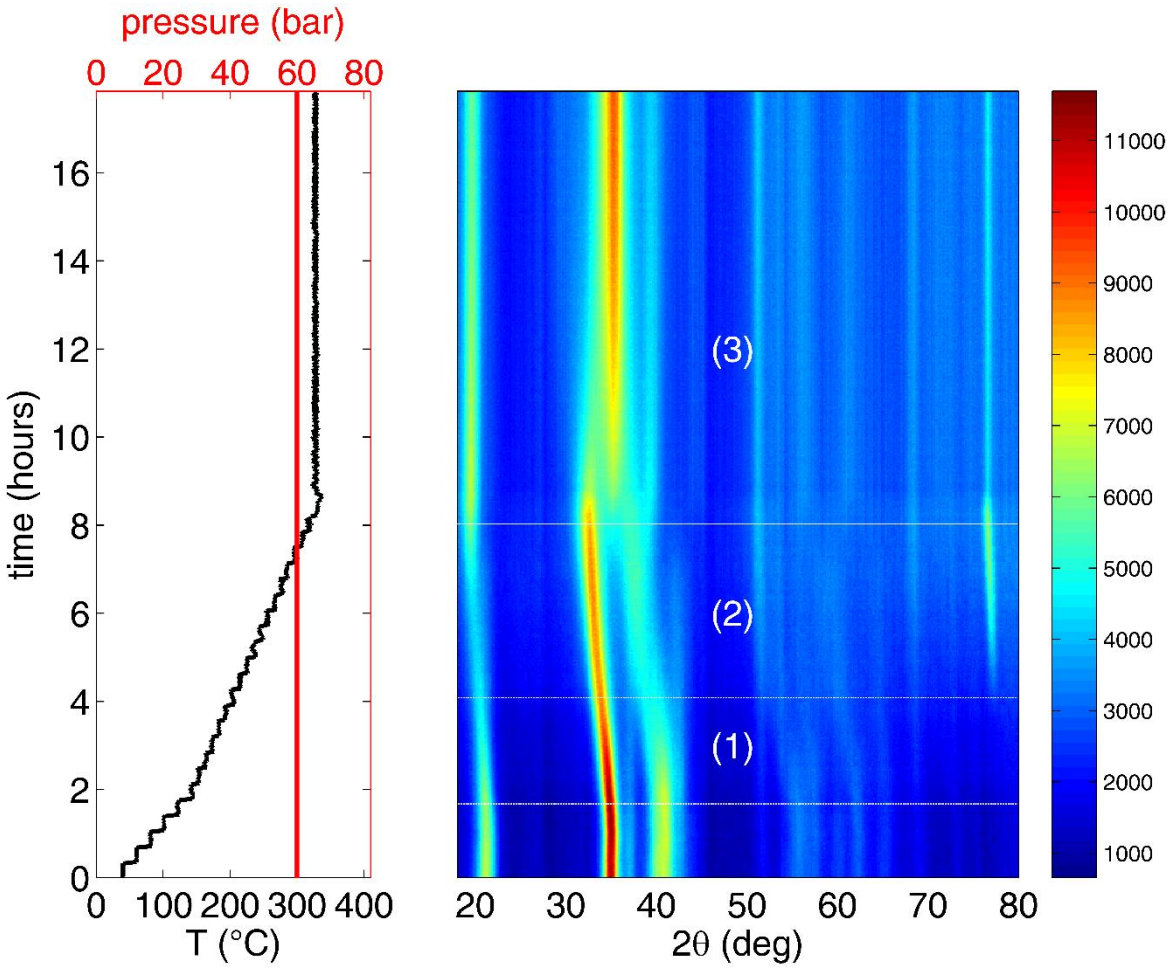


Figure 37: Two-dimensional representation of the time-resolved in situ neutron powder-diffraction patterns of $Li_6C_{60}$ in the region between 18 and 80° (right) and the corresponding temperature and $D_2$ pressure (left). Some weak invariant peaks can be seen that originate from spurious scattering from the sample environment, as shown in Figure . The numbers 1, 2 and 3 label the three main transformations discussed in the text.

Increasing the temperature, above 125 °C the data reveal at least three main processes occurring:

1) Hydrogenation of the $C_{60}$ molecule starting between 130 and 140 °C, when the $Li_6C_{60}$ *fcc* 111 and 220 reflections deviate from their expected thermal evolution and the lattice expands significantly. A similar behavior was observed in $Li_{12}C_{60}$ and $Na_{10}C_{60}$, where an anomalous lattice expansion was detected between 150 and 250 °C, ascribed to the formation of C-D groups on $C_{60}$ which are responsible for the sudden volume increase.[36] During this expansion, the background increases (as expected for the increasing deuterium content, which is a significant incoherent neutron scatterer) and the intensities of the $Li_6C_{60}$ *fcc* 111 and 220 reflections decrease.

This phase transition is a slow process and terminates at about 300 °C, when the lattice expansion rate slows down. It is evident that this first absorption process involves only the $C_{60}$ anions and no

LiD is formed**.** This suggests that the presence of Li in the cell is of fundamental importance in the hydrogen-storage mechanism. Pure $C_{60}$ starts to absorb hydrogen only at ~ 330-350 °C and 200 bar $H_2$ (well above the 140 °C of $Li_6C_{60}$ deuterated at 60 bar) and with very slow kinetics.8
The Li in $Li_6C_{60}$ allows the absorption of $D_2$ (and $H_2$) to occur at much lower temperature. We can simplify this process (1) with the equation:

$$Li_6C_{60} + 4D_2 \xrightarrow{140\ °C} Li_6C_{60}D_8(fcc) \qquad (1)$$

The number of deuterium atoms absorbed by $Li_6C_{60}$ at this stage was approximatively calculated by considering the total neutron intensity at the end of process 1. This deuterium is likely to be chemically bound to fullerene, since the direct hydrogenation of the $C_{60}$ anion, as a first step of hydrogen-absorption process in $Li_6C_{60}$, was already shown to occur by means of muon spin-relaxation spectroscopy [14]. This hydrogen behaviour is not a general rule in fullerides as we have seen in the previous chapter where in the case of $Li_{12}C_{60}$ we have shown that the first hydrogenation step is the formation of Li-D covalent bonds .[36]

2) During the expansion around 200 °C a peak appears at 2θ = 77.3°, assigned to the cubic LiD 111 reflection. The intensity of this peak increases with temperature up to 305 °C. The LiD 220 reflection is also observed when the sample was removed from the stainless steel cell and measured in a vanadium cell (see Figure ).
The second process then begins with the formation of LiD from deuterated $Li_6C_{60}$.
Unfortunately, in this case it is not possible to determine the amount of segregated LiD solely from powder-diffraction data, since the structure factor of hydrofulleride is unknown.
However, a maximum in the normalized total counts is achieved at the end of this stage (corresponding to 1.95 wt% $H_2$). The following equation can describe this process:

$$Li_6C_{60}D_8(fcc) + \frac{y}{2}D_2 \xrightarrow{200\ °C} Li_{6-\alpha}C_{60}D_{8+y-\alpha}(fcc) + \alpha LiD \qquad (2)$$

where $0 < \alpha < 6$ and represents the amount of segregated LiD. If $\alpha = 0$, no LiD is segregated and overall 15 deuterium atoms are bound to $C_{60}$ (as calculated from the normalized total counts). Speculatively, α is likely to be greater than one since by the end of process 3 (see below) the intensity of the LiD 111 reflection has decreased by about 60%, corresponding to a non-integer stoichiometry if $\alpha = 1$. Moreover, the chemisorption of hydrogen by fullerene occurs through the saturation of the carbon $sp^2$ hybrid orbitals and the subsequent formation of C-H bonds. Consequently, only an even number of hydrogens can be bound to $C_{60}$ [44] and α could be 3 or 5, leading to the formation of $Li_3C_{60}D_{12}$ or $Li_1C_{60}D_{10}$, respectively. The reasons for the origin of the formation of LiD are not evident. However, we can consider two different hypotheses.

1) The steric hindrance exerted by 10–12 hydrogens on $C_{60}$ could not allow the stability of more than (6-α) Li ions in the *fcc* cell (*i.e.* the free volume decreases and the Li-cluster is too large to remain in the *fcc* cell). (2) The LUMOs of the $C_{60}D_{8+y-\alpha}$ molecule are able to host a lower number of electrons than $C_{60}$ and the excess Li returns to the metallic state, permitting the formation of LiD.

3) A dramatic structural change is observed above 315 °C and up to the maximum achievable temperature of 330 °C. Here, the integrated intensity of the LiD 111 reflection decreases by about 60% and, at the same time, a new peak at ~35.1° appears. Tentative indexing allowed the latter to be ascribed to the *bcc* hydrofullerene 311 reflection. After reaching the maximum temperature, the $Li_6C_{60}$ *fcc* 220 reflection progressively decreases in intensity and completely disappears after about 4 h at 330 °C. Conversely, the $Li_6C_{60}$ *bcc* 311 reflection increases in intensity and reaches its maximum value after the $Li_6C_{60}$ *fcc* 220 reflection disappears. Despite these changes, the peak at 19.5°, which was previously attributed to the $Li_6C_{60}$ *fcc* 111 reflection, maintains an approximately constant 2θ position during the 330 °C temperature hold. The integrated intensity slightly increases during the first few minutes of the dwell after the phase transition, and then decreases (see Figure 40, region (3)). This is because the $Li_6C_{60}$ *fcc* reflection on the (111) planes and the $Li_6C_{60}$ *bcc* 110 reflection overlap. The fit of this peak is displayed as a function of time and temperature in Figure a and b, respectively. This third process starts at 315 °C and continues for a large part of the 330 °C hold. About 60% of the LiD reacts again and possibly re-intercalates in the form of $Li^+$.
At the same time, a second hydrofulleride phase segregates from the former. About 0.21 wt% of $H_2$ equivalent is released during this process (two D atoms). This deuterium is likely to be released from LiD during the re-intercalation. Moreover, from the variation of the relative integrated intensities of the two deuterated fullerene phases (see

Figure), it is possible to deduce that the transition from the *fcc* to the pseudo-*bcc* structures occurs between two line-phases (*i.e.* the disappearance of the *fcc* phase occurs progressively with the appearance of a new *bcc* structure that is thermodynamically more stable). We can tentatively describe this last stage of absorption by the following equation:

$$Li_{6-\alpha}C_{60}D_{8+y-\alpha}(fcc) + \alpha LiD \overset{315°C}{\longleftrightarrow} Li_{6-\alpha+2}C_{60}D_{8+y-\alpha}(bcc) + (\alpha - 2)LiD \qquad (3)$$

The fact that when the *bcc* phase increases some Li re-intercalates is not unexpected, since a *bcc* arrangement of molecules (rather than a *fcc* lattice) possesses interstitial space for more Li ions.

This third step is the slowest one because, when LiD reacts with the hydrofulleride ($Li_{6-\alpha}C_{60}D_{8+y-\alpha}$), the limiting process is the ionic diffusion of $Li^+$ in the deuterated phase which is reported to be slow.[39]
A similar process is therefore supported here, where the diffusion of $Li^+$ ions from the LiD decomposition into the *bcc* phase (starting at the grain surface) is limited by the slow ionic-

diffusion in this phase. It is also worth noting that after the segregation of Li from hydrofulleride the absorption process by $C_{60}$ stops. This is in agreement with the hypothesis of spillover-like effect of Li clusters in $Li_6C_{60}$:[14] the intercalated Li clusters are effective in dissociating the hydrogen molecules and, when Li is segregated in the form of LiH (or LiD), the chemisorption process by $C_{60}$ is not promoted further.

The three stages described before can be illustrated in the figure below.

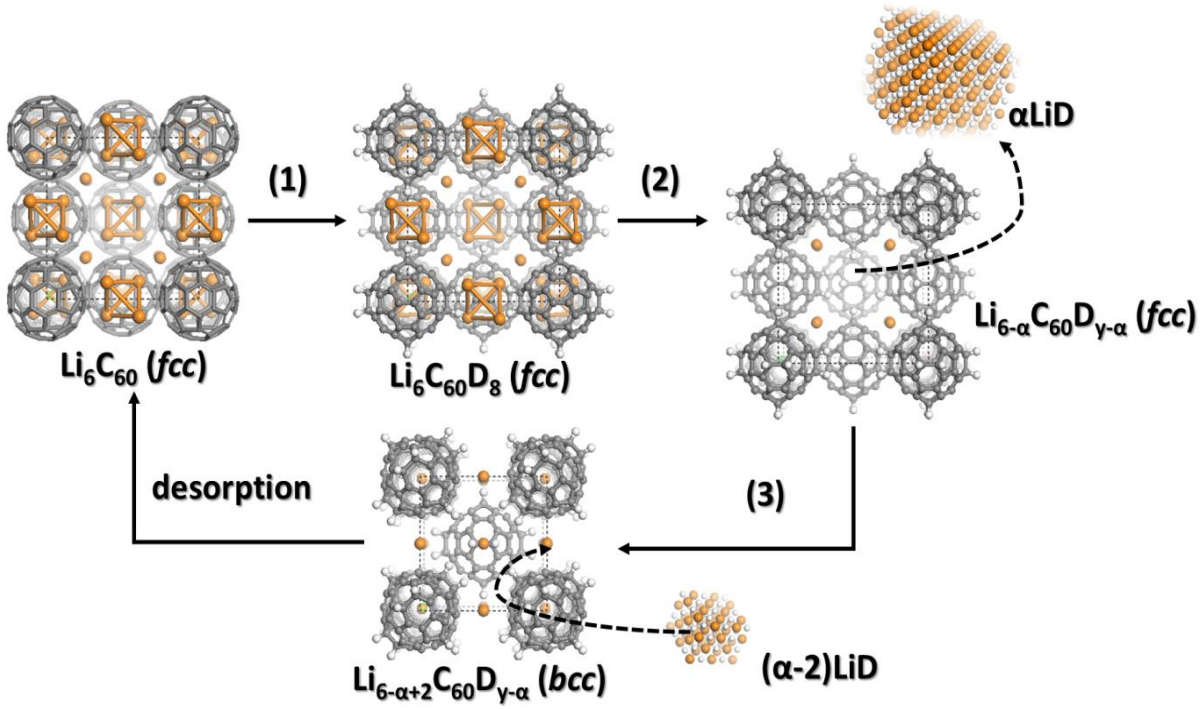


Figure 38: Schematic mechanism of the hydrogenation process of $Li_6C_{60}$

From the analysis in details of the peaks evolution and the structural change, we can see that the *fcc* lattice parameter increases from ~13.8 to 15.0 Å and the lattice then evolves toward the new *bcc* phase, for which the cubic parameter is ~12.23 Å. The sample's normalized total counts increase from 0.75 to 1 (about 33%) during the *in situ* experiment and this can be correlated to the $D_2$ content, which would correspond to 3.93 wt% $D_2$ absorption. An evaluation of the lattice of deuterated compound was carried out by measuring neutron diffraction data of the sample at the end of the experiment in a vanadium cell at room temperature. Le Bail analysis reveals $Im\bar{3}m$ symmetry with a lattice parameter of 11.816(4) Å (close to what is found for $C_{60}H_{36}$).[43]
The lattice parameter value extracted from the Gaussian fitting of the $Li_6C_{60}$ *bcc* 110 reflection ranged from 12.23 to 12.12 Å during the transition at 330 °C in the stainless steel cell (see Figure 3Figure 9c).

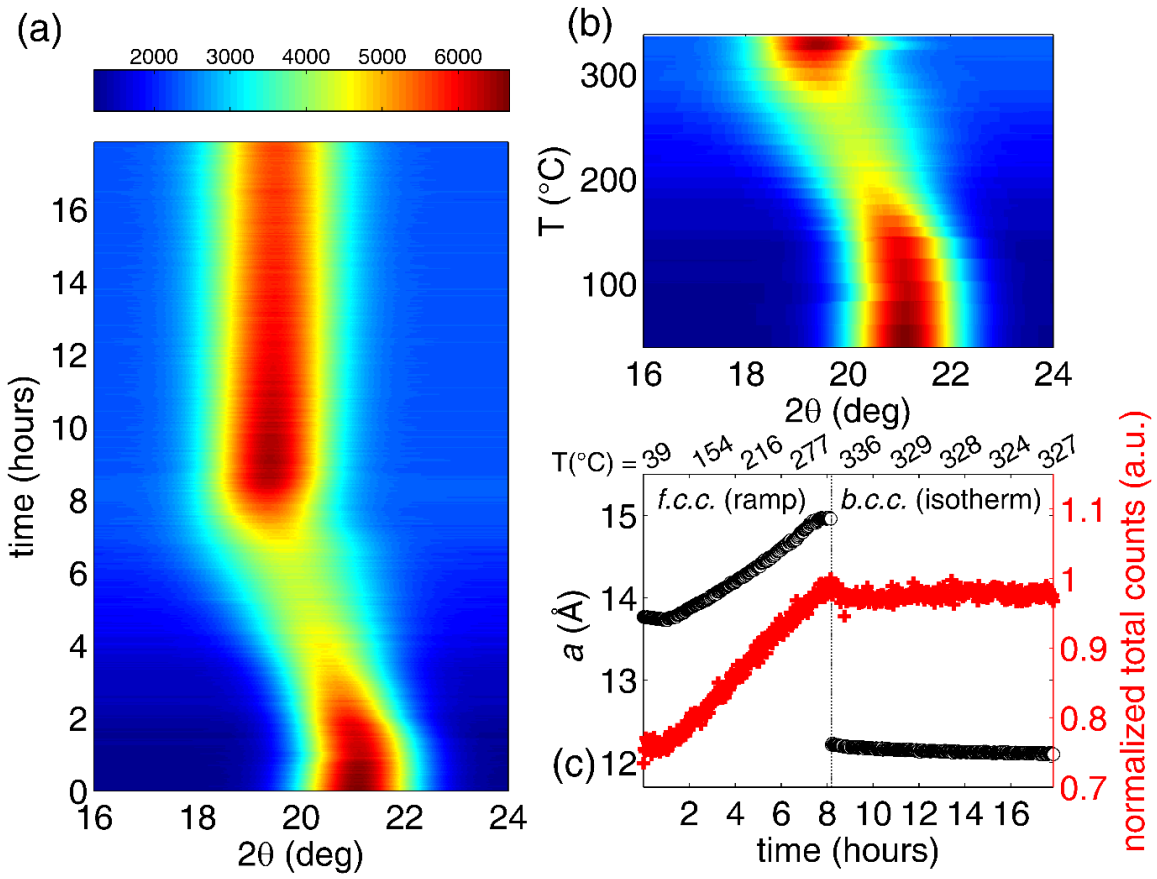


Figure 39: The Gaussian fit of the cubic $Li_6C_{60}$ reflection in the neutron diffraction data as a function of time (a) and temperature (b) during the experiment (only the fit during the ramp is shown in b). (c) The $Li_6C_{60}$ fcc and pseudo-bcc lattice parameter obtained from Gaussian fitting (open circles) and the total neutron intensity (crosses) as a function of time and with discrete temperature points reported.

It is worth noting that the assignment of a *bcc* symmetry to the hydrofulleride $Li_6C_{60}D_y$ lattice should be considered only as an approximation. In fact, while the *bcc* structure indexes well the collected data at low angles, it does not perfectly fit the data at high angles. A more reliable fit was obtained to the data of the sample in the vanadium cell at room temperature with a monoclinic cell with *I*2/*m* symmetry and lattice parameters $a$ = 11.602(3), $b$ = 11.624(2) Å, $c$ = 12.390(1) Å and $\beta$ = 87.43(1)°. Therefore, the lattice can be assumed as pseudo-*bcc* and the *bcc* case discussed approximates reasonably well the monoclinic cell.

The next figure reproduces the evolution of the intensities of the different diffraction reflections.

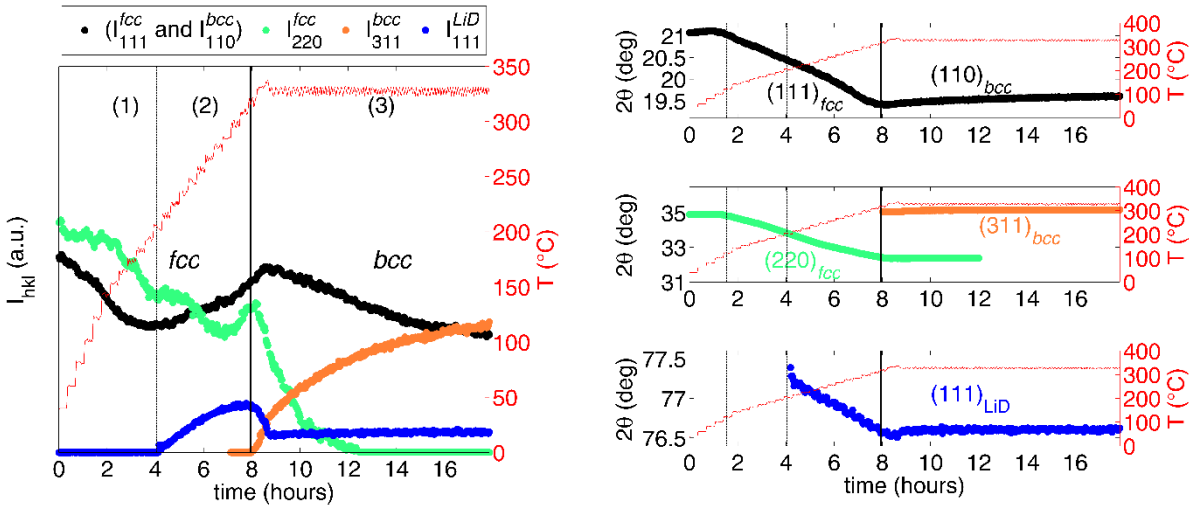


Figure 40: Integrated intensity (left) and 2θ position (right) of selected peaks of the in situ data including reflections from $Li_6C_{60}$ (black, green, and orange), and the LiD 111 reflection (blue). The temperature is shown on the right y-axes. The vertical lines mark the main phase changes. In particular, the thicker black vertical line highlights the point at which the fcc structure starts to evolve toward the bcc phase. The numbers 1, 2 and 3 label the three main transformations discussed in the text.

It should also be noted that the $Li_6C_{60}$ sample did not absorb the maximum amount of deuterium, corresponding to the 5 wt% $H_2$ achieved by treating the sample at 350 °C and 100 bar $H_2$,[1,6] due to the pressure and temperature limits of the sample environment, but on the basis of a preliminary structural analysis of the fully hydrogenated phase, no dramatic changes in the structure are expected during the increase from 2 to 5 wt% hydrogen, apart from an expected small increase in lattice parameter.

At the end of the absorption process in fact (~2 wt% $H_2$ at 300 °C, 60 bar $D_2$) the lattice volume of $Li_6C_{60}$ increases by about 26%. Compared to the volumetric increase per wt% $H_2$ of Mg (~25.5% volume increase in $MgH_2$, corresponding to about 7.7 wt% $H_2$), in these conditions the $Li_6C_{60}$ expansion is about 4 times greater if normalized to the amount of stored hydrogen.

We also know that $Li_6C_{60}$ can easily reversibly accommodate 5.9 wt% $H_2$ by further intercalating a transition metal (i.e: absorption at 350 °C under 100 bar $H_2$ with a Pd catalyst).[34]

From 2 to 5.9 wt% $H_2$ the lattice volume increase is very small (less than 2%) since the space occupied by a semi-hydrogenated fullerene does not differ much from that occupied by a highly hydrogenated $C_{60}$ (such as $C_{60}H_{36}$ or $C_{60}H_{48}$). At its maximum hydrogen content, the volumetric expansion of $Li_6C_{60}$ normalized by the wt% of stored hydrogen is just 1.5 times greater than the same value for Mg. Although molecular systems are commonly-considered less attractive than metal hydrides for applied hydrogen-storage purposes, especially because of their low density, fullerene stands out for its ability to reversibly chemisorb large quantities of hydrogen at mild conditions and with a limited volume expansion.

Deuterium desorption measurement of the sample is been carried out after the *in situ* experiment and is displayed, as a function of time, in Figure 41. The total amount of desorbed deuterium corresponds to 3.4 wt%, equivalent to about 1.7 wt% $H_2$. This is in good agreement with the amount of deuterium calculated from the normalized neutron total counts.

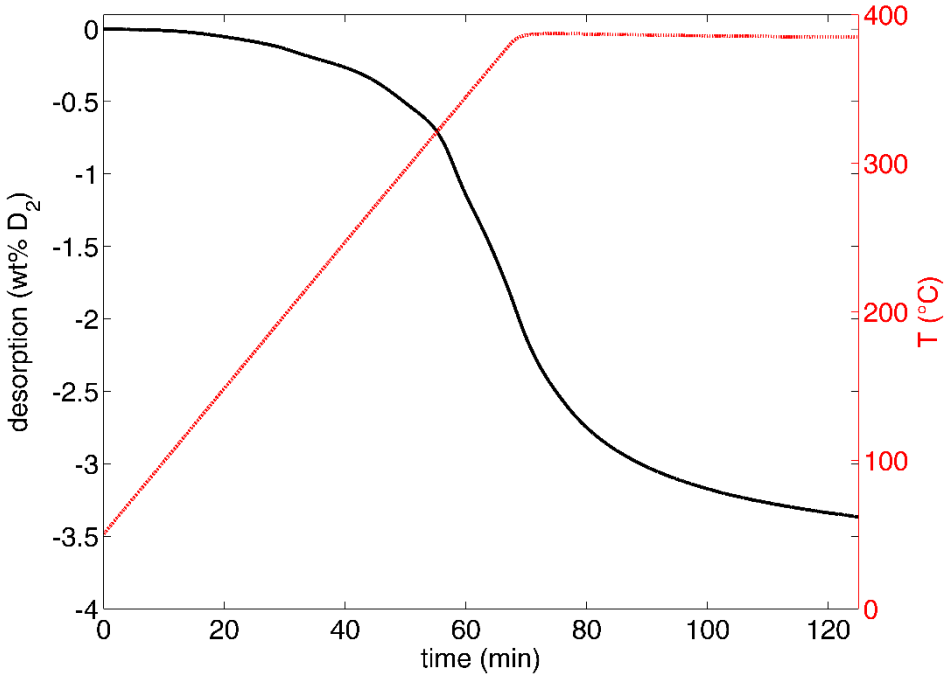


Figure 41: (a) Desorption measurement of deuterated $Li_6C_{60}$ (390 °C, 0.5 bar $H_2$).

**Conclusions**

In this study the deuterium absorption by $Li_6C_{60}$ at 330 °C and 60 bar $D_2$ pressure was investigated using *in situ* neutron powder-diffraction. The sample was kept under 60 bars pressure of Deuterium and its temperature was gradually increased while measuring the evolution of its diffraction pattern. The overall absorption process can be described using three different sub-stages of reaction:

(1) The first deuteration of $Li_6C_{60}$, occurring through an anomalous *fcc* lattice expansion and leading to the formation of $Li_6C_{60}D_8$.

(2) The partial segregation of LiD and the deuteration of fullerene (up to about 2 wt% of equivalent $H_2$ is chemisorbed).

(3) The formation of two line phases and the structural transition to a new *bcc* hydrofulleride structure.

In particular, we found that the low ionic diffusion of lithium (after its partial decomposition from LiD) into the new *bcc* phase is the rate-limiting step in the process.

In conclusion, we have understood and described the mechanism involved in the reaction between hydrogen and $Li_6C_{60}$ underlining the catalytic effect of Li that, together with the charged state of $C_{60}$, constitutes the necessary ingredient for the absorption of hydrogen in this new class of materials, allowing the absorption to take place reversibly at temperatures suitable for on board application.

We have already discussed that, although alkali cluster intercalated fullerides nearly meet the DoE requirements in terms of hydrogen amount, the kinetic of their absorption is still not ideal.

We have also introduced the two different approaches, starting from the $Li_6C_{60}$ fulleride stoichiometry, followed in order to improve the kinetics:

1) Decoration of the lattice with transition metal nanoparticles Pd, Pt and Ni which are known to facilitate the $H_2$ molecule dissociation with increment in the hydrogen chemisorbed amount up to 6 mass%.

2) Cointercalation of both Li and Na in the fullerene lattice.

In these alkali mixed intercalated systems the high occupancy of the $t_{1g}$-LUMO states of $C_{60}$ (usually locating up to 6 electrons) promotes the hydrogen chemisorption through the formation of a C-H $sp^3$ covalent bond [7–10]. Both lithium and sodium intercalated fullerides present advantages and disadvantages: while $Li_6C_{60}$ absorbs high amount of hydrogen, its stability in the hydrogenated phase ($Li_6C_{60}H_y$) is stronger than the hydrogenated $Na_6C_{60}$. This causes the onset of desorption to be higher in temperature with respect to the parent Na intercalated phase [54].
In order to improve not only the absorption kinetics, but also the desorption process, we need to operate on the composition of the fulleride system, in terms of intercalated ions or clusters and charged state of $C_{60}$. So the aim of this work is to find the best compromise between absorption and kinetics of these materials.

### 3.3 $Na_xLi_{6-x}C_{60}$

We have synthesized mixed alkali cluster intercalated fulleride series $Na_xLi_{6-x}C_{60}$ ($0 \leq x \leq 6$)
and we have investigated them by means of charge/discharge kinetic and coupled calorimetric – manometric measurements.
These compounds are isostructural to $Na_6C_{60}$ and $Li_6C_{60}$ while the cubic lattice parameter is linearly dependent on the amount of intercalated sodium (Figure 45).
The $H_2$ absorption/desorption was studied for all the different $Na_xLi_{6-x}C_{60}$ concentrations and we found the best compromise between absorption rate, temperature and amount of hydrogen, in $Na_1Li_5C_{60}$.
This system is able to reversibly absorb up to 4.3 wt% $H_2$ at 280 °C with about 67 % improved kinetics than $Li_6C_{60}$ reference compound.

**Samples preparation**

Materials have been synthesized by following a solid state 2-step procedure in according to the synthetic process showed in the introductive part of this thesis. To obtain the cointercalation we need to produce in a first step the sodium fulleride $Na_xC_{60}$ and then add the lithium to the system.
We usually start from $C_{60}$ (purity of 99.9 %) grinded in an agate mortar with *x* moles of $NaN_3$ (99.99 %, Sigma-Aldrich). $NaN_3$ was previously anhydrified by precipitation from ethanol and then treated in dynamic high vacuum at 150 °C for several hours. The powder is pelletized; the pellets placed in tantalum foil bags and then treated in a Pyrex® vial connected to a turbo-molecular vacuum pump. The materials are then heated in dynamic high vacuum up to 250 °C with a rate of 60 °C/h and then at 450 °C by ramping at 10 °C/h to decompose the sodium precursor
(Tdec $NaN_3$: ~400°C).
At this temperature, the sample is annealed for one day and finally cooled down to room temperature. The as produced $Na_xC_{60}$ has been then analysed by means of X-ray diffraction to check the phase. As we can see in the figure we have obtained highly crystalline fcc compounds in the case of sample stoichiometries x = 1, 2, 3 and 6, while for the samples with compositions x = 4 and 5 they present a monoclinic lattice [51].

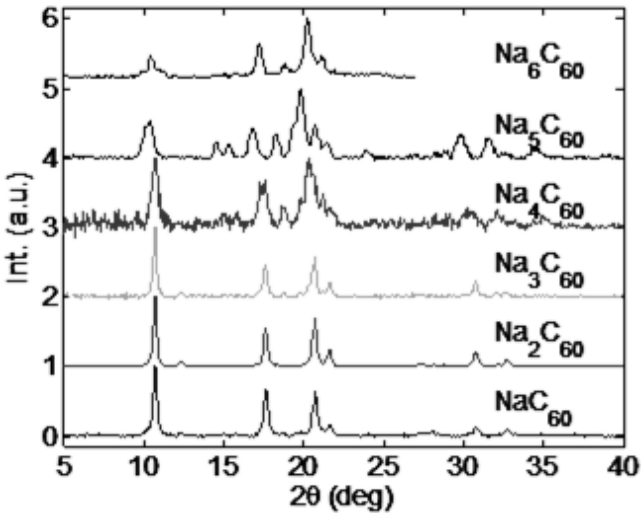


Figure 42:. XRD analysis of $Na_xC_{60}$ at the end of the first synthetic step to check the products formation

In the second step of synthesis, $Na_xC_{60}$ samples is grinded and mixed with (6-*x*) moles of granular lithium ( purity of 99 %), previously cut in very small flakes. The mixture is milled in an agate ball mill (Fritsch Mini-Mill Pulverisette 23, 5 mL volume with 5 agate spheres of 10 mm diameter) at 30 Hz for 60', divided in 6 rounds of 10' followed by 5' of break each.
The obtained black powder was pelletized, placed in tantalum bags, within a sealed Pyrex® vial, and treated at 270 °C for 2 days under static high vacuum conditions.

Figure 43: Ball mill

Another possible synthetic way for this second step uses $LiN_3$ as lithium precursor following a similar approach of the first step. The as synthesized $Na_xC_{60}$ is grinded and mixed in the mortar with (6-*x*) moles of $LiN_3$ and then the mixed reagents are pelletized and treated under dynamic vacuum at 270°C in a vial using the same method described in the production of $Na_xC_{60}$.

We can resume the synthetic steps in the following prospect:

1) Synthesis of sodium fulleride: $x \cdot NaN_3 + C_{60} = Na_xC_{60} + \frac{1}{2}x \cdot N_2$ (dec. 450 °C)

2) Synthesis of $Na_xLi_{6-x}C_{60}$

- First method: $Na_xC_{60} + (6-x) \cdot Li = Na_xLi_{6-x}C_{60}$ (ball-mill + annealing)
- Second method: $Na_xC_{60} + (6-x) \cdot LiN_3 = Na_xLi_{6-x}C_{60} + \frac{1}{2}(6-x) \cdot N_2$ ($T_{dec}$ ~300 °C)

Both the two methods for the intercalation of lithium present particular advantages:
using the Lithium azide allows to obtain samples with a higher crystallinity and a finer powder (figure ) with respect to using metallic lithium. On the other hand using the metal we can better control the stoichiometry of the system because the dynamic vacuum applied during the treatment to decompose the azide can remove also a little fraction of lithium together with the nitrogen.

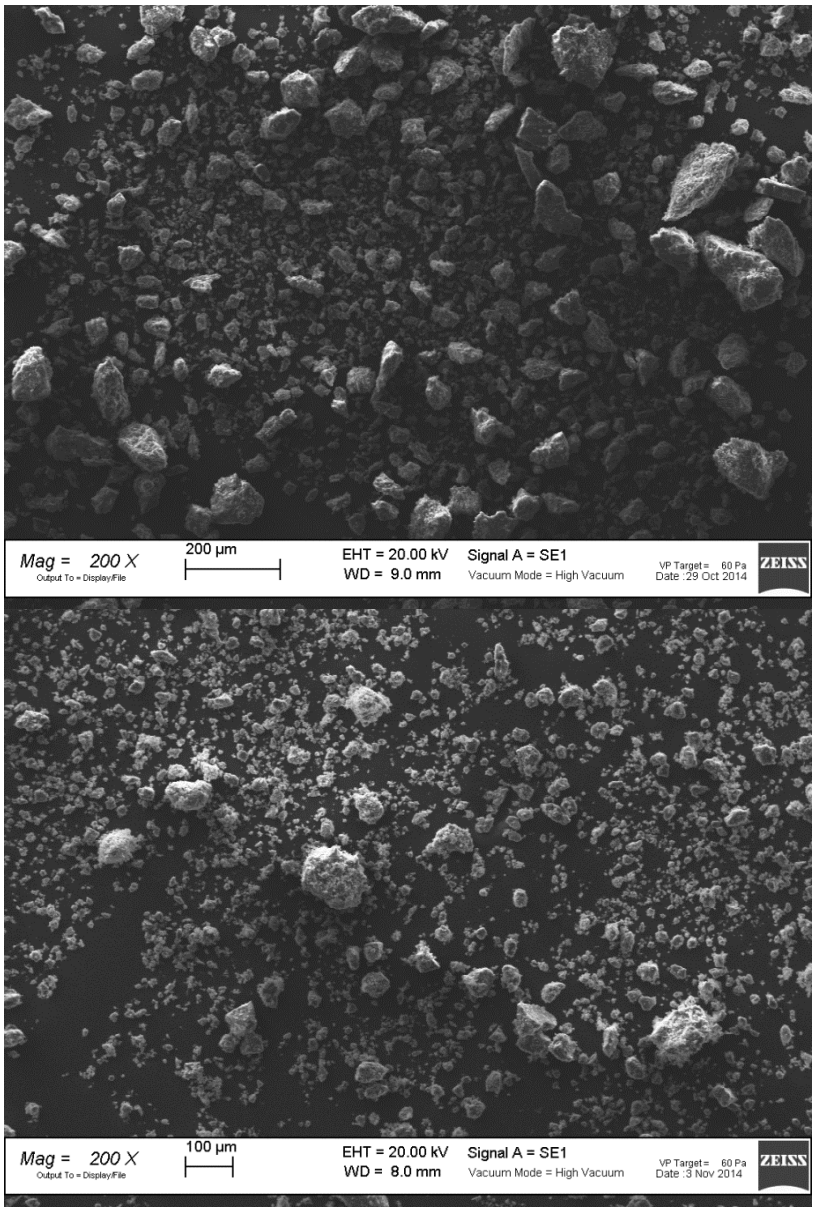


Figure 44: SEM analysis of $Na_1Li_5C_{60}$ obtained by metallic lithium (top) and by lithium azide (bottom)

In this particular study we have chosen to obtain the final product adding lithium metal via ball-mill process in order to better control the stoichiometry of the samples.

After the synthesis the preliminary X-ray powder diffractionhas been carried out by means of a Bruker D8 Discover instrument (Cu-$K_{\alpha 1}$ radiation), working in Debye-Scherrer geometry and equipped with an area detector (GADDS). The samples powder has been sealed in glass capillaries and the measurement have been performed, under spinning condition , collecting data for several hours per frame. Hydrogen absorption investigations have been performed on the as prepared samples in a PCTPro-2000 manometric instrument (Setaram). About 300 mg of sample has been heated from room temperature up to 280 °C at 5 °C/min under 100 bar of hydrogen and a 10 h isotherm was appended at the end of the ramp. Hydrogen desorption kinetic measurements have been performed by heating the sample at 400 °C under 0.5 bar of hydrogen followed by 10 h of

isotherm. All the operations of synthesis and handling of materials were carried out in air and moisture free conditions by operating in vacuum or within an Ar glove box ($O_2$ and $H_2O$ levels <1 ppm).

**Analysis of the results**

The synthesis of $Na_xC_{60}$ phases by means of the azide method produces well-crystallized samples, as shown in powder X-ray diffractions of Fig 45 .
The Le Bail analysis of those spectra confirmed the formation of the well-known *fcc* phases of $Na_2C_{60}$ (for x = 1, 2, and 3) and $Na_6C_{60}$ (for x = 6),[11] and the monoclinic phase of $Na_4C_{60}$ (x = 4 and 5).[51] The $Na_xLi_{6-x}C_{60}$ phases exhibit broadened peaks (see Figure 45). These are in part due to the reduced size of powder grains and the increased disorder caused by the high-energy ball milling.
On the other hand, a decrease of the *fcc* symmetry, inducing a pseudo-*fcc* arrangement of fullerenes, is commonly observed in Li containing fullerides, leading to *fcc* peaks splitting.
In case of low resolution (such as for X-ray powder diffraction) the convolution of these peaks can be confused as peak broadening. The refinement of the pseudocubic lattice parameter by Le Bail analysis of the diffractograms, adopting the $Fm\bar{3}m$ cell of $C_{60}$, demonstrated an increasing trend, according to the relative increase of *x*. For *x* = 6, we found *a* = 14.37 Å, in good agreement with the literature.[11] Satellite peaks near the 111 reflection, at ~10.5°, and the peak at 18-20°, between the 220 and the 311 reflections, are normally attributed to hexagonal distortion of the *fcc* lattice, as stacking fault type of defects [18]. Due to the *fcc* (or pseudo-*fcc*) arrangements of $C_{60}$ molecules, the only way to fill the free space with 6 atoms of Na (Li) is allowing the formation of an alkaline cluster in the central octahedral void of the cell. This cluster is tetrahedral in case of $Na_6C_{60}$ [11] and not yet characterized in the novel $Na_xLi_{6-x}C_{60}$ phases.

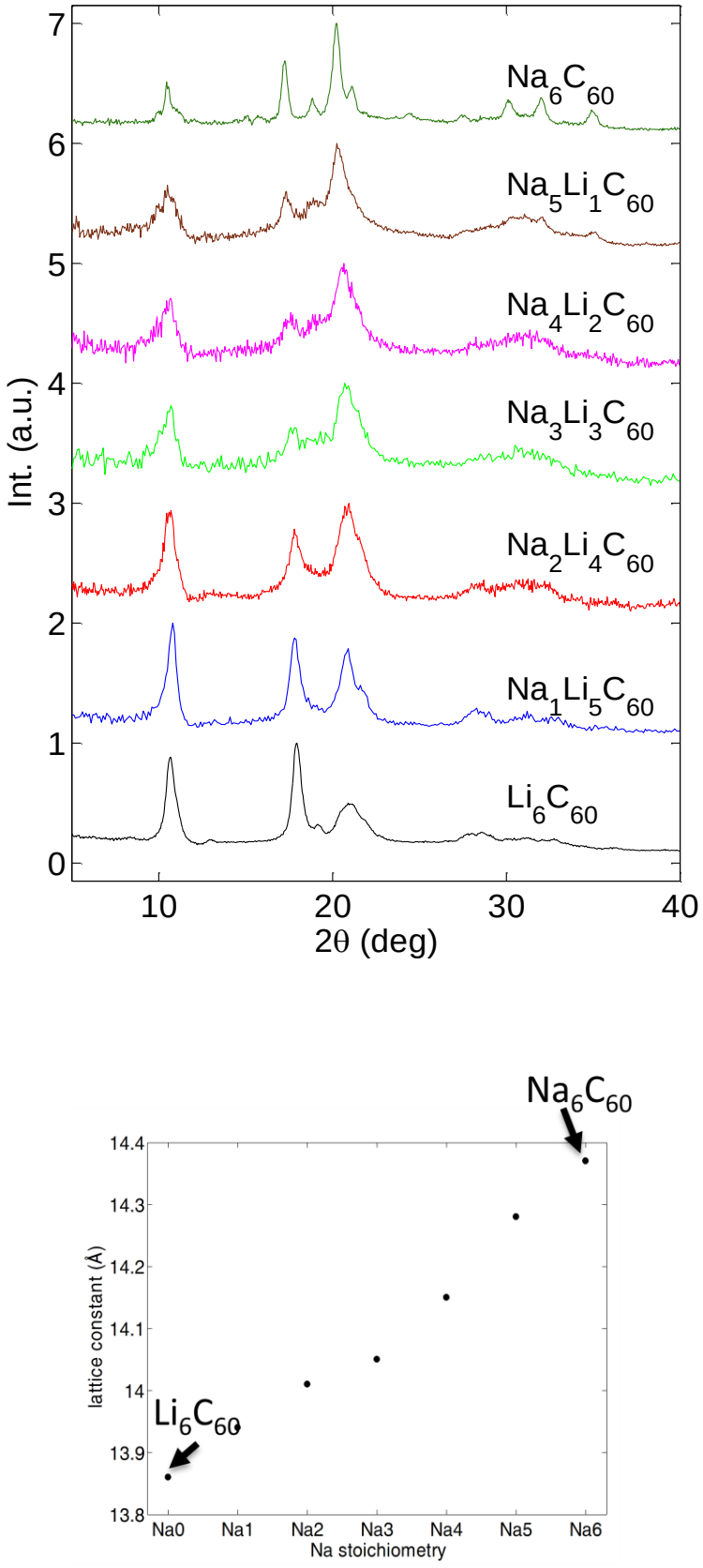


Figure 45: On the top: X-ray powder diffractions of $Na_xLi_{6-x}C_{60}$. At the bottom: fcc lattice parameter as a function of Na content from 0 to 6, as obtained from Le Bail analysis of the diffraction patterns.

The samples have been hydrogenated at 280 °C under 100 bar $H_2$.

The first hydrogen absorption and desorption cycle is reported, as a function of time, in Figure 47.

Hydrogen absorption – desorption cycles showed that both the gravimetric capacity and the absorption rate significantly improve by decreasing the Na content and the values obtained for the mixed compound $Na_1Li_5C_{60}$ are better than those for pure $Li_6C_{60}$( Table ), testifying the catalytic activity of Na when added in small amount to the Li-fullerite. The hydrogen sorption reaction is reversible for all the stoichiometries, the cycling ability is good in the frame of 3 cycles (maximum tested up to now) and as we have already discussed in the previous chapters, the addition of Na destabilises the hydrogen sorption process, and we obtain a promotion in the dissociation of hydrofullerene with desorption temperature below 300 °C.[8,9]

By checking with X ray diffraction after the hydrogenation at 280 °C ( Figure 46 ) is possible to see an expansion of the *fcc* cell caused by the $C_{60}$ volume increasing due to C-H bonds formation.
In case of $Li_6C_{60}$ and $Na_6C_{60}$ the lattice is evolved from *fcc* to *bcc* when hydrogenated above 300°C, in this case we don't notice any evolution of the *fcc* structure.

We observe also the formation of LiH and NaH, although is not possible to make a quantitative estimation from XRD data. In the analysis we have chosen the stoichiometries with x = 2 and 3 as general references for all the $Na_xLi_{6-x}C_{60}$ fullerides.

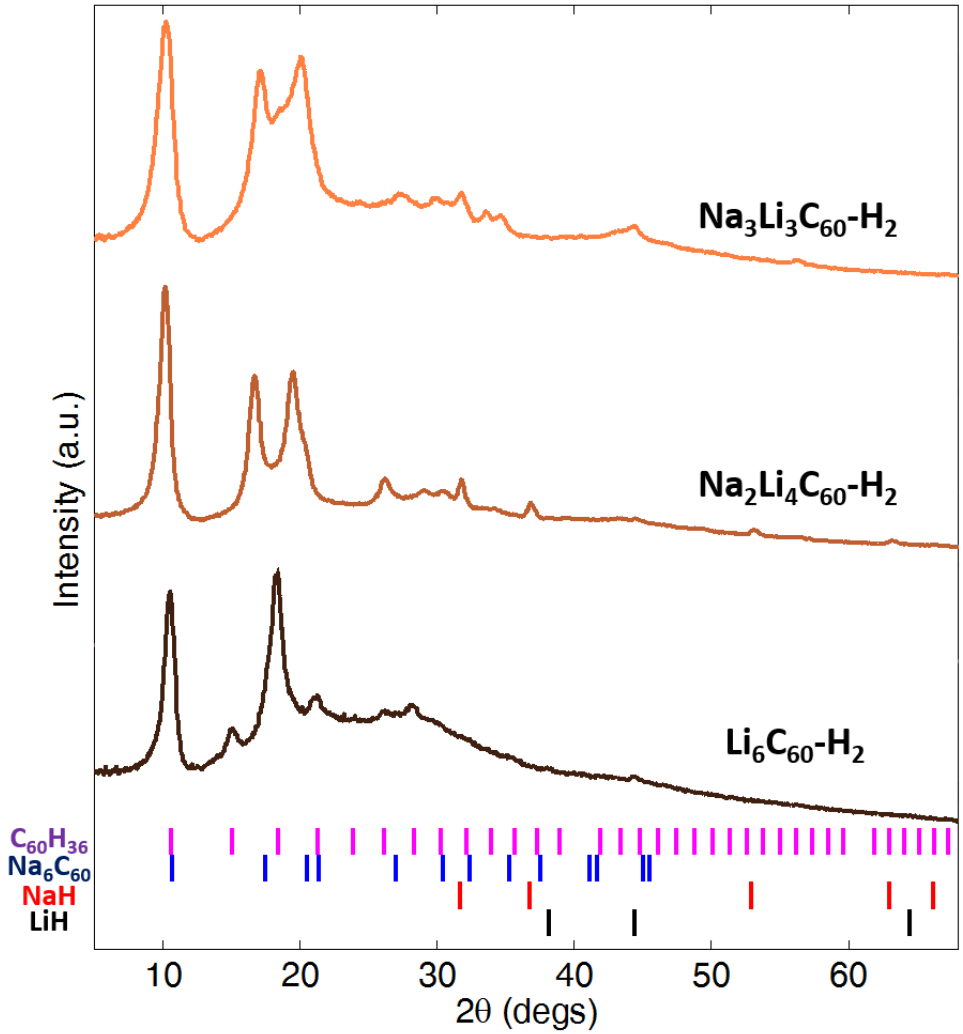


Figure 46. X-ray powder diffraction patterns of selected $Na_xLi_{6-x}C_{60}$ after the first hydrogen absorption at 280 °C (100 bar). The pattern of $Li_6C_{60}$ hydrogenated at 350 °C (100 bar) is also reported for comparison. The general data of the most important results on the hydrogen storage parameters of all the $Na_xLi_{6-x}C_{60}$ samples are reported in the table.

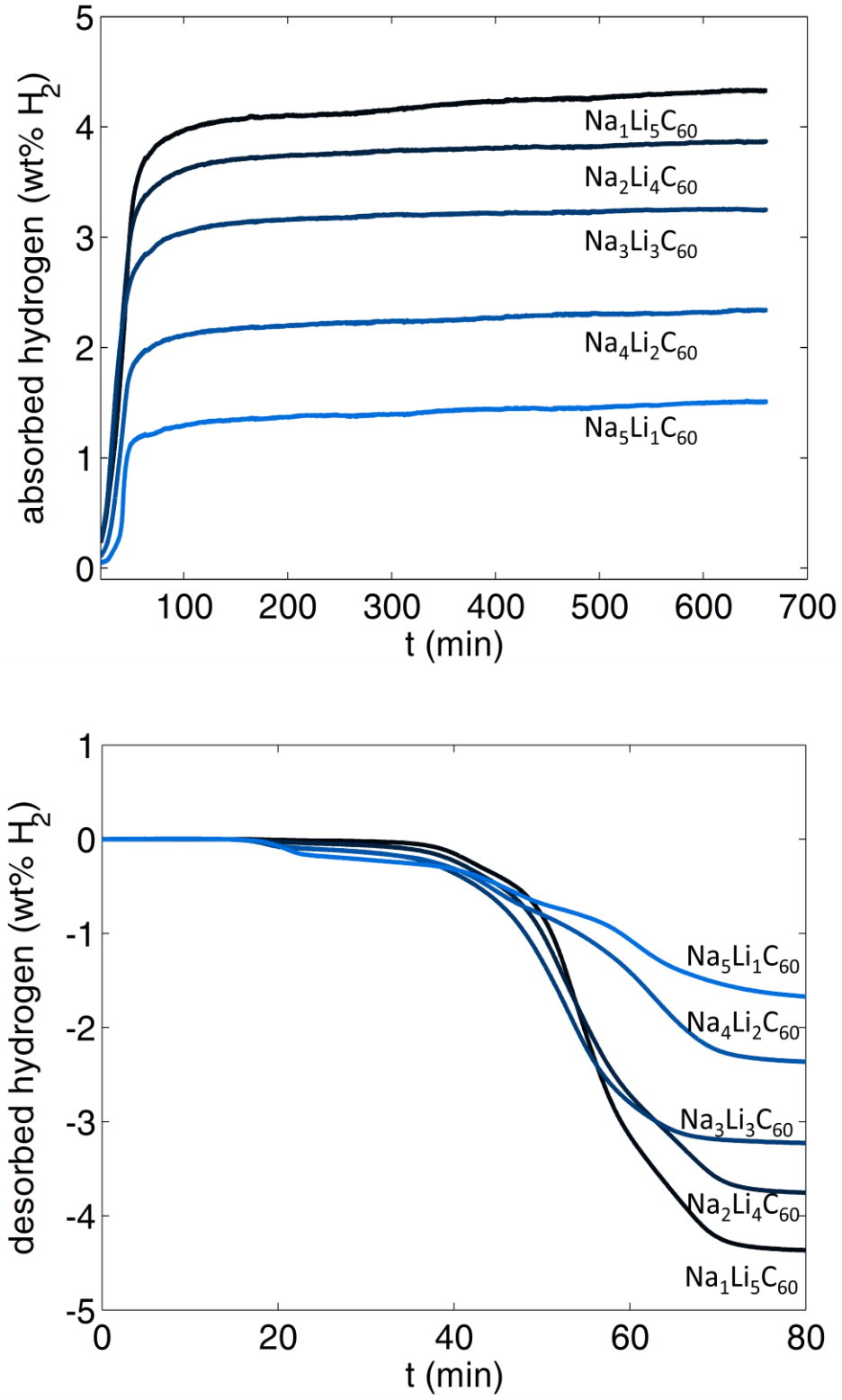


Figure 47. 1st cycle of hydrogen absorption (up) and desorption (bottom) of $Na_xLi_{6-x}C_{60}$ are reported as a function of time and amount of hydrogen absorbed and released.

| Sample | Absorption capacity (wt %) @ 280 °C | Gravimetric capacity (wt %) after isotherm | Absorption rate (x $10^{-2}$ wt %/min) under the ramp |
|---|---|---|---|
| $Li_6C_{60}$ | 1.8 | 3.5 | 3.9 |
| $Na_1Li_5C_{60}$ | 3.2 | 4.3 | 6.5 |
| $Na_2Li_4C_{60}$ | 3.1 | 3.9 | 5.9 |
| $Na_3Li_3C_{60}$ | 2.8 | 3.2 | 5.0 |
| $Na_4Li_2C_{60}$ | 1.5 | 2.4 | 3.3 |
| $Na_5LiC_{60}$ | 1.8 | 2.3 | 3.5 |
| $Na_6C_{60}$ | 1.5 | 1.8 | / |

Table 5: kinetic absorption properties (Absorbed $H_2$, onset temperature and rate) of the $Na_xLi_{6-x}C_{60}$ phases.

The analysis of the time derivative of desorption curves allow to better separate the different processes involved when varying the stoichiometry. In Figure 48 the rates of desorption are reported as a function of the time and the profile of desorption has been tentatively fitted by different non-correlated Gaussians. It is possible to identify at least four main processes. One occurring at lowest temperature (near 150 °C) and at least three convoluted processes above 200 °C. The results of the fit are shown in Figure 48: it is evident that the first peak of desorption, between 140 - 155 °C, is highly dependent on Na presence, being absent in $Li_6C_{60}$ and progressively more consistent between x = 2 and 6. It is worth to point out that the percentage of desorbed hydrogen is not only dependent on the amount of hydrogen but also on the density of the absorber. Therefore, an increasing (decreasing) of the wt% of $H_2$ when varying the amount of Na in the structure, does not necessary corresponds to the same variation in the stoichiometric content of hydrogen. For instance, assuming that the only product of hydrogenation is $Na_xLi_{6-x}C_{60}H_y$, a 1 wt% $H_2$ in $Na_1Li_5C_{60}$ and $Na_6C_{60}$ corresponds to a different value of y = 7.8 and 8.6 respectively. The amount of hydrogen released in the first process is very low and varies between 0.02 (for x = 1) and 0.2 wt% $H_2$ (in $Na_6C_{60}$), corresponding to about 0-2 hydrogen atoms per $C_{60}$, while the minimum temperature for this step is found for *x*=3 (140 °C). The second process is clearly lower in temperature for Na containing samples (247 °C for *x*=2) than for $Li_6C_{60}$ (291 °C) and the amount of desorbed hydrogen varies from 0.3 ($Li_6C_{60}$) to 0.95 wt% (*x*=4), corresponding to 2-8 hydrogens per $C_{60}$, depending on

*x*. The third process, occurring between 308 and 347 °C, is the most important and dependent on *x*. In the case of $Li_6C_{60}$ it occurs at 323 °C and only 0.3 wt% $H_2$ is released (about 2 hydrogens per $C_{60}$). In the mixed phases, the maximum desorption is reached for x = 0.5 at 330 °C, corresponding to 3.3 wt% $H_2$ (about 26 hydrogens per $C_{60}$) and decreases progressively with *x*. The last process is the highest in temperature; it decreases in temperature with *x* varying from 380 °C ($Li_6C_{60}$) to 350 °C (*x*=0.5) and for some sample is completed during the isotherm. In the case of $Li_6C_{60}$ this is the most important process, corresponding to 2 wt% $H_2$ desorbed (about 15 hydrogens).

Anyway, for $x \neq 0$, the amount of desorbed hydrogens ranges from 8 to 12 (depending on *x*), corresponding to about 0.3-1.2 wt% $H_2$.

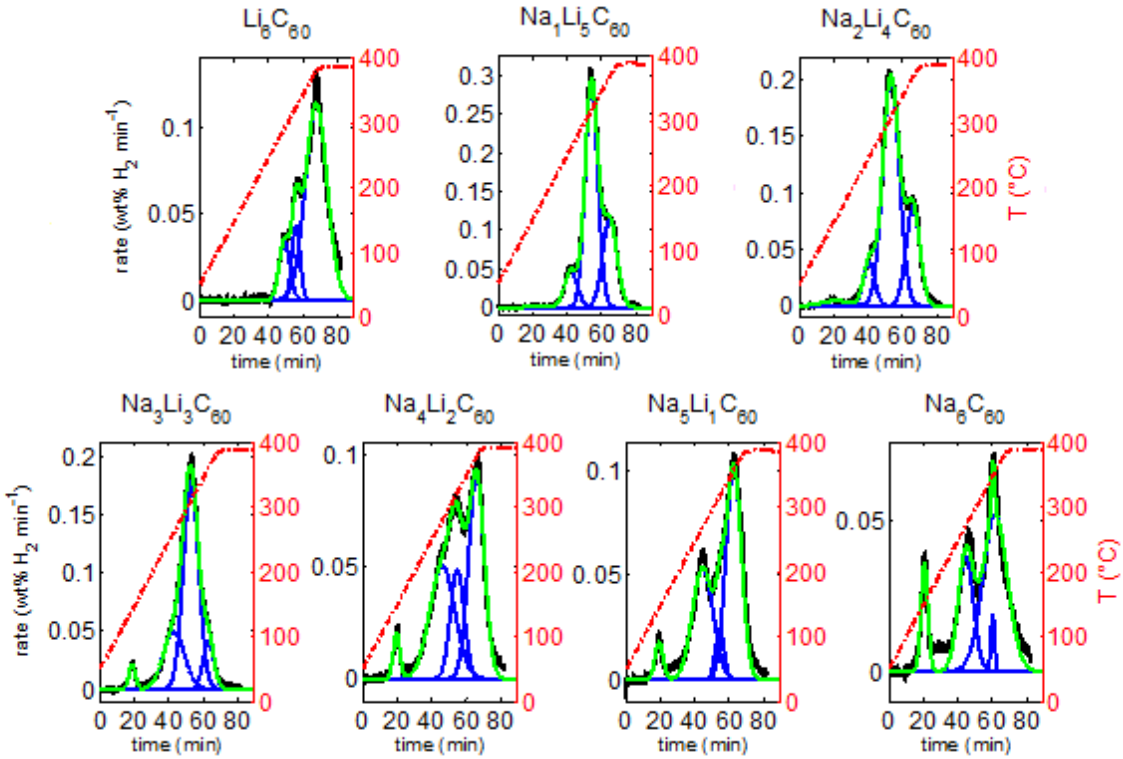


Figure 48. hydrogen desorption rates (black) and fit according to Gaussian functions (blue and green) of $Na_xLi_{6-x}C_{60}$ reported as a function of time (left Y-axis).

We attempted to do the same analysis on the absorption data, anyway, the peaks were not well separated as for desorption and their deconvolutions have been too difficult to study.

Considering the amount of hydrogen desorbed per single step, it is possible to reconstruct the complete dehydrogenation processes of $Na_xLi_{6-x}C_{60}$ compounds.

It has been found that the hydrogenation involves the segregation of part of the metal in form of hydride (NaH and LiH in our case) [8,9]. To better explain this investigation we can use the following general equation:

$$Na_xLi_{6-x}C_{60} + \frac{y}{2}H_2 \overset{(T,p)}{\Longleftrightarrow} Na_{x-\alpha}Li_{6-x-\beta}C_{60}H_{y-\alpha-\beta} + \alpha LiH + \beta NaH \qquad (1)$$

Here $\alpha$ and $\beta$ are the amount of lithium and sodium hydrides respectively.
Unfortunately, is difficult to quantify these values from XRD data, since the structure of hydrofulleride is unknown and a quantitative phase analysis via Rietveld refinement is not possible. In $Na_{10}C_{60}$, $Li_6C_{60}$ and $Li_{12}C_{60}$ part of the alkali metal is de-intercalated in form of hydride during the absorption process [8,10,53]. The measurements on hydrogenated $Na_xLi_{6-x}C_{60}$ highlighted the presence of both LiH and NaH (see Figure 46). It is possible to just estimate a rounded up *y* assuming $\alpha=\beta=0$. Another assumption we have done is that hydrofullerene composition is $C_{60}H_{2n}$, where $n\geq1$, since only an even number of hydrogens is considered stable on $C_{60}H_y$ [46]. Below, for simplicity we will exclude from discussion the first absorption process at 140 °C.
For $Li_6C_{60}$ about 20 hydrogens are chemisorbed on $C_{60}$ at the end of the absorption process.
During the first two dehydrogenation steps at 291 and 324 °C about 0.28 wt% $H_2$ per step are released (2 hydrogens per step: $C_{60}H_{18}$ and $C_{60}H_{16}$ are respectively formed).
The third dehydrogenation process allows to desorb 2 wt% $H_2$, corresponding to the remaining hydrogens.
During the following three steps of dehydrogenation at 280, 331 and 350 °C, $C_{60}H_{34}$, $C_{60}H_{24}$ and $C_{60}$ are respectively formed.
When *x*=1, about 36 hydrogens are chemisorbed on fullerene ($C_{60}H_{36}$) at the end of the absorption process. During the second dehydrogenation process (257 °C) $C_{60}H_{36}$ loses about 4 hydrogens per molecule (becoming $C_{60}H_{32}$). The third step at 315 °C brings to $C_{60}H_{22}$ and the complete dehydrogenation is achieved at 370 °C.

The path of dehydrogenation

for *x*=2 is $C_{60}H_{30} \rightarrow C_{60}H_{28}$ (247 °C) $\rightarrow C_{60}H_{20}$ (308 °C) $\rightarrow C_{60}$ (370 °C).

For *x*=3: $C_{60}H_{26} \rightarrow C_{60}H_{20}$ (261 °C) $\rightarrow C_{60}H_2$ (310 °C) $\rightarrow C_{60}$ (360 °C).

For *x*=4: $C_{60}H_{22} \rightarrow C_{60}H_{12}$ (280 °C) $\rightarrow C_{60}H_{10}$ (322 °C) $\rightarrow C_{60}$ (377 °C).

For *x*=5: $C_{60}H_{20} \rightarrow C_{60}H_{12}$ (269 °C) $\rightarrow C_{60}H_{10}$ (317 °C) $\rightarrow C_{60}$ (356 °C).

Finally, for $Na_6C_{60}$: $C_{60}H_{14} \rightarrow C_{60}H_8$ (270 °C) $\rightarrow C_{60}$ (353 °C).

The first stage around 140 °C was considered together with the first of the three high temperature processes in the calculation of the dehydrogenation paths, due to the low value of hydrogen involved (0-2 hydrogens per $C_{60}H_y$, depending on *x*). Since this process is very far in temperature (about 100 °C) from the other three processes, we attribute it to extrinsic hydrogen species (*e.g.*: hydrogen not bound to carbon). Comparing the four stages of desorption, is clear that the first step only occurs when Na is intercalated. A possible explanation is that those hydrogens responsible for

this process are likely to form a chemical bond with sodium, either in form of ion (*e.g.*: NaH) or clustered with intercalated lithium. The second hypothesis is likely to occur when, as previously assumed [14], the mechanism of hydrogenation can be explained through a spillover-like effect.

In fact, the hydrogen molecule is quickly dissociated on the metal cluster during the first stage of absorption, until the cluster become less effective to perform this task.

Then, the hydrogenation of fullerene continues slowing down its rate since alkali cluster has been partly deintercalated in form of hydride. This was already evidenced in Pt-Pd doped $Li_6C_{60}$, where the presence of a catalyser allowed to continue the fast process at the limit, even when the LiH was segregated [34].

Anyway, in that case the presence of the catalyser did not significantly influenced the desorption enthalpy. On the contrary, by substituting part of the Li with Na, the absorption process is faster, not only during the absorption (comparable with the rate measured for Pt-Pd decorated $Li_6C_{60}$) but also for desorption.

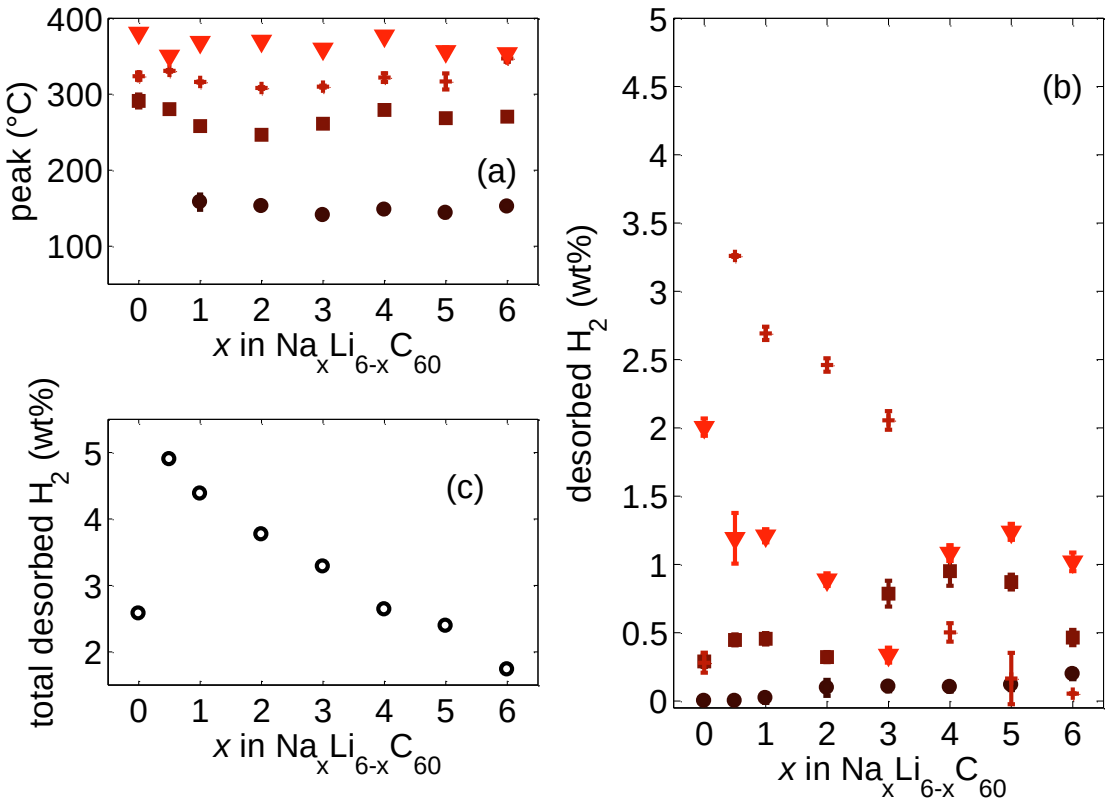


Figure 49. (a) desorption onsets of hydrogenated $Na_xLi_{6-x}C_{60}$ and respective partial desorptions (b) and maximum desorbed content (c), reported as a function of x.

After this gravimetric analysis we have also investigate the thermodynamic properties of the most promising sample $Na_1Li_5C_{60}$, comparing the calculated desorption enthalpies with $Li_6C_{60}$ and $Na_6C_{60}$ take as references.

In the figure we can see the dehydrogenation calorimetric profiles recorded on the sample after the first hydrogenation run.

Coupled calorimetric – manometric measurements were performed by connecting the high-pressure stainless steel cell of the Sensys high pressure DSC by Setaram with the PCTPro-2000.

About 30 mg of the hydrogenated samples (after the first charging run) were discharged by heating from room temperature up to 450 °C at 0.5 bar of hydrogen in dynamic mode (heating rate = 5 °C/min).

For $Na_1Li_5C_{60}$ is present one only and quite sharp endothermic peak centred at about 310 °C, resembling the signal of pure $Li_6C_{60}$. By increasing the Na content, one endothermic shoulder at higher temperature appears, making the peak broader and broader and shifting its maximum temperature up to 370 °C for the $Na_5LiC_{60}$ sample.

This large peak resembles the highest temperature signal of $Na_6C_{60}$. Other two endothermic peaks compare in the calorimetric trace of this compound, one centred at 170 °C and the other at 260 °C. Both these signals are coupled with mass loss, hence they are dehydrogenation steps. The desorption enthalpy under the highest temperature signal decrease, from 66 kJ/mol $H_2$ for pure $Na_6C_{60}$ or 63 kJ/mol for $Li_6C_{60}$, to 47 kJ/mol $H_2$ for $Na_1Li_5C_{60}$, value that falls in the binding energy range for practical applications.

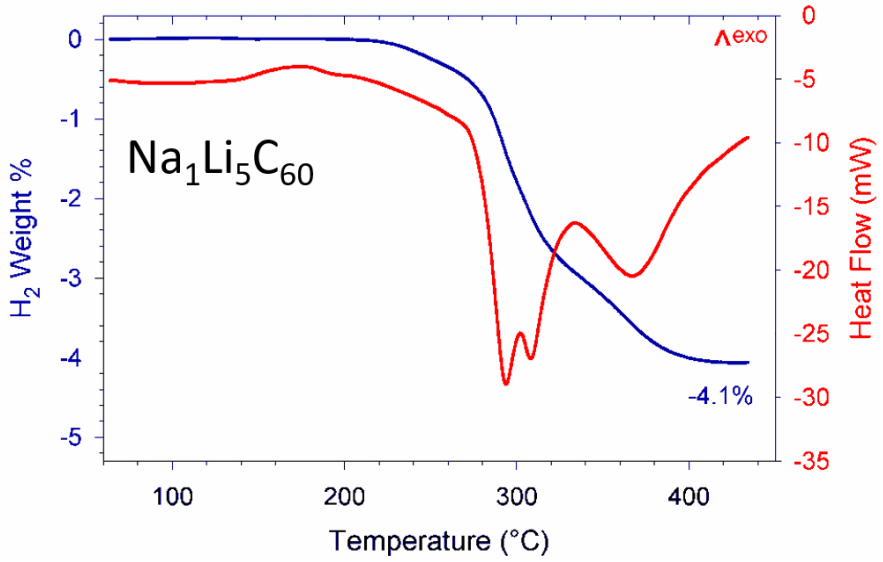


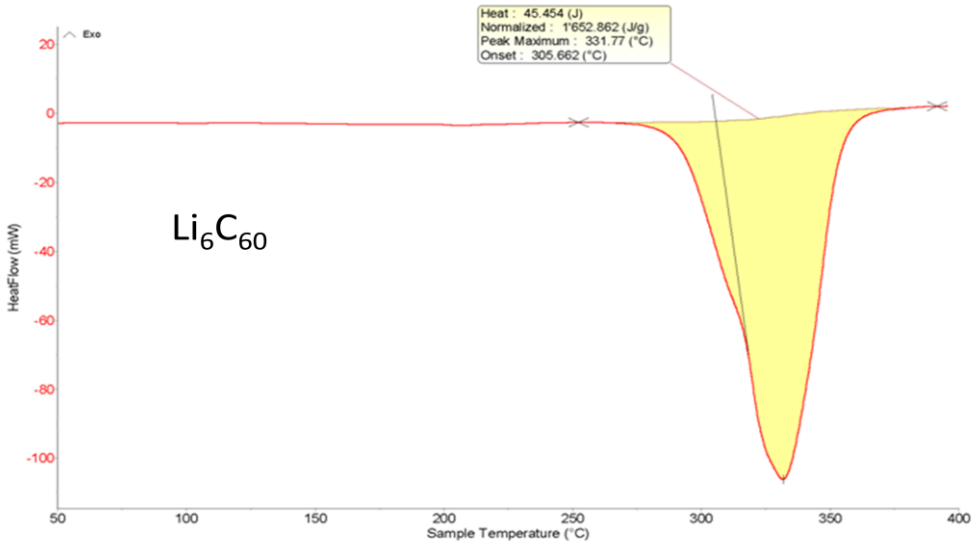


| Sample | $\Delta H_{des}$ (kJ/mol) | $T_{on}$ (°C) |
|---|---|---|
| $Li_6C_{60}$ | 63 | 306 |
| $Li_5NaC_{60}$ | 47 | 279 |

Figure 50. Top: differential scanning calorimetry of $Na_1Li_5C_{60}$ showing three exothermic desorption peaks with a global enthalpy of 47 kJ/mol $H_2$.Bottom: differential scanning calorimetry of $Li_6C_{60}$

So combining the two analysis results is evident that $NaLi_5C_{60}$ is the most promising stoichiometry considering both thermodynamics and gravimetric properties. It's maximum absorption reaches 4.3 wt% $H_2$, when $Li_6C_{60}$ only get 2.7 wt% $H_2$ after a longer isotherm landing at 280 °C.

Finally neutron powder-diffraction measurements on $Na_1Li_5C_{60}$ have been carried out on the high-intensity neutron powder diffractometer WOMBAT at ANSTO (Sydney, Australia), in the same way and conditions of the experiment performed on on $Li_6C_{60}$ and explained in the previous experimental part of this thesis.
We have investigated the structural evolution of the sample during the absorption of 60 bars pressure of deuterium, keeping the sample under pressure and gradually increasing the temperature up to 330°C while measuring the evolution of its diffraction pattern.

Following the $Na_1Li_5C_{60}$ structural patterns evolution is possible to confirm the absence of phase transitions (different results with respect to the $Li_6C_{60}$ system) and notice only an increase in the fcc lattice, involved in the formation and partial segregation of LiH (Figure )

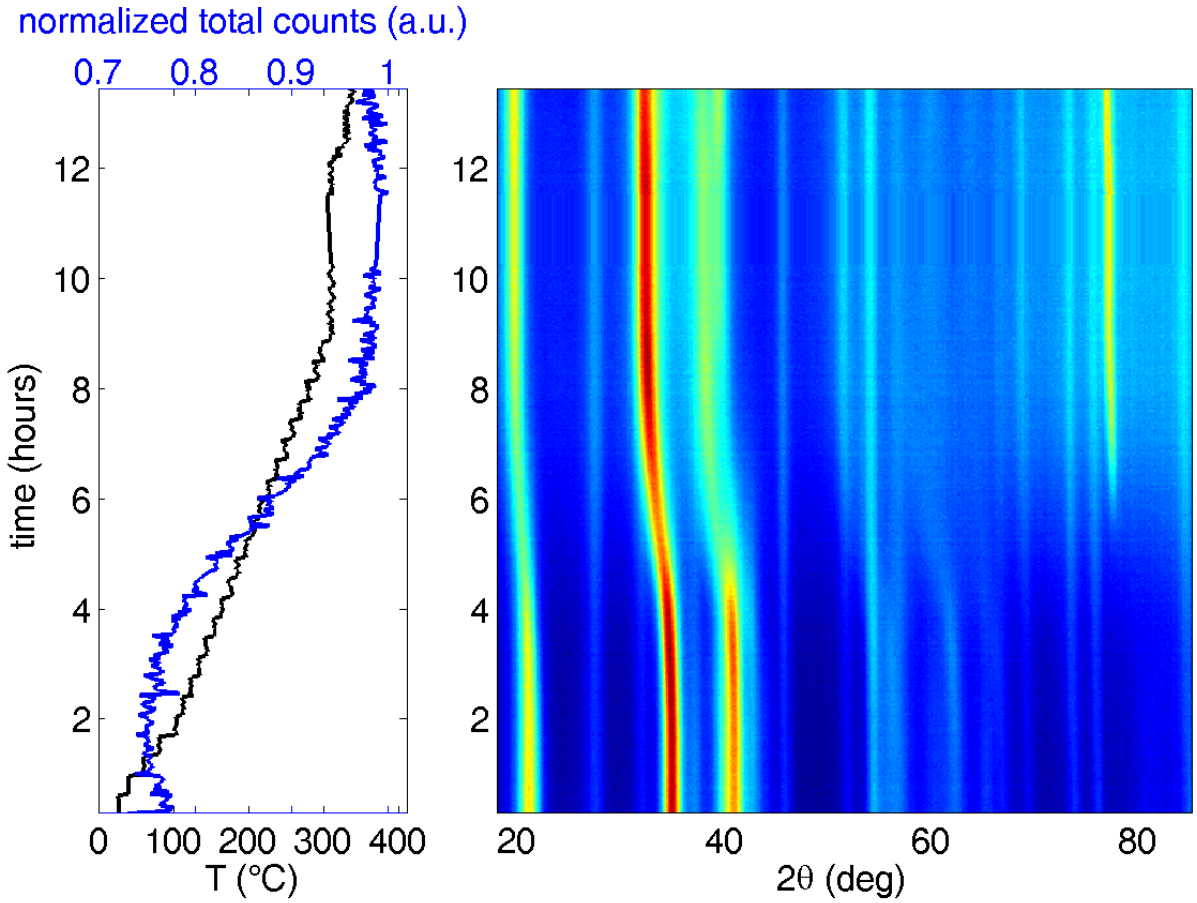


Figure 51: Two-dimensional representation of the time-resolved in situ neutron powder-diffraction patterns of $Na_1Li_5C_{60}$ in the region between 18 and 80° (right) and the corresponding temperature and $D_2$ pressure (left).

We can underline the only presence o f the cubic LiD 111 reflection ( $2\theta = 77.3°$), appearing at 200°C, without any evidence of the NaD formation.
Although there are pressure limits on the experimental setup that avoid the possibility to a complete hydrogenation of the system (only 60 bar of deuterium can be applied), the absence of NaD in the $Na_1Li_5C_{60}$ is probably due to the low amount of sodium in the system.
During the process sodium probably remains always inside the cell making spill-over and improving the kinetics even when lithium segregates as hydride.
When we intercalate more Na, we introduce in the system steric effect problems and we promote the formation of NaH. A further study on the dependence of metal concentration correlated with the formation of metal hydrides can be useful to better understand the mechanisms involved in these materials.

## Conclusions

Mixed alkali-cluster intercalated Na and Li fullerides $Na_xLi_{6-x}C_{60}$ have been synthesized by means of two step procedure consisting in the thermal decomposition of sodium azide in $C_{60}$ and the ball-milling of metallic lithium with $Na_xC_{60}$. The hydrogen storage investigation has proved the catalytic effect of Na in promoting the hydrogenation of $C_{60}$ anion.
The DSC coupled manometric measurements evidenced that also the dehydrogenation enthalpy is affected when $Li_6C_{60}$ is doped with *x* moles of Na. While $\Delta H_{des}$ was 63 kJ/mol $H_2$ for pure $Li_6C_{60}$, it is only 47 kJ/mol $H_2$ when $x$=1. This study allowed us to establish that $Na_1Li_5C_{60}$ is the best compromise between the amount of stored hydrogen and the kinetics of absorption and desorption.
We can finally confirm the substantial interest of these materials in hydrogen storage application in terms of kinetics and thermodynamics properties. The gravimetric density could be further increased and a promising strategy to investigate can be a synthesis, adding transition metals (i.e Pt or Pd), of a cointercalated alkali and transition fulleride system combining the properties of both metal families.

The second part of this chapter is focused on graphene based materials.
We have discussed in the introductive part of this thesis that in the case of graphene for solid state hydrogen storage we need to decorate our system with metal nanoparticles to promote a chemisorption of atomic hydrogen due to the spillover effect [47].
We also know that the process involved in the dissociation of hydrogen molecule requires high temperature because the strength of the molecular bond.
Preliminary results suggested that relatively sharp particle size distribution allow a contemporary improvement of $H_2$ absorption and destabilization during the desorption process.
In fact the reduction of transition metal particle size has been identified as possible improvement because it facilitates this dissociation process and it lowers the de-hydrogenation enthalpy.
We succeeded to prepare a suitable graphene based system thanks to the development of a novel transition metal addition strategy based on the decomposition of metal organic precursors and, in particular using a metal-carbonyl clusters precursor.
We have chosen to start the decoration of our graphene with transition metals instead of using alkali or alkaline earth metals, as we have seen in the previous part of this chapter in the case of metal intercalated fullerides, because transition metals are known from literature to better promote spillover effect [47,49].
In the following part the synthetic strategy to obtain graphene decorated with transition metal nanoparticles (nickel and platinum) will be presented.
After this first work on synthesis and nanoparticles size optimization, it will be presented a study on the use of decorated graphene as a substrate for the in situ (graphene surface) production of nanosized $MgH_2$, with the aim of reduce its high decomposition temperature, investigating the thermodynamic properties of the metal hydride.

### 3.4 Synthesis of metal decorated graphene

Graphene is a perfect substrate material; bulk synthesis of graphene and its decorations with metals can open to interesting opportunities in the field of energy storage or heterogeneous catalysis.
We are able to obtain gram amount of thermally exfoliated graphene (TEGO) and we have tuned different synthetic approaches for the decoration and functionalization of TEGO with metal nanoparticles of Ni [39] and Pt.
In particular we have developed a novel 2-steps method for the bulk synthesis of nanoparticles decorated graphene (avoiding its exposure to air). The size and the distribution of nanoparticles can be controlled and optimized varying the thermal decomposition rate, the nature and concentration of metal precursor.
We have investigated different organic precursors and metal clusters like $Ni(acac)_2$ and $Pt_{19}(CO)_{22}$, we have observed the formation of nanoparticles with a diameter less than 20 nm and the formation of single metal atoms (depending on the synthesis) on the graphene's layers.

The morphological and topological properties of the samples have been investigated by means of high resolution transmission electron microscopy (HRTEM, HAADF-STEM).
The main result showed by this work is how single metal atoms can be generated on graphene, providing the opportunity to explore the properties of individual metal atoms.

### 3.4.1 Ni-Graphene

We have followed two different synthetic approaches for the decoration of graphene with Ni nanoparticles starting from two different precursors:
$Ni(acac)_2$ and $[NBu_4]_2[Ni_6(CO)_{12}]^{2-}$

The synthetic approach to obtain a Ni-decorated graphene consists in a two-steps process:

1) Synthesis of graphene from the termal exfoliation of graphite oxide (GO):

- Oxidation of graphite with Brodie method[62] (oxidazing reagents $NaClO_3$ and $HNO_3$)

- Production of TEGO (Thermally Expanded Graphite Oxide)
  Termical exfoliation of GO at 1150°C for 30 min under dynamic vacuum

2) Decoration with metal nanoparticles:
decoration of TEGO via chemical impregnation and decomposition of metal organometallic precursors.

Using this synthetic way, we are able to decorate graphene with a wide variety of transition metals and we can also control the dimension of nanoparticles.

1) The first step consists in the production of TEGO starting from graphite (RW-A grade).
We perform an oxidation of the graphite mixing it in a 3 necks round-bottom flasks with $NaClO_3$ in a weight ratio 1:8 in favor of the oxidazing agent.
In a lateral neck is introduced a funnel with fuming $HNO_3$ to further oxidize the mixture.
The neck in the opposite side is connected with a tube fluxing nitrogen to remove $ClO_2$ vapors formed during the oxidation reaction. This fluxing step is important because a high concentration of these yellow/green vapors can cause an explosion.
In the central neck it is introduced the agitator to keep the reagents under continuous stirring.
The flask is placed in an ice bath in which it is immersed a heater connected to a laptop.

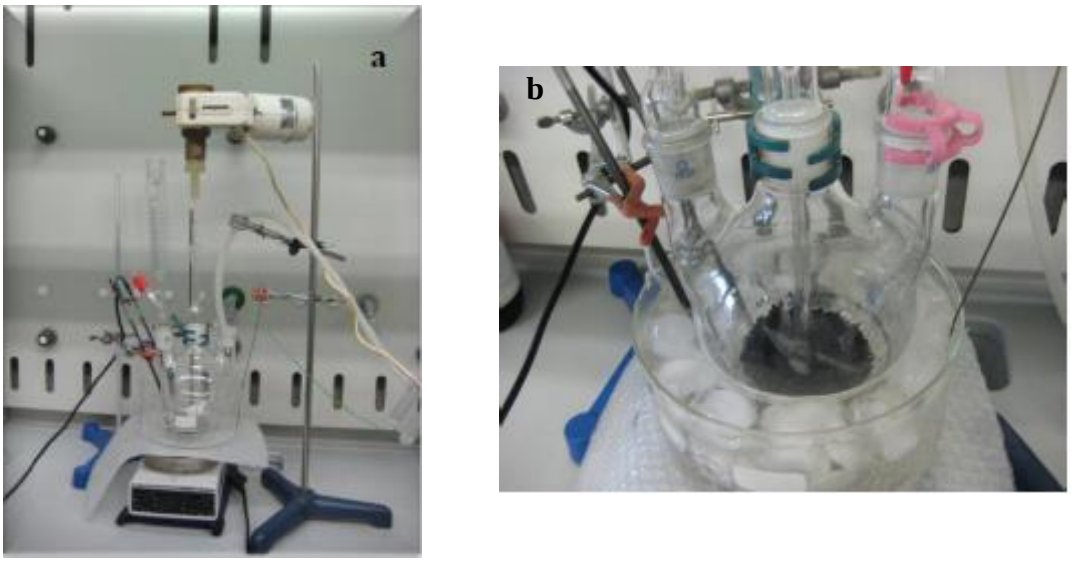


Figure 52: picture of the synthetic apparatus for the oxidation of the graphite (on the left) and focus on the mixed reagents inside the round-bottom flask before the addition of $HNO_3$ (on the right)

When the temperature of the system, controlled with a thermocouple, reaches about 0° C we starts to drop slowly the nitric acid always keeping the temperature close to zero to avoid possible explosions.
After the introduction of all $HNO_3$, we proceed with a thermal treatment descripted in the following steps:

- Up to 60° C with a rate of 20° C/h
- Dwell of 8h at 60° C
- Cooling down at room temperature

The obtained product presents a green coloration.
Then we need to wash the oxidated graphite in a 3M solution of HCl and then wash agin with millipore $H_2O$ until you get a neutral pH of the solution.
Finally the suspension is filtered and the product is dried overnight in an oven at 60°C.

The produced graphite oxide is exfoliated in a oven at 1150°C for 30 min under dynamic vacuum. This process allows to obtain a high amount of termally exfoliated graphene and as we can see in the figure 53 we observe a big increase in the volume of TEGO compared to the graphite oxide precursor.

Figure 53: picture of the thermal exfoliation step.
On the bottom it is possible to compare inside the quarz tube
the volume of the GO precursor and the produced TEGO

2) To perform the decoration with metal nanoparticles, in the case of Ni, we impregnate TEGO and $Ni(acac)_2$ or $[NBu_4]_2[Ni_6(CO)_{12}]^{2-}$ in tetrahydrofuran (THF) according to the schematic procedure shown in figure. A termal treatment at 300°C occurs to decompose the metallic precursors, promoting the formation of metal nanoparticles on the graphene surface.

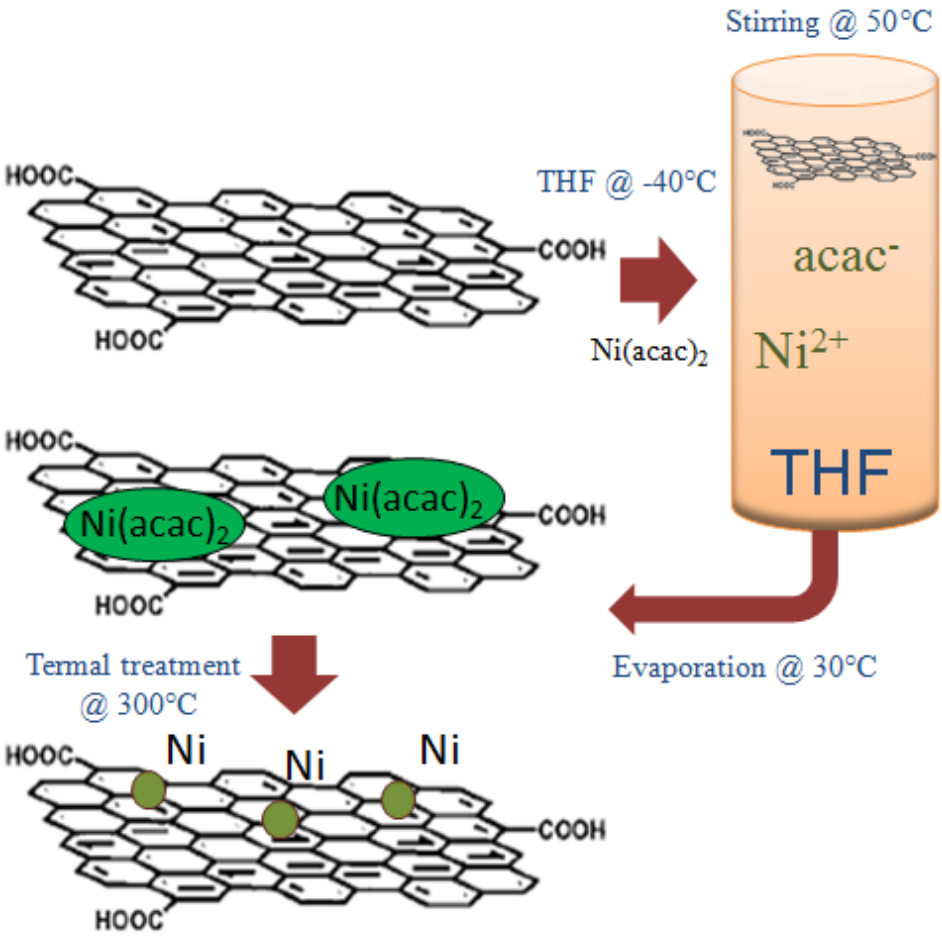


Figure 54: Example of the metal decoration process in the case of Nichel

During all the synthesis we manipulate our samples in a glove-box under Ar atmosphere.

Figure 55: glove box ($O_2$ and $H_2O$ < 0,5ppm).

The TEM analysis of Ni-graphene materials have shown different results in terms of nanoparticles size:

- we have obtained an average diameter of ~20 nm in the case of samples synthesized using $Ni(acac)_2$, confirming the previous analysis of our group [39]

- An average diameter less then 5 nm in the case of the samples obtained from Ni cluster.
  In this sample we have also the formation of atomic size particles with dimensions lower than 1nm

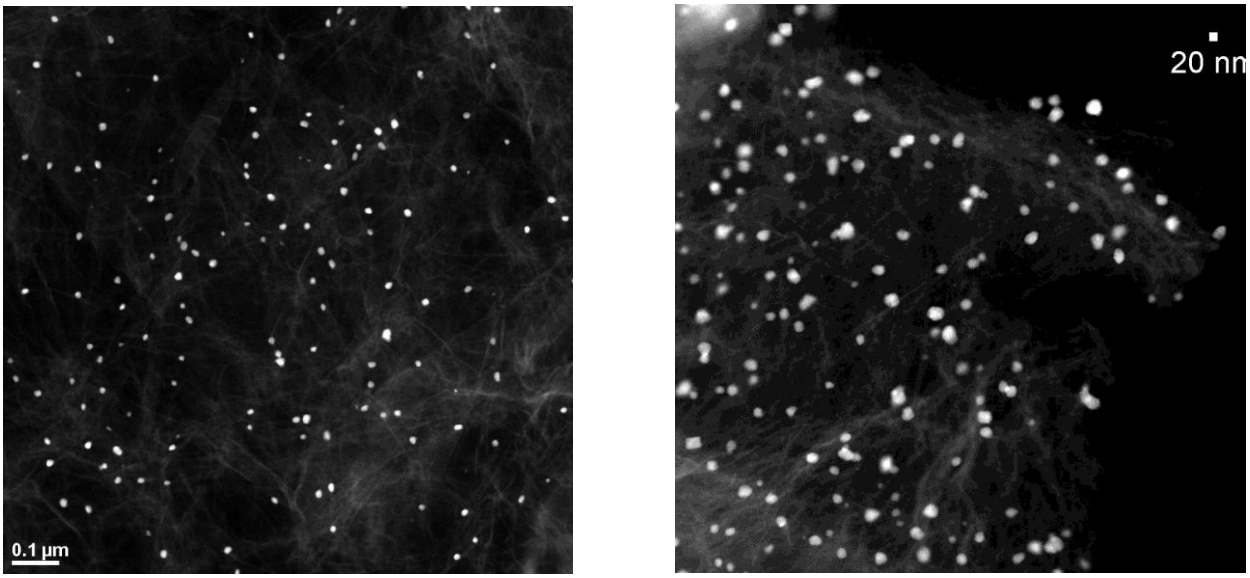


Figure 56: STEM images of Ni-graphene from $Ni(acac)_2$

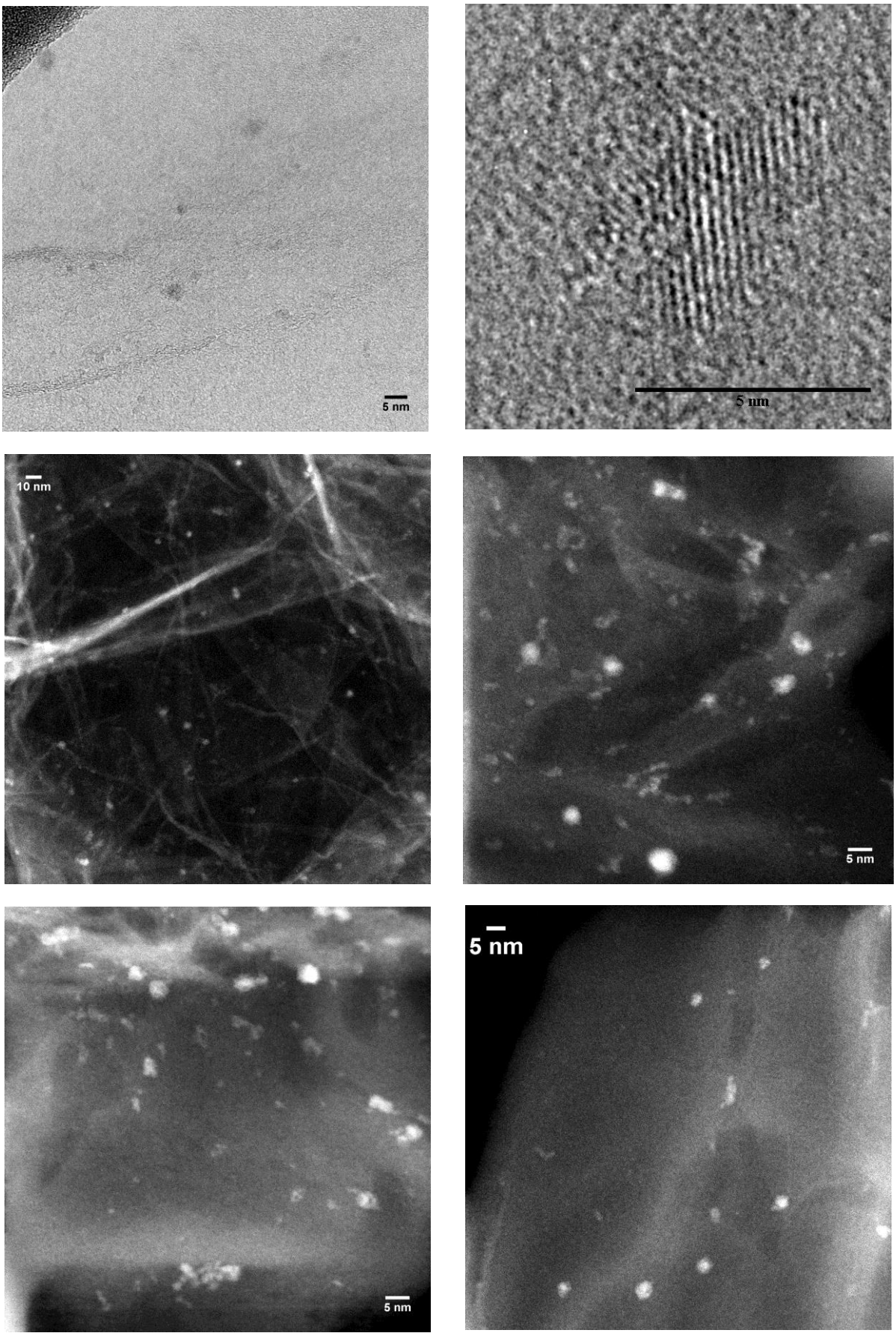


Figure 57: STEM images of Ni-graphene samples from $[NBu_4]_2[Ni_6(CO)_{12}]^{2-}$

### 3.4.2 Pt-Graphene

Following the promising results obtained with Ni-cluster precursor we have synthesized also platinum decorated graphene using the same synthetic way, described in details in the following part.

RW-a grade graphite has been oxidized following the Brodie method.[62]
The graphite (5 g) was mixed with sodium chlorate powder (40 g) in a weight ratio 1:8 and cooled with an ice bath in a fume-hood. By keeping the mixture under continuous stirring, 50 ml of concentrated $HNO_3$ was slowly added, with minimal change in temperature.
The suspension was heated at 60 °C for 8 h with a slow thermal ramp (20 °C/h) and then cooled to RT (30°C/h). After continuous stirring for 1 day, the suspension appeared dark green.
The product has been then diluted in type-1 purified water and filtered through a coarse filter paper.
The product was then suspended in a 3M solution of HCl 37%, filtered, and carefully washed on the filter until the pH of the liquid phase increased to 7. Finally, the product was dried in an oven at 60 °C overnight. The as obtained graphite oxide (GO) was washed and dried in air at 60 °C for one day. Batches of about 600 mg of GO were then placed on the tip of a quartz 0.2 $m^3$ volume vial, connected to a vacuum pump. The thermally exfoliated graphite oxide (TEGO) was obtained as described in the previous part (pag.74) by suddenly exposing the GO to 1423 K in dynamic high vacuum (< 10-5 mbar), in order to exfoliate graphitic planes, and holding at this temperature for 30 minutes before fast cooling in air at room temperature. The vial was then disconnected and opened in Ar atmosphere (< 1 ppm of $O_2$ and $H_2O$) in order to prevent the oxidation of dangling bonds formed by the detachment of oxygen-containing groups during the exfoliation.

In this case of platinum decoration we have studied two different reagents [64,65]:

- $(TBA^+)_4[Pt_{19}(CO)_{22}]^{4-}$ (TBA = tetra-n-butylammonium)
- $(PPh_4)^{2+}$ $[Pt_{15}(CO)_{30}]^{2-}$ ($PPh_4$ = tetraphenylphosphonium)

The impregnation step in this case has been performed in acetonitrile ($CH_3CN$, 99.8 %, Sigma-Aldrich) for $Pt_{19}$-cluster and THF for $Pt_{15}$-cluster. Both the solvents have been anhydrified and degassed before use. These particular solvents have been preferred, with respect to the commonly-used dimethylformamide (DMF) or n-methyl-2-pyrrolidone (NMP), because of their lower boiling point and modest effectiveness in suspending TEGO. This facilitates the evaporation at room temperature, avoiding the thermal-induced decomposition of Pt carbonyl clusters.
These particular platinum cluster precursors have been chosen because of their low nuclearity and the high solubility in $CH_3CN$ and THF.

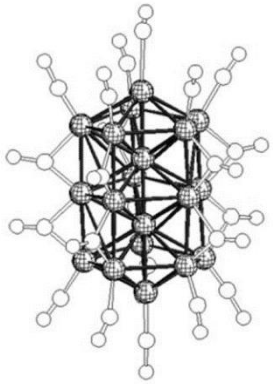

Figure 58: $[Pt_{19}(CO)_{22}]^{4-}$ (ref)

Assuming TEGO as entirely composed of carbon, we synthesized the Pt decorated TEGO according to the atomic ratio (Pt:C) 1:100. This concentration is typical for applications of metal decorated graphene for energy storage and catalysys (see also investigations of Ni-TEGO in ref[63]).

We report only the synthesis method from $Pt_{19}$ valid as a general procedure for both the investigated precursors.

About 200 mg of TEGO and 1 mol% of $(TBA)_4[Pt_{19}(CO)_{22}]$ were suspended/dissolved separately in acetonitrile (10 mL each) by continuous magnetic stirring inside Schlenk glassware, in order to avoid undesired reactions with atmospheric oxidizing agents.
The mixtures were then combined at room temperature and kept under stirring overnight.
The solvent was removed by slow evaporation at room temperature.
In order to remove the carbonylic groups from Pt clusters, Pt-TEGO was heated up to 300 °C in dynamic high vacuum with a fast ramp (20 °C/min) and held at this temperature for 20 minutes before cooling. The rapid heating promotes the molecular decomposition favoring the nucleation process and inhibiting the growth of nuclei.

A summary of the synthesis follows:

$$100 \cdot C_{grafene} + 1/19\ \mathbf{Pt_{19}(CO)_{22}} \rightarrow PtC_{100}\ (\text{in } C_2H_6CN)$$
$$100 \cdot C_{grafene} + 1/15\ \mathbf{Pt_{15}(CO)_{19}} \rightarrow PtC_{100}\ (\text{in THF})$$

Also in this case we have obtain a system which presents both very small aggregates and single atoms as it is clearly show in the figure .

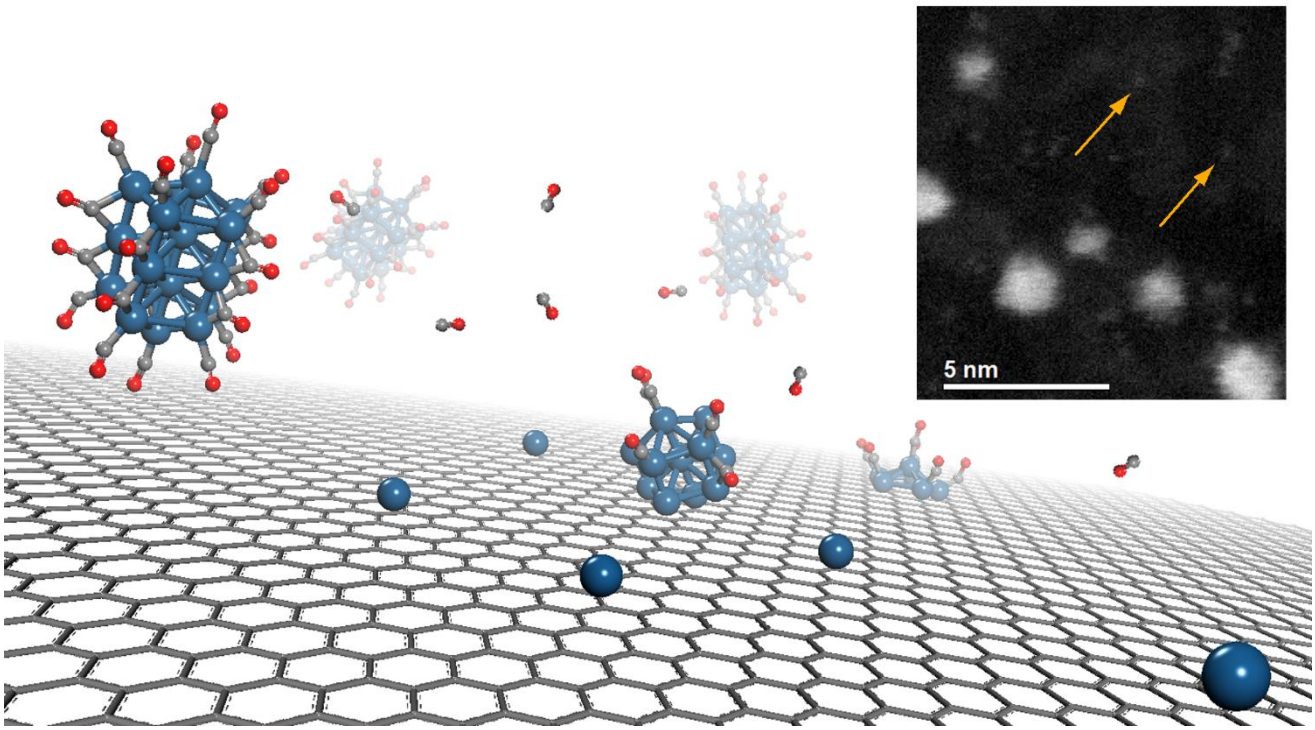


Figure 59: Theorical image of the different Pt nanoparticles and atoms obtained on the graphene layer (background) compared with a STEM images of the sample $PtC_{100}$ from $Pt_{19}$-cluster (on the right).

SEM and HRTEM analysis of both different samples obtained from different Pt-cluster have been reported in the next pages.

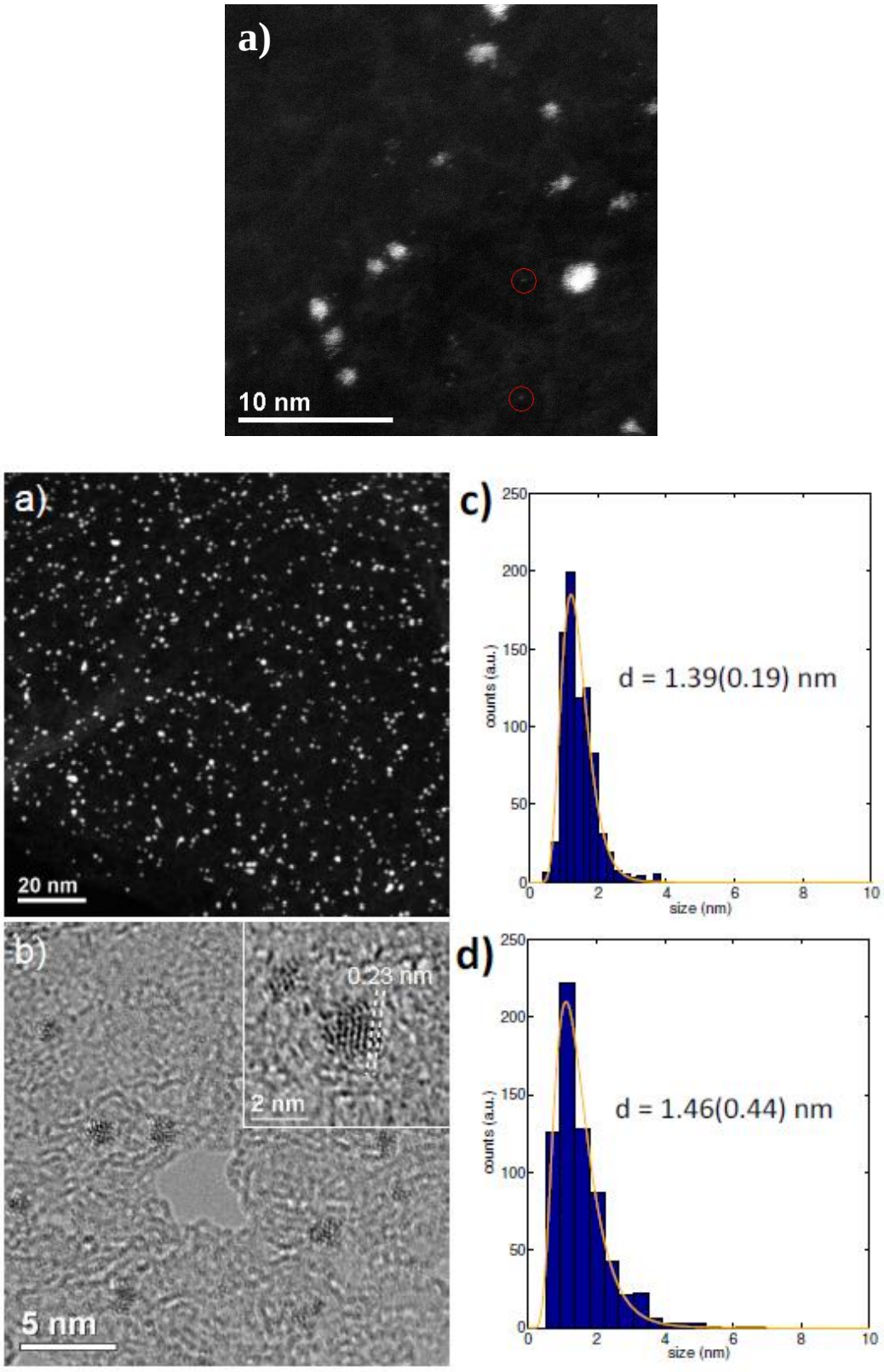


Figure 60: morphology of the Pt-TEGO film.
(a) STEM images, showing the small Pt particlesuniformly dispersed on the graphene substrate; in the images on the top Pt atoms are underlined by red circles.
(b) Corresponding HRTEM image from few Pt nanoparticles.
Some primal atomic planes are formed, with a distance ~0.23 nm, as expected from (111) Pt0 planes (see inset). (c, d) Particles diameter histograms from the as-synthesized (c) and 573 K treated sample (d), respectively (standard deviations in brackets)

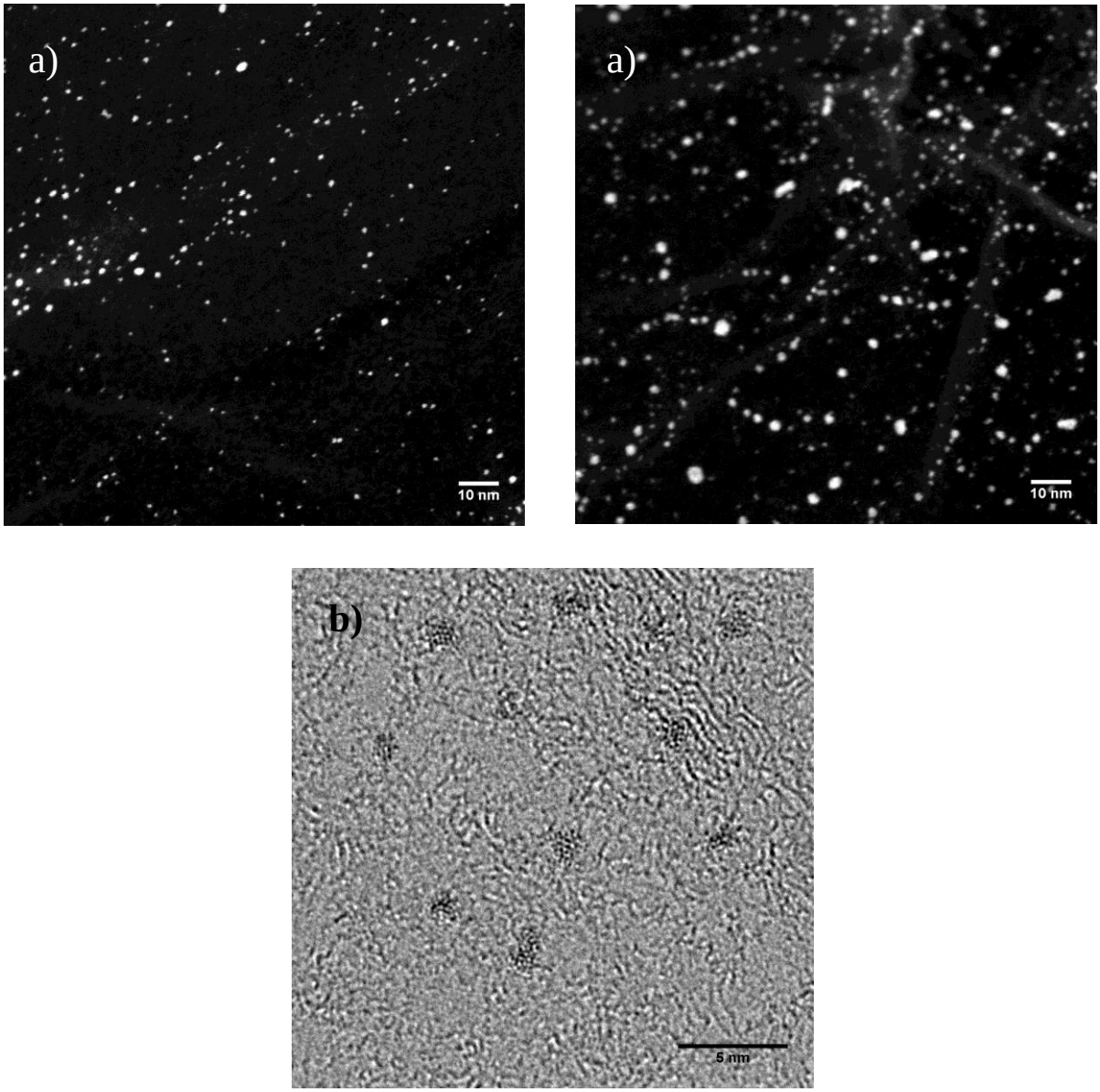


Figure 61: a) STEM images of $PtC_{100}$ from $Pt_{19}$-cluster precursor; b) HRTEM image

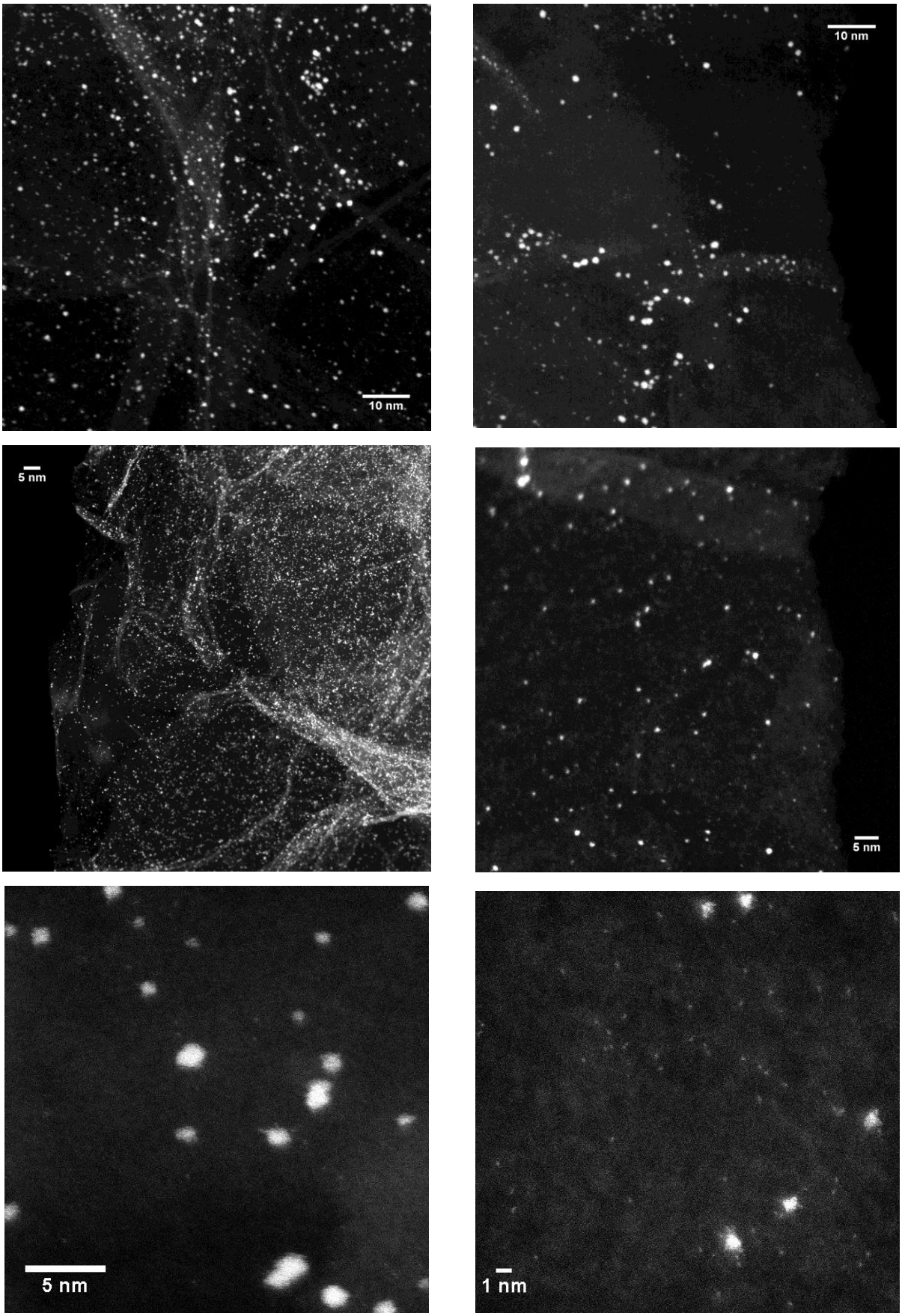


Figure 62: STEM images of $PtC_{100}$ from $Pt_{15}$-cluster precursor

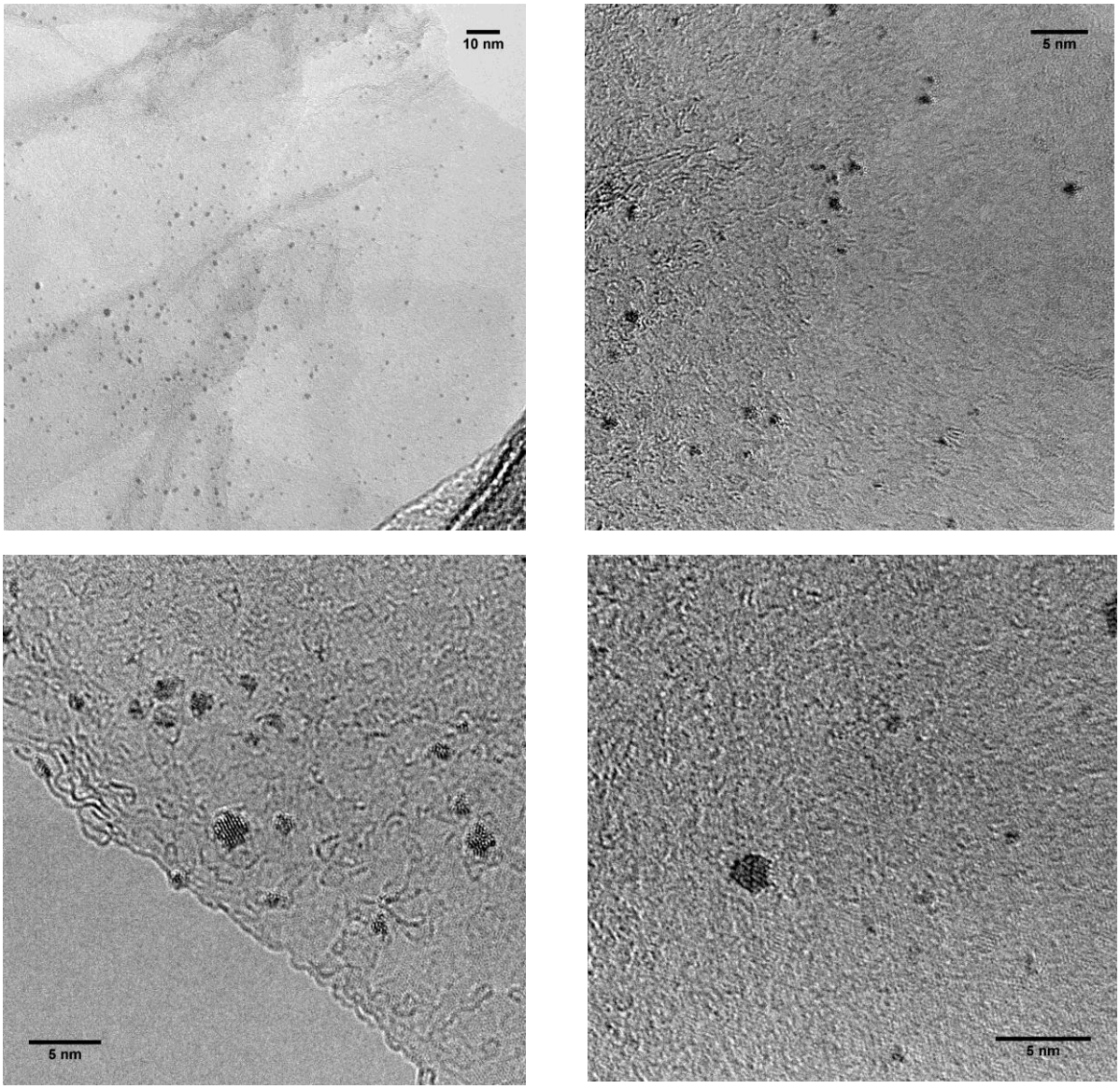


Figure 63: HRTEM images of $PtC_{100}$ from $Pt_{15}$-cluster precursor

In conclusion we have investigated the possibility to synthesize graphene decorated with metal nanoparticles and we have optimized the synthesis to obtain a reduction in the metal aggregate dimension down to atomic scale. To obtained this result we have followed a synthetic strategy using metal carbonyl clusters as metal precursors. The presence of graphene substrate plays a fundamental role in this formation process and further investigation will be useful to understand the cluster decomposition mechanism and the specific interactions between metal cluster and graphene.

### 3.5 Study of nanosized $MgH_2$ produced on a graphene substrate

As we have seen in the introductive part of this thesis, a different promising strategy is the idea of using carbon materials as a substrate to nanosize an hydride [45] to improve its unsuitable thermodynamic and kinetic properties, connected to its high dissociation and desorption temperatures.

This type of investigation has been carried out at the MERlin Group of Prof. Francois Aguey-Zinsou during a collaboration with the University of New South Wales in Sydney and it has been focused on Mg-organic precursors interacting with graphene and metal decorated graphene to produce and nanostructurate $MgH_2$ on the carbon nanostructure surface.

We have followed different synthetic approaches for the decoration and functionalization of graphene with metal nanoparticles and investigated the gravimetric and thermodynamic properties of the hydrogen absorption of these innovative materials.

In particular my first aim was to study the behavior of $Mg/MgH_2$ on the surface of graphene and also to investigate the formation and properties of Ni alloys with Mg [39], starting from a one pot two-metal decoration of substrate adding Ni as catalyzer to further promote the hydrogen storage performances.

The choice of mixing together these two materials (hydride and carbon) to realize a more complex and promising system, taking advantage of their unique properties, is born from experimental and theoretical studies that have recently demonstrated that decreasing the particle size is also capable of a thermodynamically destabilization of Mg-based hydrides, leading to a further enhancement of hydrogen storage performance. To destabilize the strong Mg-H bonds (76 $kJ.mol^{-1}$) is also known in literature the use of Ni, that forms weak Ni-H bonds, in particular in the case of $Mg_2Ni$ alloys forming $Mg_2NiH_2$ (65 kJ.mol-1) after hydrogenation.

In addition to the stability problem, one of the most difficult issue to solve is the high surface energy that allows the growth and aggregation of nanoparticles during the consecutive thermal treatments for $H_2$ charge and discharge, worsening the nanostructured morphology and the storage properties. Therefore to realize a reversible hydrogen storage process in Mg-based hydrides, overcoming the exo-/endothermic reactions involved in hydrogenation/dehydrogenation process, we need to have a rapid heat transfer in the system.

Graphene is a perfect candidate to host nanoparticles because of its light weight, high chemical stability and excellent thermal conductivity, combining the ability to support
well-dispersed nanoparticles and also prevent their riaggregation and growth, promoting the difficult formation of free standing Mg nanoparticles that are highly unstable.

Furthermore our defective TEGO, compared to an ideal graphene, represents an even more interesting and promising system because its higher amount of defects and grain boundary increases the number of dissociation sites and leads more $H_2$ diffusion and the nucleation of the hydride phase.

**Samples preparation**

The first step was to synthesize different samples of Mg-graphene starting from 9,10-Dihydro-9,10-anthracendiyl-tris(THF)magnesium ($MgA.(THF)_3$) and di-n-butylmagnesium with a wet chemistry impregnation of these precursors on bulk graphene with different concentration in weight of Mg using tetrahydrofuran (THF) as solvent for the first precursor and ciclohexane for the second one.
At the same time we have synthesized samples of graphene with $Mg_2Ni$ alloy on the surface.
We have used a wet chemical approach impregnation of the graphene in THF starting from $MgA.(THF)_3$ and Bis(cyclooctadiene)nickel(0) ($Ni(cod)_2$).

We have also followed another synthetic way to form alloy nanoparticles using tetrakis(dimethylamino)ethylene (TDAE) as a reducing agent in the impregnation process of graphene in THF using $MgA.(THF)_3$ and bis(cyclopentadienyl)nickel ($Ni(Cp)_2$) as metals precursors.

The following is the list of the synthesized samples using $MgA.(THF)_3$ as magnesium precursor:

- MgC10
- MgC100
- $Mg_2Ni$-Graphene 20%wt of alloy
- $Mg_2Ni$-Graphene 10%wt of alloy
- $Mg_2Ni$-Graphene 20%wt of alloy from reductive way using TDAE
- $Mg_2Ni$-Graphene 10%wt of alloy from reductive way using TDAE

The reagents have been dissolved in THF and mixed together.
After removing the solvent, all samples have been treated at 400 ° C for 1 hour to promote the formation of nanoparticles and to remove organic precursors.

The following is the list of the synthesized samples using di-n-butylmagnesium as magnesium precursor:

- MgCx 60%wt of Mg
- MgCx 40%wt of Mg
- MgCx 20%wt of Mg

The reagents have been dissolved in cyclohexane and mixed together.
In this case the heat treatment has occurred at 210 ° C.

Then all the samples have been characterized with Transmission Electon Microscopy (TEM) technique to observe the formation and dimension of metal clusters and the hydrogen absorption properties have been investigated using a TGA/DSC instrument loading all the samples with 30 bar of $H_2$ at 100°C.
In the case of Mg-graphene from di-n-butylmagnesium it is known that the thermal decomposition of this precursor lead to the formation of β-$MgH_2$ from a β-elimination process [57,60] and for this reason we have Investigated the hydrogenation behavior of the as-synthesized samples.

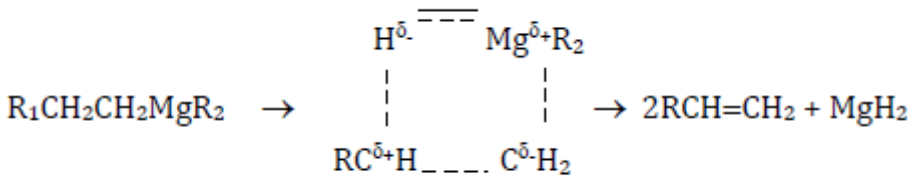


Figure 64: β-elimination process involved in the $MgH_2$ formation

**Description of the results**

The microscopy has shown the presence of nanoparticles in all the samples with diameters less than 10 nm, which is a promising result for hydrogen absorbing materials because nanocrystalline form should gives remarkable improvement of absorption / desorption kinetics.
The TGA/DSC analysis has given us information about the evolution of hydrogen followed by mass spectra (MS) during a thermal decomposition. Measurements were carried out at a heating rate of 10 °C $min^{-1}$. In the images we can see the TGA-DSC analysis (left) and the corresponding MS of $H_2$(right). These results show the decomposition temperatures of $MgH_2$ formed in our materials which are compared whit the decomposition temperatures of the pure $MgH_2$ of 350°C.
The images of the samples analysis are separated for different Mg-precursors used in the synthetic step.

At the beginning we have investigate, by mean of TEM, the formation of the alloy $Mg_2Ni$ on graphene plane. We can observe the presence of both Ni and Mg elements.
Ni nanoparticles are present as free nanoparticles and inside a sort of Mg aggregate in the right concentration 1:2 with respect to Mg as we can see in the figure.

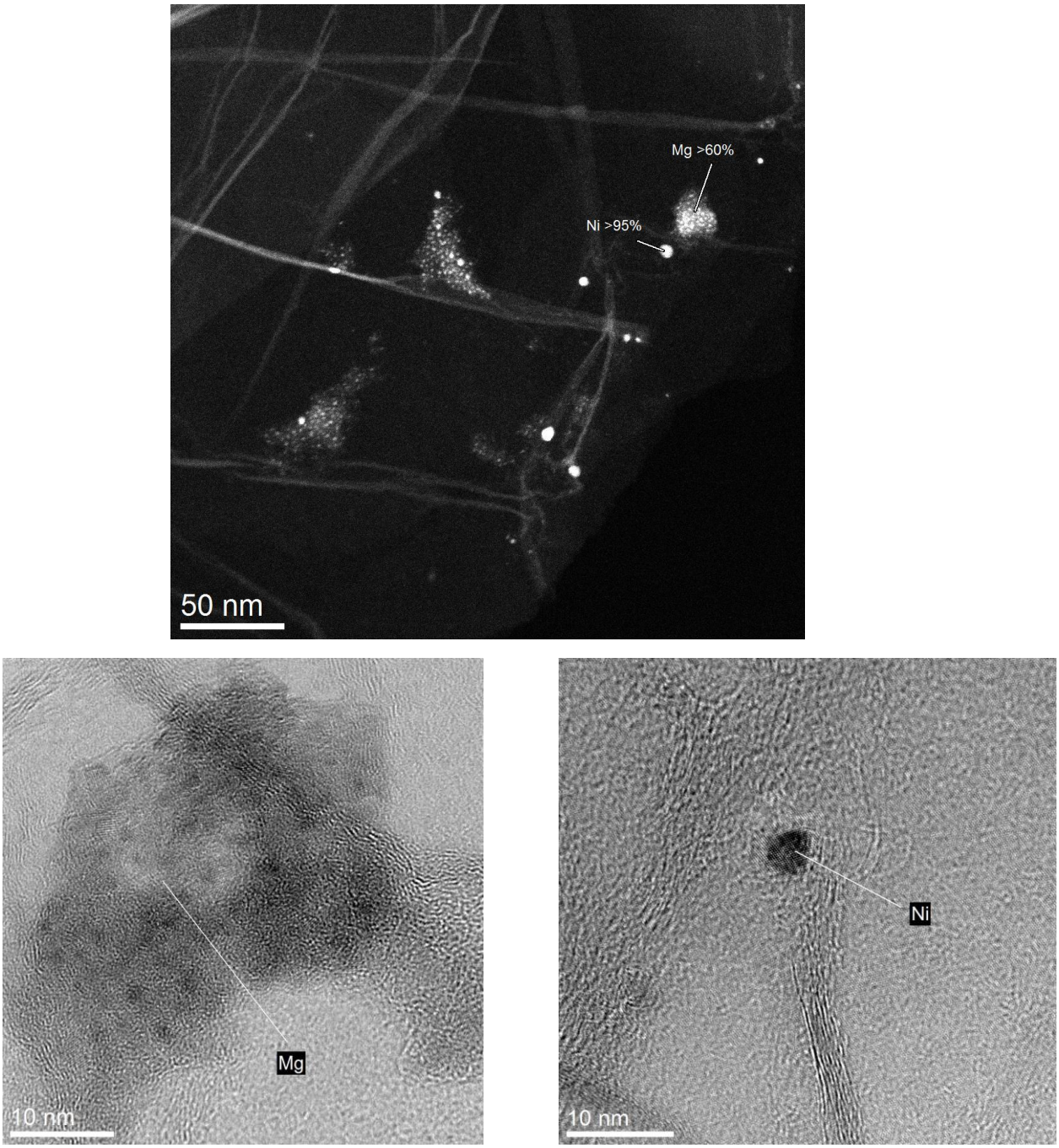


Figure 65: STEM (top) and HRTEM (bottom) images of $Mg_2Ni$-graphene sample

Then we have analyzed all the synthesized samples and in the following figures it is reported both the TEM investigation and the study of combined TGA/DSC analysis.

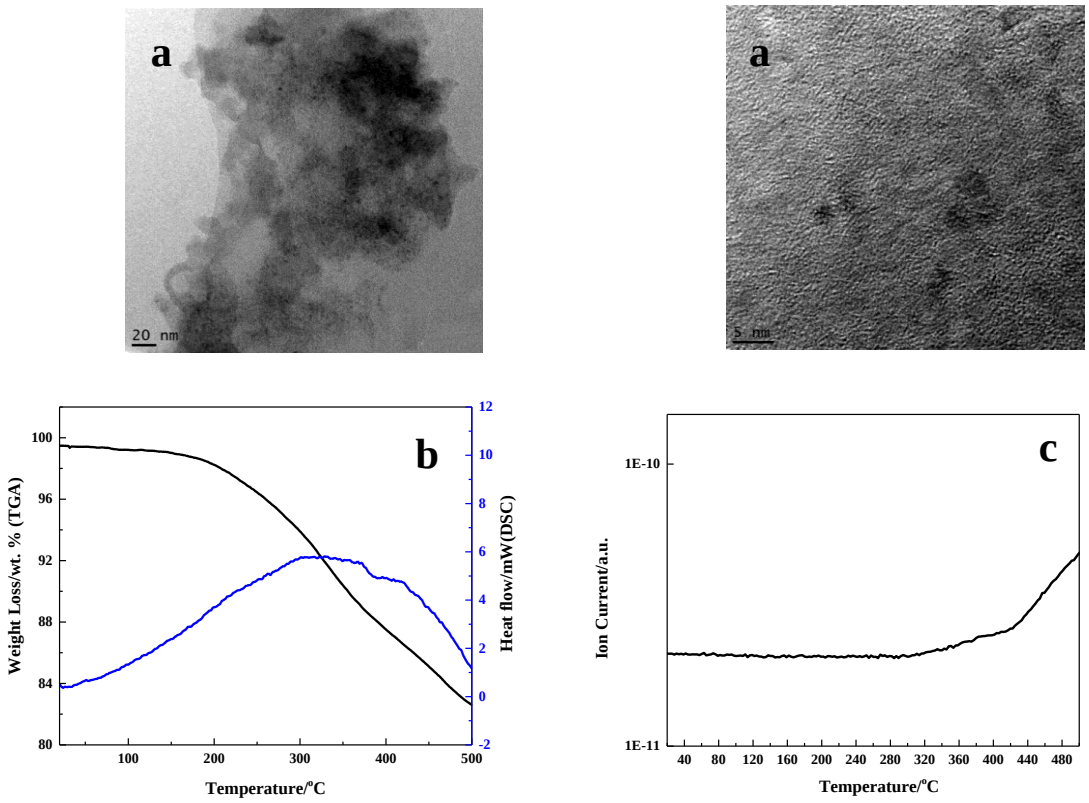


Figure 66: a) TEM images of $MgC_{10}$ (18% of Mg) from $MgA(THF)_3$
**b)** TGA/DSC of $MgC_{10}$ hydrogenated with 30 bar $H_2$ at100°C and c) Mass spectrum of $H_2$

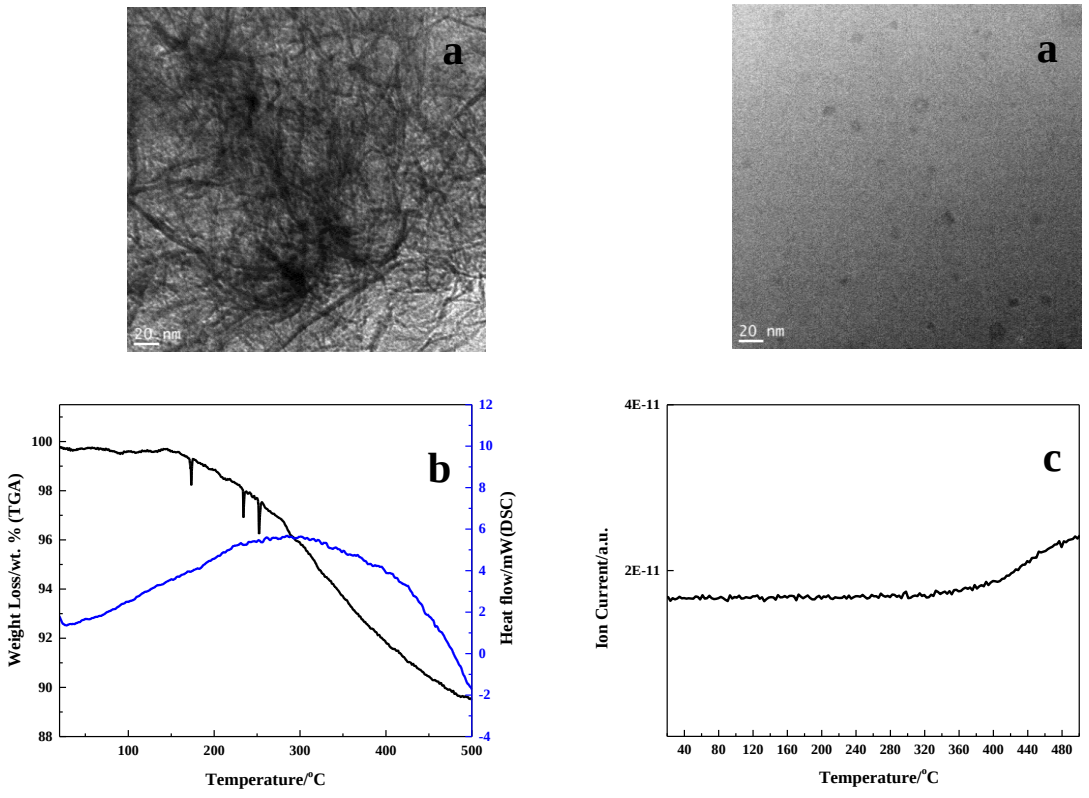


Figure 67: a) TEM images of $MgC_{100}$ (1.8% of Mg) from $MgA(THF)_3$
b) TGA/DSC of $MgC_{100}$ hydrogenated with 30 bar $H_2$ at100°C and c) Mass spectrum of $H_2$

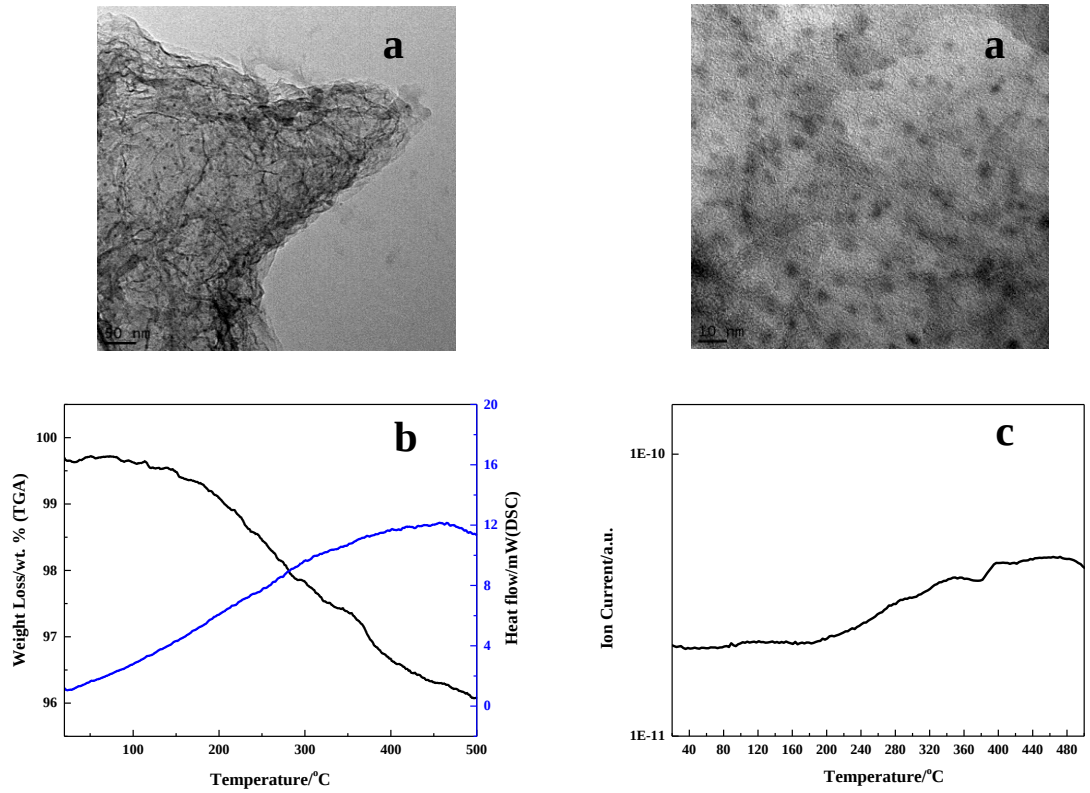


Figure 68: a) TEM images of Mg2Ni-Graph 20%wt (9%wt of Mg)
b) TGA/DSC of Mg2Ni-Graph 20%wt hydrogenated with 30 bar $H_2$ at100°C and c) Mass spectrum of $H_2$

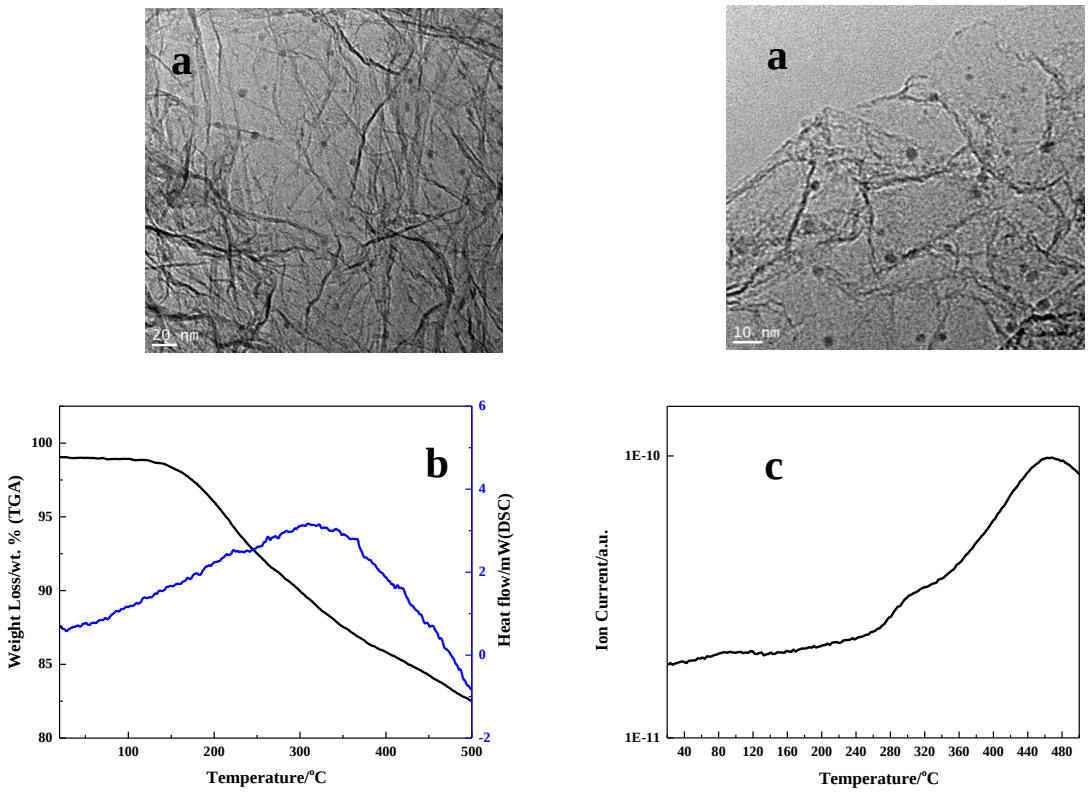


Figure 69: a) TEM images of Mg2Ni-Graph 10%wt (4.5%wt of Mg)
b) TGA/DSC of Mg2Ni-Graph10%wt hydrogenated with 30 bar $H_2$ at100°C and c) Mass spectrum of $H_2$

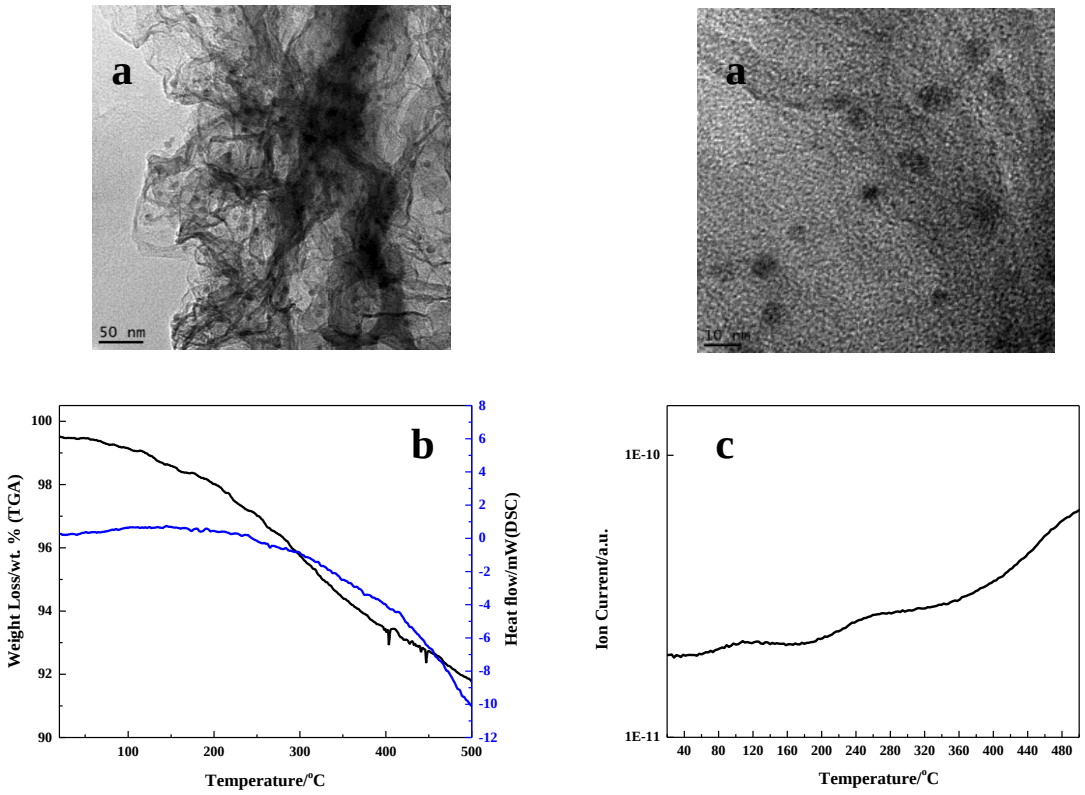


Figure 70: a) TEM images of Mg2Ni-Graph 20%wt from TDAE way (9%wt of Mg)
b) TGA/DSC of the sample hydrogenated with 30 bar $H_2$ at100°C and c) Mass spectrum of $H_2$

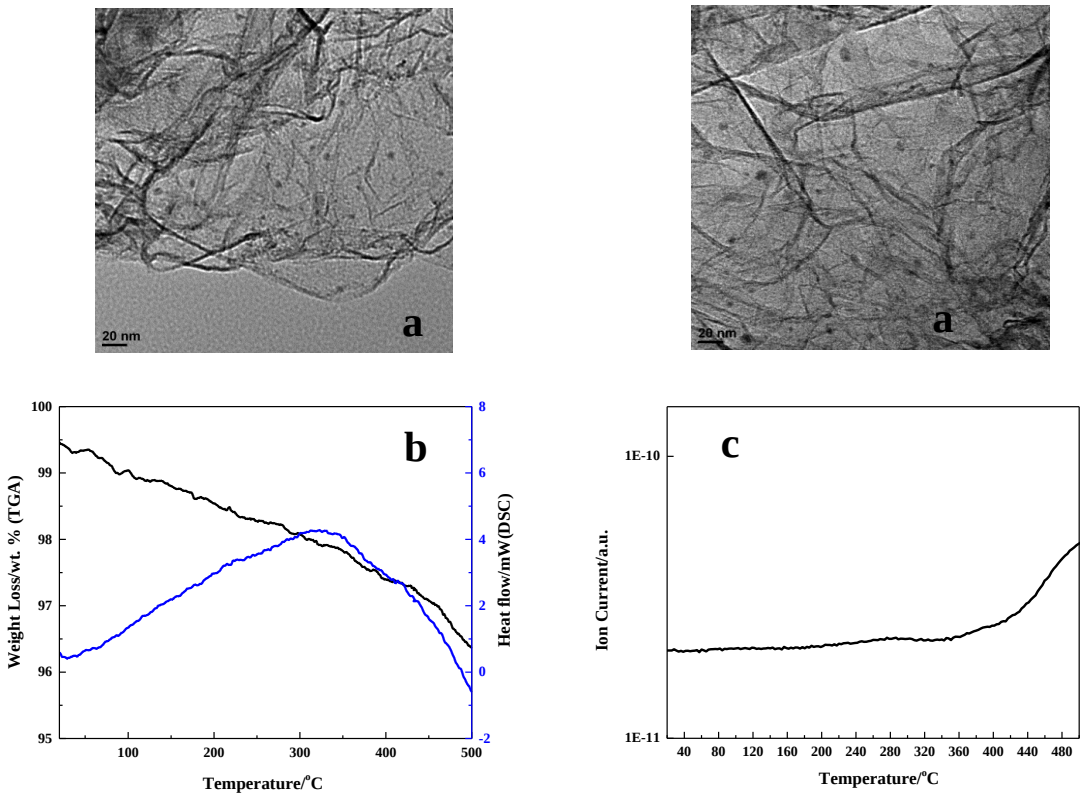


Figure 71: a) TEM images of $Mg_2Ni$-Graph 10%wt+TDAE (4.5%wt of Mg)
b) TGA/DSC of the sample hydrogenated with 30 bar $H_2$ at100°C and c) Mass spectrum of $H_2$

The analysis reported in the previous pages show a first characterization of the materials synthesized started from graphene and $MgA.(THF)_3$.

In all the samples we have observed the formation of Mg nanoparticles on the graphene layer with a diameter size less then 10nm. The best result in terms of reduction in nanoparticles size has been shown by the $MgC_{10}$, where we have less the 5nm diameters, but the nanoparticles are not well dispersed on the surface of the carbon material.

The samples with the alloys have instead a good dispersion of particles on the surface of the material but with these preliminary and quantitative investigations is not so easy to discriminate the Mg from the Ni nanoparticles and to see clearly the alloy $Mg_2Ni$ formation.

$MgH_2$ decomposition under heat treatment is evident from TGA/DSC analysis in terms of weight loss (black line in the figures) and it is also confirmed from the mass spectra in which we can see changes in the evolution of the $H_2$ line at the sample temperatures of the TGA/DSC spectra.

The mass spectra give us also information of the temperature range of the decomposition of $MgH_2$: the figures show the initial hydrogen desorption temperature, corresponding to the first variation of slope from the flat curve, underlining the starting point in which hydrogen is released.

For these materials we found temperatures about 350-400°C for the Mg-graphene samples and lower for the alloys-decorated graphenes. The best result is shown in the table by the $Mg_2Ni$-graphene with 20% wt of alloy which present a decomposition range starting at about 160°C, almost 200°C lower than commercial $MgH_2$ taken as reference.

The following reported samples results are from the Mg-graphene materials synthesized using di-n-butylmagnesium.

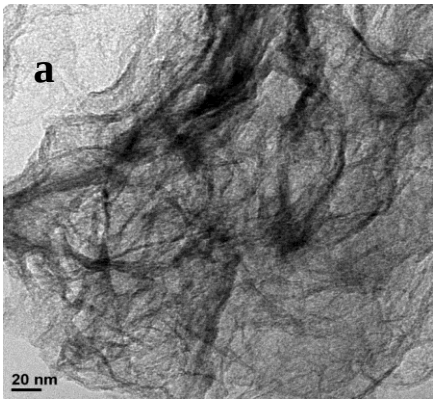


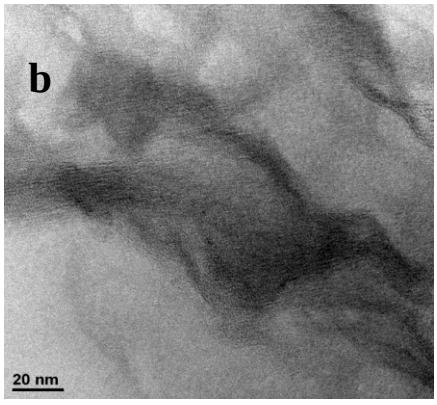


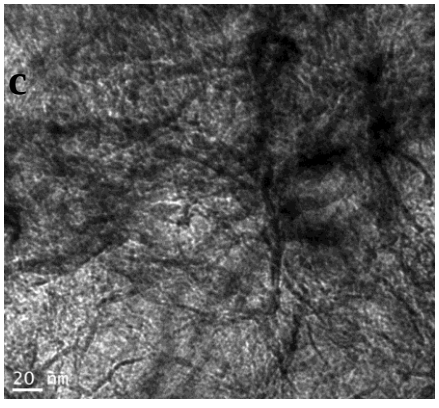

Figure 72: TEM images of **a)**MgCx 60% wt of Mg **b)** MgCx 40% wt of Mg c)MgCx 20% wt of Mg

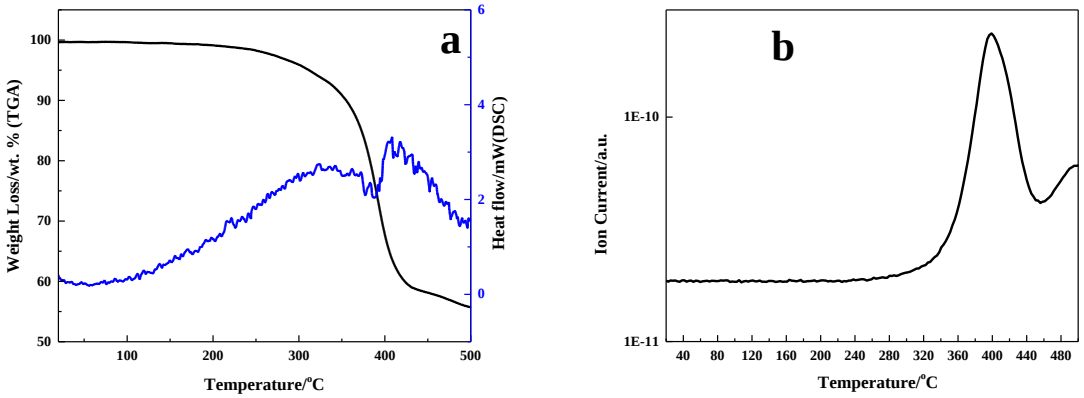


Figure 73: a) TGA/DSC of MgCx 60% wt of Mg and b) Mass spectrum of $H_2$

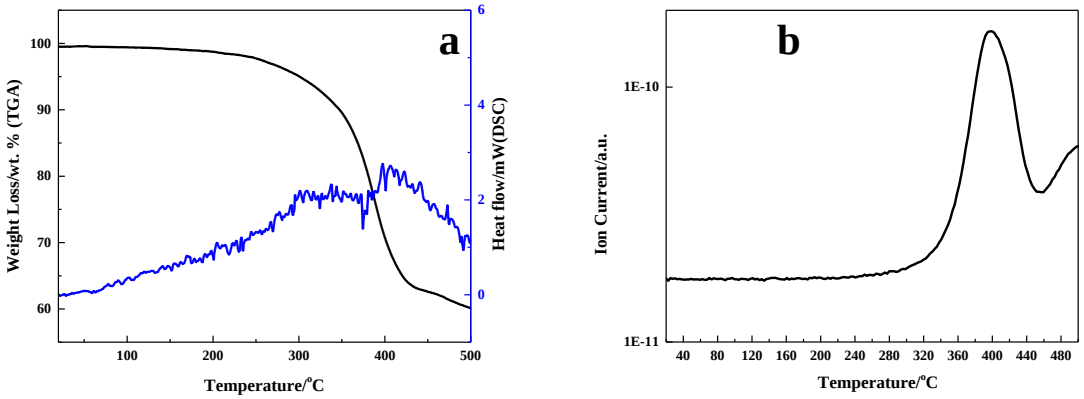


Figure 74: a) TGA/DSC of MgCx 40% wt of Mg and b) Mass spectrum of $H_2$

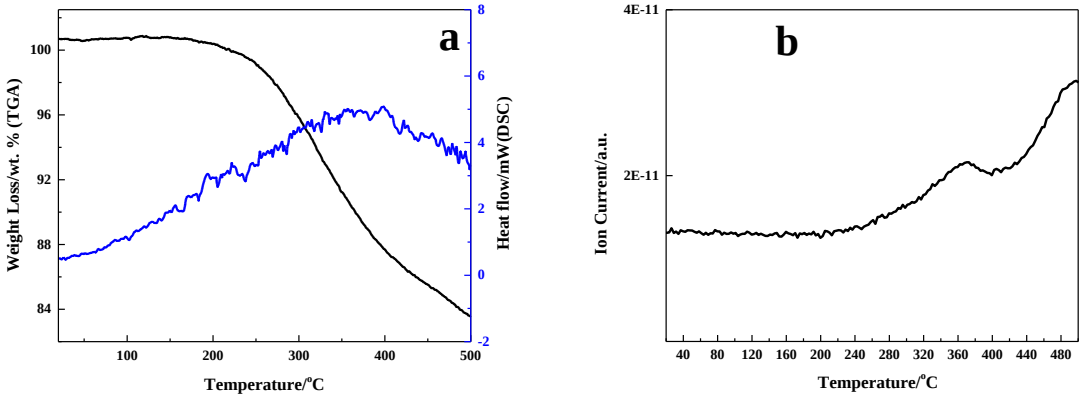


Figure 75: a) TGA/DSC of MgCx 20% wt of Mg and b) Mass spectrum of $H_2$

| ***Samples*** | ***Initial Tdes $H_2$ (°C)*** |
|---|---|
| *$MgC_{10}$ + $H_2$ 30bar 100°C* | *300 °C* |
| *$MgC_{100}$ + $H_2$ 30bar 100°C* | *350 °C* |
| *$Mg_2Ni$-Graphene 20% wt alloy + $H_2$ 30bar 100°C* | *180 °C* |
| *$Mg_2Ni$-Graphene 10% wt alloy + $H_2$ 30bar 100°C* | *160 °C* |
| *$Mg_2Ni$-Graphene 20% wt alloy + TDAE + $H_2$ 30bar 100°C* | *180 °C* |
| *$Mg_2Ni$-Graphene 10% wt alloy + TDAE + $H_2$ 30bar 100°C* | *220 °C* |
| *$MgC_x$ 60% wt Mg* | *300 °C* |
| *$MgC_x$ 40% wt Mg* | *300 °C* |
| *$MgC_x$ 20% wt Mg* | *260 °C* |
| *$MgC_x$ 60% wt Mg + $H_2$ 30bar 100°C* | *300 °C* |
| *$MgC_x$ 40% wt Mg + $H_2$ 30bar 100°C* | *300 °C* |
| *$MgC_x$ 20% wt Mg + $H_2$ 30bar 100°C* | *260 °C* |

Table 6: results

## Conclusions

In this study we have decorated chemically produced graphene (TEGO) with metal nanoparticles starting from Mg precursors and Ni compounds in order to form directly $MgH_2$ on the surface or to study the behavior of $H_2$ with $Mg_2Ni$ alloy on the surface of the material.
The morphological characterization and the study of the $H_2$ evolution have shown very promising results according to the bare $MgH_2$ behaviour takes as reference.
Unfortunately only investigations on magnesium hydride decomposition temperature have been performed. For this reason these preliminary results open the way for a subsequent investigation of the properties and the materials will be subjected to hydrogen absorption/desorption cycles to evaluate their hydrogen storage properties and to test their reversibility.

## References chapter 3


1. Schlapbach L, Züttel A. Hydrogen-storage materials for mobile applications. *Nature* 2001;414:353–8.
2. Züttel A. et al., Hydrogen storage in carbon nanostructures. *Int J Hydrogen Energy* 2002;27:203–12.
3. Yoon M, et al.. Charged fullerenes as high-capacity hydrogen storage media. *Nano Lett* 2007;7:2578–83.
4. Sun Q, et al., First-principles study of hydrogen storage on Li12C60. *J Am Chem Soc* 2006;128:9741–5.
5. Chandrakumar KRS, Ghosh SK. Alkali-metal-induced enhancement of hydrogen adsorption in C60 fullerene: an ab initio study. *Nano Lett* 2008;8:13–9.
6. Sun Q, Wang Q, Jena P, Kawazoe Y. Clustering of Ti on a C60 surface and its effect on hydrogen storage. *J Am Chem Soc* 2005;127:14582–3.
7. Teprovich JA et al., Synthesis and characterization of a lithium-doped fullerane (Li(x)–C60–H(y)) for reversible hydrogen storage. *Nano Lett* 2012;12:582–9.
8. Mauron et al., Reversible hydrogen absorption in sodium intercalated fullerenes. *Int J Hydrogen Energy* 2012;37:14307–14.
9. Knight DA, et al. Synthesis, characterization, and reversible hydrogen sorption study of sodium-doped fullerene. *Nanotechnology* 2013;24:455601.
10. Mauron P et al., Hydrogen sorption in Li12C60. *J Phys Chem C* 2013;117:22598–602.
11. Yildirim et al., Intercalation of sodium heteroclusters into the C60 lattice. *Nature* 1992;360:568–71.
12. Rosseinsky MJ et al., Structural and electronic properties of sodium-intercalated C60. *Nature* 1992;356:416–8.
13. Ricco` M et al., Recovering metallicity in A4C60: The case of monomeric Li4C60. *Phys Rev B* 2007;75:081401.
14. Giglio F. et al., Li12C60: a lithium clusters intercalated fulleride. *Chem Phys Lett* 2014;609:155–60.
15. Aramini M et al., Muon spin relaxation reveals the hydrogen storage mechanism in light alkali metal fullerides. *Carbon NY* 2014;67:92–7.
16. Tomaselli M et al., A multiple-quantum nuclear magnetic resonance study of interstitial Li clusters in LixC60. *J Chem Phys* 2001;115:472.
17. Cristofolini Let al., NMR and high-resolution X-ray diffraction evidence for an alkali-metal fulleride with large interstitial clusters: Li12C60. *Phys Rev B* 1999;59:8343–6.
18. Pratt F. WIMDA: a muon data analysis program for the Windows PC. *Phys B Condens Matter* 2000;289–290:710–4.
19. Delley B. An all-electron numerical method for solving the local density functional for polyatomic molecules. *J Chem Phys* 1990;92:508.
20. Perdew JP et al.,Generalized gradient approximation made simple. *Phys Rev Lett* 1996;77:3865–8.
21. Rols S, Jobic H, Schober H. Monitoring molecular motion in nano-porous solids. *Comptes Rendus Phys* 2007;8:777–88.
22. Blöchl PE. Projector augmented-wave method. *Phys Rev B* 1994;50:17953–79.
23. Kresse G. Efficient iterative schemes for ab initio total-energy calculations using a plane-wave basis set. *Phys Rev* 1996;54:11169–86.

24. K. Parlinski. Software PHONON. <http://wolf.ifj.edu.pl/phonon/>; 2008.
25. Kubo R. A stochastic theory of spin relaxation. *Hyperfine Interact* 1981;8:731–8.
26. Hayano R et al., Zero-and low-field spin relaxation studied by positive muons. *Phys Rev B* 1979;20:850–9.
27. Schenck A. Muon spin rotation spectroscopy: principles andapplications in solid state physics. Adam Hilger Ltd; 1985.
28. Celio M, Meier PF. Exact calculation of the muon polarization function. *Hyperfine Interact* 1984;18:435–40.
29. Meier PF. Spin relaxation of positive muons due to dipolar interactions. *Hyperfine Interact* 1984;18:427–33.
30. Cottrell SP et al., Muon charge state and dynamics in the alkali metal hydrides. *Phys B Condens Matter* 2000;289–290:570–3..
31. Williams WG et al., Muon implantation in alkali metal hydrides. Hyperfine Interact 1997;106:105–10.
32. MacFarlane W, et al., Muon-spin-relaxation studies of the alkalifulleride superconductors. *Phys Rev B* 1998;58:1004–24.
33. Chen Y-L et al., Theoretical study on the small clusters of LiH, NaH, BeH(2), and MgH(2). *J Phys Chem A* 2005;109:9627–36.
34. Aramini, M et al., Addition of Transition Metals to Lithium Intercalated Fullerides Enhances Hydrogen Storage Properties. *Int. J. Hydrogen Energy* 2014, 39, 2124−2131.
35. Yildirim et al., Intercalation of Sodium Heteroclusters into the C60 Lattice. *Nature* 1992, 360, 568−571.
36. Gaboardi et al., Hydrogen Storage Mechanism and Lithium Dynamics in Li12C60 Investigated by μSR. *Carbon* 2015, 90, 130−137.
37. Mauron, P et al., Hydrogen Desorption Kinetics in Metal Intercalated Fullerides. *J. Phys. Chem. C* 2015, 119, 1714−1719.
38. Studer, A. et al., The High- Intensity Powder Diffractometer at the OPAL Reactor. *Phys. B* 2006,385−386, 1013−1015.
39. Maidich, L et al., Investigation of Li and H Dynamics in Li6C60 and Li6C60Hy, 2015. *Carbon* 96, 276-284 (2016)
40. Orimo, S.; Fujii, H., Materials science of Mg-Ni-based new hydrides. *Applied Physics A* 2001, *72* (2), 167-186.
41. Gaboardi, M. et al. Decoration of graphene with nickel nanoparticles: study of the interaction with hydrogen. *J. Mater. Chem. A* **2,** 1039 (2014).
42. Smith, D. K.; Leider, H. R. Low-Temperature Thermal Expansion of LiH, MgO and CaO. *J. Appl. Crystallogr.* 1968, 1,246−249.
43. Molodets et al., Stability of Crystalline Structure and Molecules of Hydrofullerene C60H36 under High Shock Pressures. *Dokl. Phys.* 2008, 53, 562−565.
44. Cataldo, F., Iglesias-Groth, S., Eds. Fulleranes: The Hydrogenated Fullerenes; Springer: Dordrecht, The Netherlands, 2010; Vol. 2.
45. Zaluska A. et al., Nanocristalline magnesium for hydrogen storage, *Journal of Alloys and Compounds* 288 (1999) 217–225
46. Cahill, P. A. in *Chem. Fullerenes* 53–66 (1995).

47. Abhishek K. Singh, Morgana A. Ribas, and Boris I. Yakobson, H-Spillover through the Catalyst Saturation: An Ab InitioThermodynamics Study, *ACSNano* 2009, 3, 1657
48. Montone et al., On the Barriers Limiting the Reaction Kinetics between Catalysed Mg and Hydrogen. *Scr. Mater.* 2010, 63, 456−459.
49. Xiao Ming Liu et al, *Nano Lett*. 2013, 13, 137−141
50. Montone et al., Microstructural and Kinetic Evolution of Fe Doped MgH2 during $H_2$ Cycling. *Catalysts* 2012, 2, 400−411.
51. Kubozono, Y. et al. "Structure and physical properties of $Na_4C_{60}$ under ambient and high Pressures". *Phys. Rev*. B63, 045418 (2001)
52. P. Mauron, M. Gaboardi, D. Pontiroli, A. Remhof, M. Riccò andA. Züttel, *Journal of Physical Chemistry C*, 2015, **119**, 1714–1719.
53. M. Gaboardi et al., *The Journal of Physical Chemistry C*, 2015, **119**, 19705–19721.
54. J. A. Teprovich, et al., *Journal of Alloys and Compounds*, 2013, **580**, S364–S367.
55. M. Aramini, et al., *International Journal of Hydrogen Energy*, 2013, **39**, 2124–2131.
56. R. Röding, et al., *Chemical Physics Letters*, 2005, **413**, 157–161.
57. LefranÇois, M. and Y. Gault, *Décomposition thermique des halogénures d'éthylmagnésium.* Journal of Organometallic Chemistry, 1969. **16**(1): p. 7-19.
58. F. Rachdi et al., *Physical Review B*, 1997, **56**, 7831–7834.
59. S. J. Duclos et al., *Science*, 1991, **254**, 1625–1627.
60. Wiberg, E. and R. Bauer, Der Magnesiumwasserstoff $MgH_2$. *Chemische Berichte*, 1952. 85(6): p. 593-605
61. G. C. Carter, L. H. Bennett and D. J. Kahan, Metallic Shifts in NMR: A Review of the Theory and Comprehensive Critical Data Compilation of Metallic Materials. Part I, *Pergamon Press*, New York, 1977.
62. Brodie, B. C. Sur Le Poids Atomique Du Graphite. *Ann. Chim. Phys*. 1860, 59, 466–472.
63. Gaboardi, M et al., Decoration of Graphene with Nickel Nanoparticles: Study of the Interaction with Hydrogen, *J. Mater. Chem. A* 2014, 2 (4), 1039.
64. Bignami, et al., Comparative Investigations on Platinum Cluster Salts. *Johnson Matthey Technol. Rev.* 2014, 58 (3), 114–123.
65. Washecheck, D. M.et al., *J. Am. Chem. Soc.* 1979, 101 (20), 6110–6112.

**Chapter 4**

# Conclusions

This thesis analyzes several different approaches in the use of carbon nanostructures materials, in particular fullerenes and graphenes, for solid state hydrogen storage applications.
The principal aims of this study have been:

- Synthesis and optimization of alkali and/or alkali earth metal clusters intercalated fullerides and transition metal decorated graphene.

- Study of the hydrogen storage properties of these materials, improving them from the point of view of gravimetric /volumetric density and thermodynamic/kinetic properties.

- Study of the interactions between hydrogen and carbon and mechanisms involved in the hydrogen sorption and desorption process.

- Optimization of nanoparticles dimension and investigation on the role of the size in the hydrogen storage applications.

- Study of the use of metal decorated graphene as a substrate to promote the formation of nanosized $MgH_2$, investigating the thermodynamic properties in the hydrogen storage field of the hydride.

Some major results have been summarized in the following list:

- $Li_{12}C_{60}$ system has been studied by means of muon spin relaxation spectroscopy and Inelastic Neutron Scattering to unveil the behaviour of hydrogen in the first step of the hydrogenation process. The results provides that H (Mu) binds to a lithium forming LiH Only after the amount of free Li in the lattice is suitably decreased, the $C_{60}$ hydrogenation is expected to start.
- $Li_6C_{60}$ system has been studied by means of *in situ* neutron powder-diffraction under deuterium pressure to understand the hydrogen absorption mechanism.
  The sample was kept under 60 bars pressure of deuterium and its temperature was gradually increased up to 330 °C while measuring the evolution of its diffraction pattern.
  The overall absorption process can be described using three different sub-stages of reaction:

  (1) A first deuteration of $Li_6C_{60}$, occurring through an anomalous *fcc* lattice expansion and leading to the formation of $Li_6C_{60}D_8$.

(2) The partial segregation of LiD and the deuteration of fullerene (up to about 2 wt% of equivalent $H_2$ is chemisorbed).

(3) The formation of two line phases and the structural transition to a new *bcc* hydrofulleride structure.

We have also found that the low ionic diffusion of lithium (after its partial decomposition from LiD) into the new *bcc* phase is the rate-limiting stage of the process.

- Mixed alkali-cluster intercalated Na and Li fullerides $Na_xLi_{6-x}C_{60}$ have been synthesized by means of two step procedure consisting in the thermal decomposition of sodium azide in $C_{60}$ and the ball-milling of metallic lithium with $Na_xC_{60}$.

  The hydrogen storage investigation has proved the catalytic effect of Na in promoting the hydrogenation of $C_{60}$ anion.
  The DSC coupled manometric measurements evidenced that also the dehydrogenation enthalpy is affected when $Li_6C_{60}$ is doped with *x* moles of Na, decreasing from
  $\Delta H_{des}$ = 63 kJ/mol $H_2$ in the case of $Li_6C_{60}$, down to only 47 kJ/mol $H_2$ for $Na_1Li_5C_{60}$ system.
  In particular $Na_1Li_5C_{60}$ is the best compromise between the amount of stored hydrogen and the kinetics of absorption and desorption.

- Metal nanoparticles decorated graphenes have been synthesized and we have optimized the systems reducing the metal aggregate dimension down to atomic dispersion.
  To obtain this result we have followed a 2-step synthetic strategy using metal carbonyl clusters as metal precursors.

- Chemically produced graphene (TEGO) have decorated with metal nanoparticles starting from Mg precursors and Ni compounds in order to form directly $MgH_2$ on the surface of the material. The morphological characterization and the study of the decomposition temperature of the as produced magnesium hydride $H_2$ have shown very promising results comparing with the bare $MgH_2$ taken as reference and in particular in the system obtained from $Mg_2Ni$- graphene we low the initial hydrogen desorption temperature from ~350°C (reference) down to 160°C.

Although all these preliminary results are open to additional investigations in order to further improve the storage properties, we can consider all these carbon based materials really promising for energetic or catalytic applications and in the case of intercalated fullerides we have introduced a new class of hydrogen storage materials absolutely comparable with the solid state materials nowadays under investigation.

## Acknowledgements

Siamo arrivati alla fine di questo meraviglioso percorso di tre anni e devo assolutamente ringraziare tantissime persone speciali che mi hanno accompagnato e sostenuto durante il dottorato.
Vorrei ringraziare col tutto il cuore Mauro e tutto il suo/nostro gruppo di ricerca.
La sua presenza costante è stata un punto di riferimento fondamentale per la mia crescita come persona e scienziato. Assieme a Daniele e Mattia mi ha guidato, consigliato, insegnato ed il piacere ed onore che ho provato a lavorare al loro fianco non sono emozioni traducibili in parole. Persone splendide! Auguro a chiunque di avere la fortuna in futuro di poter lavorare nel laboratorio di nano strutture di carbonio della facoltà di Fisica a Parma.
Ringrazio tutti i collaboratori che mi hanno aiutato a realizzare il mio lavoro di tesi e che con la loro competenza e professionalità mi hanno insegnato molto in questi anni.
Tra questi voglio ricordare in particolare Chiara Milanese e Alessandro Girella, Giovanni Bertoni, Francois Zinsou, Stephane Rols, Chiara Cavallari, Neeraj Sharma, James Pramudita, Anton Komlev, Mike e tutto il gruppo dei russi di Novosibirsk, Alessandra Gorreri e Matteo Aramini.
Voglio ringraziare tutti gli amici di Fisica e Chimica che hanno condiviso in questi anni gioie e dolori. Sono davvero tantissimi e avrei bisogno di scrivere una nuova tesi per rendere loro merito. Tra tutti voglio ricordare di fisica: Silvia e Serena, tutti i dottorandi, Alice, Michelangelo, Elena Garlatti, Tiziano, Pietro, Silvio, Nicola, Bruno, Daniela D'Alessio, Fabiana, Marco e Denise, Pietro Trevisan, Michele.
Di chimica come non ringraziare: Silvia e Nico, Andrea Rozzi, Federico Adorni, Vittoria, Emanuele e Claudia, Michele Sidoli, Matteo Dal Checco, Maria Chiara.
Davide Parizzi merita un grazie particolare per essere stato il mio inseparabile compagno di avventure, sempre pronto ad aiutarmi.

Voglio ringraziare separatamente dal gruppo anche Mattia, Sara, Roberta e Daniele Menossi. Mattia lo devo ringraziare due volte, sia come brillante scienziato che si è accollato il peso di dovermi insegnare (soprattutto l'informatica), sia come amico.
A Sara dedico un bellaaaa zia!!! con tutto il cuore e a Roberta, nel ringraziarla, dico di non permettere mai che qualcuno la chiami Jennifer. Per quanto riguarda Daniele Menossi che dire, il bello deve ancora venire…

Allo stesso modo devo ringraziare Daniele Pontiroli e Daniela Ceresini, due amici veri come è difficile trovarne in giro!

Uscendo dall'ambiente universitario ringrazio gli amici del tennis, gli amici del The Space Cinema e Il mio grande amico Giulio Giarratano.

Passando alla famiglia un grazie a tutti.
Devo però in particolare ringraziare di cuore mia mamma per tutto l'aiuto, il sostegno e la pazienza in questi anni, sei stata davvero una presenza fondamentale spronandomi sempre a dare il meglio e ti ringrazio!

Infine ringrazio Giovanna, la persona più importante, che con il suo amore e presenza ha reso possibile tutti i miei sogni, obiettivi e ha saputo sostenermi e incoraggiarmi sempre. Non avrei raggiunto questo traguardo senza di te! Grazie!
Ringrazio anche tutti gli atri amici che sicuramente avrò scordato di citare.

Grazie!!!!